

REACTIVE TRANSPORT MODELING OF HEXAVALENT CHROMIUM  
TREATMENT BY ZERO VALENT IRON

A THESIS SUBMITTED TO  
THE GRADUATE SCHOOL OF NATURAL AND APPLIED SCIENCES  
OF  
MIDDLE EAST TECHNICAL UNIVERSITY

BY

ROZERAN TAŞDELEN

IN PARTIAL FULFILLMENT OF THE REQUIREMENTS  
FOR  
THE DEGREE OF MASTER OF SCIENCE  
IN  
ENVIRONMENTAL ENGINEERING

DECEMBER 2024



Approval of the thesis:

**REACTIVE TRANSPORT MODELING OF HEXAVALENT CHROMIUM  
TREATMENT BY ZERO VALENT IRON**

submitted by **ROZERAN TAŞDELEN** in partial fulfillment of the requirements for  
the degree of **Master of Science in Environmental Engineering, Middle East  
Technical University** by,

Prof. Dr. Naci Emre Altun  
Dean, **Graduate School of Natural and Applied Sciences** \_\_\_\_\_

Prof. Dr. Tuba Hande Ergüder Bayramođlu  
Head of the Department, **Environmental Engineering** \_\_\_\_\_

Assist. Prof. Dr. Sema Sevinç Şengör  
Supervisor, **Environmental Engineering, METU** \_\_\_\_\_

Prof. Dr. Kahraman Ünlü  
Co-Supervisor, **Environmental Engineering, METU** \_\_\_\_\_

**Examining Committee Members:**

Prof. Dr. Filiz Bengü Dilek  
Environmental Engineering, METU \_\_\_\_\_

Assist. Prof. Dr. Sema Sevinç Şengör  
Environmental Engineering, METU \_\_\_\_\_

Prof. Dr. Ülkü Yetiş  
Environmental Engineering, METU \_\_\_\_\_

Assoc. Prof. Dr. Emre Alp  
Environmental Engineering, METU \_\_\_\_\_

Prof. Dr. Merih Aydınalp Köksal  
Environmental Engineering, Hacettepe University \_\_\_\_\_

Date: 06.12.2024

**I hereby declare that all information in this document has been obtained and presented in accordance with academic rules and ethical conduct. I also declare that, as required by these rules and conduct, I have fully cited and referenced all material and results that are not original to this work.**

Name Last name: Rozeran Taşdelen

Signature:

## ABSTRACT

### REACTIVE TRANSPORT MODELING OF HEXAVALENT CHROMIUM TREATMENT BY ZERO VALENT IRON

Taşdelen, Rozeran  
Master of Science, Environmental Engineering  
Supervisor : Assist. Prof. Dr. Sema Sevinç Şengör  
Co-Supervisor: Prof. Dr. Kahraman Ünlü

December 2024, 139 pages

Hexavalent chromium (Cr(VI)) is a toxic heavy metal used in various industries, posing risks to human health and the environment. Its reduction to less toxic trivalent chromium (Cr(III)) can be achieved through Permeable Reactive Barriers (PRBs), which are cost-effective systems for groundwater remediation. The geochemical processes governing Cr(VI) removal and the impact of secondary mineral formations on reactive media are not fully understood, and the modeling of the remediation process is still being developed. This study primarily focuses on modeling Cr(VI) removal process using ZVI with the geochemical modeling tool PHREEQC. The modeling study is based on experimental data previously published in the literature. The main objectives of this study are to: (1) develop a kinetic reaction network that includes passivation by secondary minerals, (2) examine the impact of secondary mineral formation on the reactive capacity of ZVI at different concentrations and flowrates, (3) perform a sensitivity analysis on input parameters, and (4) build prediction models to evaluate the effect of varying inlet Cr(VI) concentrations on removal performance. The results indicate that although ZVI remains in the system at the end of the simulations, its reactive surface area is fully depleted due to surface passivation and the effect of surface passivation diminishes as ZVI concentrations

increase. Furthermore, the model predictions revealed that as the inlet Cr(VI) concentration increases, the remediated Pore Volumes (PVs) decrease exponentially. The results of this modeling study provide insights into the geochemical processes affecting Cr(VI) removal, which can help enhance the design of iron-based PRB applications.

Keywords: Reactive Transport Modeling, Chromium (VI), Zero Valent Iron (ZVI), Permeable Reactive Barriers (PRBs)

## ÖZ

### HEKZVALENT KROM'UN SIFIR DEĞERLİKLİ DEMİR İLE ARITILMASININ REAKTİF TAŞINIM MODELLEMESİ

Taşdelen, Rozeran  
Yüksek Lisans, Çevre Mühendisliği  
Tez Yöneticisi: Dr. Öğr. Üyesi Sema Sevinç Şengör  
Ortak Tez Yöneticisi: Prof. Dr. Kahraman Ünlü

Aralık 2024, 139 sayfa

Hekzavalent krom (Cr(VI)), çeşitli endüstrilerde kullanılan, insan sağlığına ve çevreye risk oluşturan toksik bir ağır metaldir. Daha az toksik olan üç değerlikli kroma (Cr(III)) indirgenmesi, yeraltı suyunun arıtılması için uygun maliyetli sistemler olan Geçirgen Reaktif Bariyerler (GRB'ler) aracılığıyla sağlanabilir. Cr(VI) giderimini yöneten jeokimyasal süreçler ve ikincil mineral oluşumlarının reaktif ortam üzerindeki etkisi tam olarak anlaşılmamıştır ve giderim sürecinin modellenmesi halen geliştirilmektedir. Bu çalışma öncelikle jeokimyasal modelleme aracı PHREEQC ile Sıfır Değerlikli Demir (Fe(0)) kullanılarak Cr(VI) giderme işleminin modellenmesine odaklanmaktadır. Modelleme çalışması daha önce literatürde yayınlanmış deneysel verilere dayanmaktadır. Bu çalışmanın temel amaçları şunlardır: (1) ikincil mineraller tarafından pasifleştirmeyi içeren bir kinetik reaksiyon ağı geliştirmek, (2) ikincil mineral oluşumunun farklı konsantrasyon ve akış hızlarında Fe(0)'ın reaktif kapasitesi üzerindeki etkisini incelemek, (3) girdi parametreleri üzerinde bir duyarlılık analizi ve (4) değişen giriş Cr(VI) konsantrasyonlarının giderme performansı üzerindeki etkisini değerlendirmek için tahmin modelleri oluşturmak. Sonuçlar, simülasyon sonunda Fe(0)'ın sistemde bulunmasına rağmen, yüzey pasivasyonu nedeniyle reaktif yüzey alanının tamamen

tükendiğini ve Fe(0) konsantrasyonları arttıkça yüzey pasivasyonunun etkisinin azaldığını göstermektedir. Ayrıca model tahminleri, girişteki Cr(VI) konsantrasyonu arttıkça arıtılan por hacminin üssel olarak azaldığını ortaya çıkarmaktadır. Bu modelleme çalışmasının sonuçları, Cr(VI) giderimini etkileyen jeokimyasal süreçler hakkında bilgi sağlamaktadır ve bu da demir bazlı PRB uygulamalarının etkinliğinin artırılmasına yardımcı olabilir.

Anahtar Kelimeler: Reaktif Taşınım Modellemesi, Hekzavalent Krom, Sıfır Değerlikli Demir, Geçirgen Reaktif Bariyerler

## ACKNOWLEDGMENTS

First and foremost, I would like to express my sincere gratitude to my supervisor Assist. Prof. Dr. Sema Sevinç Şengör. I am thankful to her for always being there when I needed support, reviewing my progress and guiding me through my studies.

I would like to extend my thanks to Prof. Dr. Kahraman Ünlü and his master student Dr. Burcu Uyuşur, Ph.D. I used the experimental data presented in Dr. Burcu Uyuşur's Master's Thesis on the treatment of chromium contaminated groundwater with Fe(0). Prof. Dr. Kahraman Ünlü, as my co-supervisor, always showed his insight and knowledge into the subject and helped me to complete my master's degree.

I want to give my sincere appreciation to the examining members, Prof. Dr. Filiz Bengü Dilek, Prof. Dr. Ülkü Yetiş, Assoc. Prof. Dr. Emre Alp, and Prof. Dr. Merih Aydınalp Köksal for their contributions and suggestions.

I would not be able to complete this work without the support and patience of my family. I am deeply grateful to my dear mama for all the healthy snack plates she made for my late-night working hours. I want to thank my precious cat, Roka, for her moral and emotional support. Finally, I want to thank my dear boyfriend who listened, supported, and believed in me throughout this academic journey.

## TABLE OF CONTENTS

ABSTRACT .....	v
ÖZ .....	vii
ACKNOWLEDGMENTS .....	ix
TABLE OF CONTENTS .....	x
LIST OF TABLES .....	xii
LIST OF FIGURES .....	xv
LIST OF ABBREVIATIONS .....	xix
1 INTRODUCTION .....	1
1.1 Background.....	1
1.2 Scope and Objective .....	4
2 LITERATURE REVIEW .....	7
2.1 Chromium in the Environment.....	7
2.1.1 Drinking water standards for Cr .....	12
2.2 Cr(VI) Treatment Methods.....	13
2.2.1 Permeable Reactive Barrier (PRBs) Technology .....	16
2.2.1.1 Reduction Mechanism for Cr(VI).....	22
3 MATERIALS AND METHODS .....	31
3.1 Modeling Approach and Description of Experimental Studies.....	31
3.1.1 Interpretation of Column Experiments .....	34
3.2 Numerical Modeling Tool: Phreeq-C .....	35
3.3 Conceptual Model .....	36
3.3.1 Reaction Network Used in the Model .....	39
3.3.1.1 Aqueous Speciation .....	39

3.3.1.2	Mineral Dissolution and Precipitation .....	42
3.3.1.3	Cr(VI) Reduction .....	43
3.3.2	Transport Process .....	45
4	RESULTS AND DISCUSSIONS .....	49
4.1	Non-reactive Transport Simulation.....	49
4.2	Reactive Transport Simulations .....	51
4.2.1	Simulation results of Cr(VI) removal with ZVI for varying Fe(0) concentrations and flowrate conditions.....	55
4.2.2	Impact of Secondary Mineral Formation .....	61
4.2.3	Implications on ZVI Reactive Surface Area .....	69
4.3	Sensitivity Analysis.....	74
4.3.1	Sensitivity Analysis for 10IR Columns .....	75
4.3.2	Sensitivity Analysis for 25IR Columns .....	84
4.3.3	Sensitivity Analysis for 50IR Column.....	100
4.4	Predictions for Removal Performance under Different Inlet Cr(VI) Loadings.....	112
4.4.1	Model Predictions under Different Cr(VI) Loads.....	112
4.4.2	Model Predictions for ZVI Amount and Surface Area under Different Cr(VI) Loads .....	116
4.4.3	Model Predictions for Secondary Mineral Precipitation and Minerals' Effect on Reactivity .....	118
5	CONCLUSION AND FUTURE WORKS .....	127
5.1	Conclusions.....	127
5.2	Future Works.....	130
	REFERENCES.....	133

## LIST OF TABLES

### TABLES

Table 2.1 Chromium Production in World (in thousands of tons) (USGS, 2022) ....	9
Table 2.2 Drinking water standards for total Cr.....	13
Table 2.3 Pros and cons of different reactive materials used in PRBs and related utilization situations (Song et al., 2021) .....	18
Table 2.4 Comparing different uses of ZVI (Song et al., 2021).....	21
Table 3.1 The hydraulic properties of the columns (Uyuşur, 2006) .....	33
Table 3.2 Aqueous speciation reactions used in the model simulation from <i>minteq.v4.dat</i> , (U.S. Environmental Protection Agency, 1998).....	40
Table 3.3 The influent solution composition.....	42
Table 3.4 Secondary mineral reactions taken into account in the model simulation and the rate constants correlating with these reactions from <i>minteq.v4.dat</i> , (U.S. Environmental Protection Agency, 1998) .....	43
Table 3.5 Kinetically controlled Cr(VI) reduction reaction used in the model simulation together with rate expression .....	44
Table 3.6 Transport related input data used in the model simulations.....	47
Table 4.1 The R <sup>2</sup> and MSE values between experimental and model data of control column experiment .....	51
Table 4.2 Calibrated kinetic parameters, R <sup>2</sup> and MSE values for experimental and model data fit considering reaction kinetics with only Fe(0) depletion (Step 1) and also with surface passivation due to secondary mineral precipitation (Step 2).....	53
Table 4.3 Calibrated model parameters for 10IR and 25IR Columns with 0.07 mL/cm <sup>2</sup> .min flux.....	56
Table 4.4 Calibrated model parameters for the 10IR, 25IR and 50IR Columns with flux of 0.127 mL/cm <sup>2</sup> .min .....	57
Table 4.5 R <sup>2</sup> and MSE values along with other model parameters for 10IR, 25IR and 50IR Columns with 0.07 and 127 mL/cm <sup>2</sup> .min fluxes.....	60

Table 4.6 The values of input parameters for each case of sensitivity analysis with 10IR Columns with 0.07 and 0.127 mL/cm <sup>2</sup> .min fluxes .....	75
Table 4.8 Normalized Parameter Sensitivity Index Calculation for 10IR Column - 0.127 ml/cm <sup>2</sup> .min flux –Case 1 and 2.....	81
Table 4.9 Normalized Parameter Sensitivity Index Calculation for 10IR Column - 0.07 ml/cm <sup>2</sup> .min flux –Case 3 and 4.....	82
Table 4.10 Normalized Parameter Sensitivity Index Calculation for 10IR Column - 0.127 ml/cm <sup>2</sup> .min flux –Case3 and 4.....	83
Table 4.11 Absolute S <sub>P</sub> values of the rate constant, k and proprtinality constant, α-CaCO <sub>3</sub> for 10IR Columns with 0.07 and 0.127 mL/cm <sup>2</sup> .min fluxes .....	84
Table 4.12 The values of input parameters for each case of sensitivity analysis with 25IR Columns with 0.07 and 0.127 mL/cm <sup>2</sup> .min fluxes .....	85
Table 4.13 Normalized Parameter Sensitivity Index Calculation for 25IR Column- 0.07 ml/cm <sup>2</sup> .min flux : Case 1 and 2 .....	92
Table 4.14 Normalized Parameter Sensitivity Index Calculation for 25IR Column - 0.127 ml/cm <sup>2</sup> .min flux : Case 1 and 2.....	93
Table 4.15 Normalized Parameter Sensitivity Index Calculation for 25IR Column- 0.07 ml/cm <sup>2</sup> .min flux : Case 3 and 4.....	94
Table 4.16 Normalized Parameter Sensitivity Index Calculation for 25IR Column- 0.127 ml/cm <sup>2</sup> .min flux: Case 3 and 4.....	95
Table 4.17 Normalized Parameter Sensitivity Index Calculation for 25IR Column- 0.07 ml/cm <sup>2</sup> .min flux: Case 5 and 6.....	96
Table 4.18 Normalized Parameter Sensitivity Index Calculation for 25IR Column- 0.127 ml/cm <sup>2</sup> .min flux:Case 5 and 6.....	97
Table 4.19 Normalized Parameter Sensitivity Index Calculation for 25IR Column- 0.07 ml/cm <sup>2</sup> .min flux: Case 7 and 8.....	98
Table 4.20 Normalized Parameter Sensitivity Index Calculation for 25IR Column- 0.07 ml/cm <sup>2</sup> .min flux: Case 7 and 8.....	99

Table 4.21 Absolute $S_P$ values of the rate constant, $k$ and proportionality constant, $\alpha$ - $\text{CaCO}_3$ , $\alpha$ - $\text{Fe}_2\text{O}_3$ , $\alpha$ - $\text{Cr}(\text{OH})_3$ for 25IR Columns with 0.07 and 0.127 $\text{mL}/\text{cm}^2\cdot\text{min}$ fluxes .....	100
Table 4.22 The values of input parameters for each case of sensitivity analysis with 50IR Column 0.127 $\text{mL}/\text{cm}^2\cdot\text{min}$ flux.....	101
Table 4.23 Normalized Parameter Sensitivity Index Calculation for 50IR Column- 0.127 $\text{mL}/\text{cm}^2\cdot\text{min}$ flux: Case 1 and 2 .....	106
Table 4.24 Normalized Parameter Sensitivity Index Calculation for 50IR Column- 0.127 $\text{mL}/\text{cm}^2\cdot\text{min}$ flux: Case 3 and 4 .....	107
Table 4.25 Normalized Parameter Sensitivity Index Calculation for 50IR Column with 0.127 $\text{mL}/\text{cm}^2\cdot\text{min}$ flux:Case 5 and 6 .....	108
Table 4.26 Normalized Parameter Sensitivity Index Calculation for 50IR Column- 0.127 $\text{mL}/\text{cm}^2\cdot\text{min}$ flux: Case 7 and 8 .....	109
Table 4.27 Absolute $S_P$ values of the rate constant, $k$ and proportionality constant, $\alpha$ - $\text{CaCO}_3$ , $\alpha$ - $\text{Fe}_2\text{O}_3$ , $\alpha$ - $\text{Cr}(\text{OH})_3$ for 50IR Column with 0.127 $\text{mL}/\text{cm}^2\cdot\text{min}$ flux .	110
Table 4.28 Absolute $S_P$ values of the rate constant, $k$ and proportionality constant, $\alpha$ - $\text{CaCO}_3$ , $\alpha$ - $\text{Fe}_2\text{O}_3$ , $\alpha$ - $\text{Cr}(\text{OH})_3$ for 10IR, 25IR and 50IR Columns.....	111
Table 4.29 Model Prediction Results for 25IR 0.07 and 0.127 $\text{mL}/\text{cm}^2\cdot\text{min}$ and 50IR 0.127 $\text{mL}/\text{cm}^2\cdot\text{min}$ fluxes .....	116

## LIST OF FIGURES

### FIGURES

Figure 2.1 Various Chromium Deposits in Turkey (MTA, 2022).....	9
Figure 2.2 Eh vs Ph Diagram for Chromium Metal (Palmer and Wittbrodt, 1991)	11
Figure 2.3 Contribution of EU Industries for Chromium Emissions in Water (Tumolo et al., 2020) .....	12
Figure 2.4 Illustration of the process of adsorption-reduction taking place when Cr(VI) is reduced by ZVI (Adapted from Fiuza et al., (2010)) .....	23
Figure 3.1 The illustration for the proposed Cr(VI) removal mechanism inside the column.....	38
Figure 3.2 Grid System of the Simulated Columns .....	46
Figure 4.1 Comparison of model and experimental Cl <sup>-</sup> concentrations for the tracer column test .....	50
Figure 4.2 Comparative simulation results of the kinetic approaches with (blue lines) and without (black lines) the incorporation of secondary mineral formation terms with the experimental results (black symbols) for 10IR column with 0.07 mL/cm <sup>2</sup> .min flux .....	54
Figure 4.3 Experimental and modelling simulation results of the 10IR and 25IR Columns with 0.07 mL/cm <sup>2</sup> .min flux .....	55
Figure 4.4 Experimental and modelling simulation results of the 10IR, 25IR and 50IR Columns with 0.127 mL/cm <sup>2</sup> .min flux .....	56
Figure 4.5 CaCO <sub>3</sub> concentration (mol/kgw) versus time for 10IR, 25IR and 50IR Columns with 0.07 and 0.127 mL/cm <sup>2</sup> .min fluxes .....	62
Figure 4.6 Fe <sub>2</sub> O <sub>3</sub> concentration (mol/kgw) versus time for 25IR Columns with 0.07 and 0.127 mL/cm <sup>2</sup> .min fluxes at the first 2 cm of the column.....	63
Figure 4.7 Cr(OH) <sub>3</sub> concentration (mol/kgw) versus time for 25IR Columns with 0.07 and 0.127 mL/cm <sup>2</sup> .min fluxes at the first 2 cm and 1 cm of the column, respectively .....	63
Figure 4.8 CaCO <sub>3</sub> concentration (mol/kgw) versus distance along the column (m) for 10IR Column with 0.127 mL/cm <sup>2</sup> .min flux for day 1, 5, and 7.....	64

Figure 4.9 CaCO <sub>3</sub> concentration (mol/kgw) versus distance along the column (m) for 25IR Column with 0.127 mL/cm <sup>2</sup> .min flux for day 2, 10 and 14 .....	64
Figure 4.10 Fe <sub>2</sub> O <sub>3</sub> concentration (mol/kgw) versus distance along the column (m) for 25IR Column with 0.127 mL/cm <sup>2</sup> .min flux for day 8, 12 and 17 .....	65
Figure 4.11 Cr(OH) <sub>3</sub> concentration (mol/kgw) versus distance along the column(m) for 25IR Column with 0.127 mL/cm <sup>2</sup> .min flux for day 4, 10 and 17 .....	65
Figure 4.12 CaCO <sub>3</sub> concentration (mol/kgw) versus distance along the column (m) for 50IR Column with 0.127 mL/cm <sup>2</sup> .min flux for day 3, 15 and 24.....	66
Figure 4.13 Fe <sub>2</sub> O <sub>3</sub> concentration (mol/kgw) versus distance along the column (m) for 50IR Column with 0.127 mL/cm <sup>2</sup> .min flux for day 3, 15 and 24.....	66
Figure 4.14 Cr(OH) <sub>3</sub> concentration (mol/kgw) versus distance along the column(m) for for 50IR Column with 0.127 mL/cm <sup>2</sup> .min flux for day 3, 15 and 24 .....	67
Figure 4.15 Changes in the total moles of ZVI with respect to time for 10IR, 25IR and 50IR columns with the 0.07 mL/cm <sup>2</sup> .min and 0.127 mL/cm <sup>2</sup> .min fluxes .....	69
Figure 4.16 Changes in the reactive surface area of ZVI (m <sup>2</sup> ) with respect to time for 10IR, 25IR and 50IR columns with the 0.07 mL/cm <sup>2</sup> .min and 0.127 mL/cm <sup>2</sup> .min fluxes .....	71
Figure 4.17 pH change along the 10IR, 25IR and 50IR Columns with 0.127 mL/cm <sup>2</sup> .min flux at day 5, 10 and 20, respectively .....	73
Figure 4.18 Change in C/C0 vs time graph of 10IR Column 0.07 mL/cm <sup>2</sup> .min flux for Case 1 and Case 2 – 50% increase and decrease in rate constant,k.....	76
Figure 4.19 Change in C/C0 vs time graph of 10IR Column 0.127 mL/cm <sup>2</sup> .min flux for Case 1 and Case 2 - 50% increase and decrease in rate constant, k .....	77
Figure 4.20 Change in C/C0 vs time graph of 10IR Column 0.07 mL/cm <sup>2</sup> .min flux for Case 3 and Case 4 – 50% increase and decrease in $\alpha$ – CaCO <sub>3</sub> .....	77
Figure 4.21 Change in C/C0 vs time graph of 10IR Column 0.127 mL/cm <sup>2</sup> .min flux for Case 3 and Case 4 – 50% increase and decrease in $\alpha$ – CaCO <sub>3</sub> .....	78
Figure 4.22 Change in C/C0 vs time graph of 25IR Column 0.07 mL/cm <sup>2</sup> .min flux for Case 1 and Case 2 – 50% increase and decrease in rate constant,k.....	87

Figure 4.23 Change in $C/C_0$ vs time graph of 25IR Column 0.127 mL/cm <sup>2</sup> .min flux for Case 1 and Case 2 - 50% increase and decrease in rate constant, $k$ .....	87
Figure 4.24 Change in $C/C_0$ vs time graph of 25IR Column 0.07 mL/cm <sup>2</sup> .min flux for Case 3 and Case 4 – 50% increase and decrease in $\alpha$ – CaCO <sub>3</sub> .....	88
Figure 4.25 Change in $C/C_0$ vs time graph of 25IR Column 0.127 mL/cm <sup>2</sup> .min flux for Case 3 and Case 4 – 50% increase and decrease in $\alpha$ – CaCO <sub>3</sub> .....	88
Figure 4.26 Change in $C/C_0$ vs time graph of 25IR Column 0.07 mL/cm <sup>2</sup> .min flux for Case 5 and Case 6 – 50% increase and decrease in $\alpha$ – Fe <sub>2</sub> O <sub>3</sub> .....	89
Figure 4.27 Change in $C/C_0$ vs time graph of 25IR Column 0.127 mL/cm <sup>2</sup> .min flux for Case 5 and Case 6 – 50% increase and decrease in $\alpha$ – Fe <sub>2</sub> O <sub>3</sub> .....	89
Figure 4.28 Change in $C/C_0$ vs time graph of 25IR Column 0.07 mL/cm <sup>2</sup> .min flux for Case 7 and Case 8 – 50% increase and decrease in $\alpha$ – Cr(OH) <sub>3</sub> .....	90
Figure 4.29 Change in $C/C_0$ vs time graph of 25IR Column 0.127 mL/cm <sup>2</sup> .min flux for Case 7 and Case 8 – 50% increase and decrease in $\alpha$ – Cr(OH) <sub>3</sub> .....	90
Figure 4.30 Change in $C/C_0$ vs time graph of 50IR Column 0.127 mL/cm <sup>2</sup> .min flux for Case 1 and Case 2 – 50% increase and decrease in rate constant, $k$ .....	103
Figure 4.31 Change in $C/C_0$ vs time graph of 50IR Column 0.127 mL/cm <sup>2</sup> .min flux for Case 3 and Case 4 – 50% increase and decrease in $\alpha$ – CaCO <sub>3</sub> .....	103
Figure 4.32 Change in $C/C_0$ vs time graph of 50IR Column 0.127 mL/cm <sup>2</sup> .min flux for Case 5 and Case 6 – 50% increase and decrease in $\alpha$ – Fe <sub>2</sub> O <sub>3</sub> .....	104
Figure 4.33 Change in $C/C_0$ vs time graph of 50IR Column 0.127 mL/cm <sup>2</sup> .min flux for Case 7 and Case 8 – 50% increase and decrease in $\alpha$ – Cr(OH) <sub>3</sub> .....	104
Figure 4.34 $C/C_0$ versus time graphs for 25IR Column with 0.07 mL/cm <sup>2</sup> .min fluxes with inlet Cr(VI) Concentrations of 20, 50 and 100 mg/L.....	113
Figure 4.35 $C/C_0$ versus time graphs for 25IR Column with 0.127 mL/cm <sup>2</sup> .min fluxes with inlet Cr(VI) Concentrations of 20, 50 and 100 mg/L.....	113
Figure 4.36 $C/C_0$ versus time graphs for 50IR Column with 0.127 mL/cm <sup>2</sup> .min fluxes with inlet Cr(VI) Concentrations of 20, 50 and 100 mg/L.....	115
Figure 4.37 ZVI amount versus time for 50IR Column – 0.127 mL/cm <sup>2</sup> .min flux with inlet Cr(VI) concentrations of 20, 50 and 100 mg/L.....	117

Figure 4.38 ZVI reactive surface area versus time for 50IR Column – 0.127 mL/cm<sup>2</sup>.min flux with inlet Cr(VI) concentrations of 20, 50 and 100 mg/L ..... 117

Figure 4.39 Effluent mineral amounts versus time for 50IR – 0.127 mL/cm<sup>2</sup>.min flux with 50 mg/L inlet Cr(VI) concentration..... 120

Figure 4.40 Exponential function values versus time for three minerals with for 50IR – 0.127 mL/cm<sup>2</sup>.min flux with 50 mg/L inlet Cr(VI) concentration ..... 120

Figure 4.41 Passive ZVI Surface Area Fraction and Mineral Amount at the Effluent with respect to time for 50IR – 0.127 mL/cm<sup>2</sup>.min flux with 50 mg/L inlet Cr(VI) concentration ..... 121

## LIST OF ABBREVIATIONS

### ABBREVIATIONS

<i>PRBs</i>	:Permeable Reactive Barriers
<i>ZVI</i>	:Zero Valent Iron
<i>MCLs</i>	:Maximum Contaminant Levels
<i>IOCS</i>	:Iron Oxide Coated Sand
<i>Eh</i>	:Electric potential
<i>K</i>	:Equilibrium rate constant
<i>k<sub>0</sub></i>	:Zero order reaction rate constant
<i>-k<sub>obs</sub></i>	:First order reaction rate constant
<i>k<sub>eff</sub></i>	:Effective rate constant
<i>IAP</i>	: Ion activity
<i>C<sub>0</sub></i>	:Inlet concentration
<i>C<sub>t</sub></i>	:Concentration at time t
<i>t</i>	:Time
<i>A</i>	:Area
<i>S(x,t)</i>	:Reactive surface area at a location x and time t
<i>S<sub>0</sub></i>	:Initial reactive surface area
<i>α<sub>i</sub></i>	:Proportionality constant for mineral phase i
<i>φ<sub>i</sub> (x,t)</i>	:Amount of mineral phase i at a location x and time t
<i>r<sub>m</sub></i>	:Precipitation or dissolution rate of mineral m
<i>r<sub>s</sub></i>	:Rate of change in aqueous species concentration
<i>A<sub>m</sub></i>	:Reactive surface area of reacting mineral m
<i>T</i>	:Temperature
<i>a<sub>i</sub></i>	:Activity of any species occurring in mineral or aqueous reactions
<i>n</i>	:Reaction order
<i>Q<sub>s</sub></i>	:Ion activity product of an aqueous specie
<i>Q<sub>m</sub></i>	:Ion activity product of a mineral

$A_m$	:Evolving reactive surface of mineral m
$A_{0m}$	:Initial reactive surface of mineral m
$Vf_m$	:Evolving volume of mineral m
$Vf_{0m}$	:Initial volume of mineral m
$QS$	:Quartz sand
$\Phi$	:Porosity
$t_{res}$	:Residence time
$PV$	:Pore volume
$Q$	:Flux
$v$	:Fluid velocity
$D$	:Hydrodynamic dispersion coefficient
$D_L$	:Dispersion coefficient
$D_{diff}$	:Molecular diffusion coefficient
$\alpha$	:Dispersivity coefficient
$\rho_b$	:Bulk density
$EDX$	:Energy dispersive x-ray analysis
$SEM$	:Scanning Electron Microscopy
$J_{adv}$	:Advective mass flux
$J_{difs}$	:Diffusive/dispersive mass flux
$IC$	:Initial Condition
$BC$	:Boundary Condition
$R^2$	:Coefficient of determination
$MSE$	:Mean square error
$NOB$	:Number of experimental data points

## **CHAPTER 1**

### **INTRODUCTION**

#### **1.1 Background**

Ensuring access to uncontaminated drinking water is a fundamentally crucial, yet very complex issue that humanity is now struggling with. Water scarcity is an important problem in many regions, where the current water resources are inadequate to fulfill the needs of urban, industrial, agricultural, and environmental sectors.

A significant number of the Earth's aquifers are currently experiencing continuous usage and are under significant stress. Groundwater and groundwater formations are particularly valuable during intensifying scarcity because groundwater sources are often more dependable than surface water bodies in a way that the stored groundwater can increase in quantity and quality (Vaux, 2010).

Site contamination poses a serious risk to environmental sustainability in the long run. Also, site contamination issues can be considered as a missed economic opportunity on top of the possible negative effects on human health, surface and groundwater quality, and ecological processes. Anthropogenic sources of pollutants include farming and industrial processes, mining activities, accidental spills, and natural geogenic processes, the latter of which are mostly linked to metals and metalloids (Vaux, 2010).

Chromium (Cr) is a growing concern, with more research revealing trace amounts of Cr(VI) in drinking water. It is stated that Cr(VI) compounds have been assessed by several IARC (International Agency for Research on Cancer) working groups for many years. The IARC determined that there is enough evidence in humans for the

carcinogenicity of Cr(VI) compounds (EFSA, 2014). Chrome can frequently be introduced into surface and groundwater bodies through both natural and anthropogenic sources. The primary possible sources are the weathering of rocks, mudstone, microbial interactions with mafic and ultramafic rocks, and geogenic processes that naturally release Cr into the environment through chromite oxidation. Furthermore, Cr contamination is predominantly associated with wastewater and sludge generated by industrial activities, including chromate production, metal finishing, textile dyeing and processing, and leather tanning sectors. (Sorwat et al., 2021b; Prasad et al., 2021).

Chromium, as a transition heavy metal, has the highest oxidation state of +6 and the lowest oxidation states of -6. Among these oxidation states, +3 (Cr(III)) is the most stable and +6 (Cr(VI)) the second most stable state. In natural aquatic environments, Chromium compounds are stable only in these two states, each with distinct chemical properties. Cr(VI) is highly toxic, mutagenic, and carcinogenic, with high solubility and mobility, moving at a rate similar to groundwater. In contrast, Cr(III) is less toxic and remains stationary under moderately alkaline to slightly acidic conditions (U.S. Environmental Protection Agency, 2000).

According to Gheju (2011), there are various pathways hypothesized for the reduction of Cr(VI) with ZVI. However, there is a widespread agreement on the fundamental theory of Cr(VI) reduction (Karvonen, 2004). According to Melitas et al. (2001), metallic iron can reduce such heavy metals to less water-soluble oxidation states by donating electrons. Cr(VI) remediation using ZVI based PRBs consists of transforming Cr(VI) to Cr(III) while simultaneously oxidizing ZVI to form iron oxides. As a result Fe(III) and Cr(III) hydroxides or oxyhydroxides with low solubility precipitates. Depending on the experimental conditions presented with various column or batch testing and pilot scale experiments, the rate expression associated with Cr(VI) removal also changes (Gheju, 2011). Accordingly, the kinetics of Cr(VI) reduction with ZVI has been reported to follow first-order, zero-order and reaction orders less than unity (Gheju, 2011).

The literature survey reveals that the overall geochemical process associated with Cr(VI) removal with ZVI is not fully comprehended (Gheju, 2011). Numerous modeling studies have illustrated the usefulness of reactive transport models in depicting the dynamic and complex processes occurring within a PRB. Nevertheless, elements of reactivity decline due to the buildup of secondary precipitates have just lately been included into these models (Mayer et al., 2001; Jeen et al., 2007). The main research question addressed in this thesis is how to define the overall geochemical process of Cr(VI) removal using ZVI that occurs in experimental columns, particularly in relation to the passivation of the reactive media caused by secondary mineral formations. As mentioned earlier the modeling aspect of remediation process is still under development and the effect of secondary minerals on the reactive media have just lately been included into models.

Geochemical modeling is an essential instrument for the design, optimization, and comprehension of the efficacy of PRBs, facilitating successful and sustainable groundwater remediation. These models clarifies the fundamental chemical processes involved in the remediation process. These models enable researchers to forecast the behavior of reactive media over time, including aspects such as media passivation, which might influence the efficacy of the barrier. Geochemical modeling enables the evaluation of the impact of diverse factors, including pollutant concentration, flow rates, and medium properties, on the efficacy of the PRB. This facilitates more efficient and economical designs by determining the best appropriate conditions for certain site circumstances. Especially with PRB applications this design stage with modeling tools is essential because refilling or replacing the reactive media in PRBs could lead to substantial costs for materials, labor, and transportation. Over time, this can make PRBs more expensive to maintain compared to other remediation methods (Member Agencies of the Federal Remediation Technologies Roundtable, 2002).

In this regard, there is a need to develop a geochemical reaction network that involves the impact of secondary mineral formations on the reactivity of ZVI. This developed geochemical reaction network is essential for modeling work as well. This way a

modeling approach for the remediation process will be developed and presented. And consecutively, with modeling results, effective design and operation of PRB systems will be enabled.

The modeling work presented in this study is based on the lab scale column experiments conducted by Uyuşur (2006); Uyuşur and Ünlü (2009). The referred column experiments are conducted under different reactive media amounts and hydraulic conditions to assess the Cr(VI) removal efficiency with ZVI as reactive media. The experimental data presented in Uyuşur (2006); Uyuşur and Ünlü (2009) includes Cr(VI) concentration measurements at the effluent of the columns with respect to remediated number of Pore Volumes (PVs) for all the columns i.e., breakthrough curves for Cr(VI). Also, the influent and background solution compositions and the pore water velocities are presented with the experimental study. With the conditions set in experimental study the transport process is defined in the model and the model is calibrated in accordance with the breakthrough curves for Cr(VI).

## **1.2 Scope and Objective**

The literature evaluation demonstrates that researchers have improved our understanding of PRBs' longevity and effectiveness (as cited in Gui et al., 2009). Although not entirely understood, geochemical process associated with Cr(VI) removal with ZVI is extensively reviewed for Cr(VI) remediation with ZVI. Laboratory studies have examined the impact of various factors, such as, flow velocities and the quantity of reactive medium on the effectiveness of PRBs in removing contaminants and their long-term reactivity. Uyuşur (2006); Uyuşur & Ünlü (2009) studied three different ratios (w/w) of ZVI and quartz sand (QS) as reactive media within the columns (50% ZVI, 25% ZVI and 10% ZVI). Also each of these columns are operated under three different flux conditions to see the effect of varying hydraulic conditions.

Although different methodologies have been used to study the removal kinetics, the investigation of the modeling aspect of the remediation process is still underdeveloped. Significant attention has been devoted to the examination for secondary compounds that form on surface of Fe(0). However, impact of the later phases on reactive media capacity is not well understood.

In this regard, this study aims to develop a reaction network to model Cr(VI) remediation with ZVI, incorporating the surface passivation of Fe(0) due to secondary mineral precipitation. In Phreeq-C modeling applications, a reaction network refers to a set of chemical reactions and processes defined in the model to simulate the interactions and transformations of chemical species in aqueous systems. Phreeq-C uses reaction networks to model geochemical systems under varying conditions such as pH, temperature, and pressure. With this work, it is intended to understand the overall geochemical processes controlling Cr removal and the impact of the secondary minerals on the capacity of the reactive media. Using the column experiments carried out by Uyuşur (2006), reactive transport simulations of Cr(VI) removal by ZVI are conducted for their experiments considering varying groundwater fluxes and ZVI concentrations. Accordingly the objectives of this study can be listed as follows.

- to develop a kinetic reaction network that incorporates the passivation of reactive media with secondary minerals to model Cr(VI) removal process with ZVI.
- to investigate the impact of secondary mineral formation on the total reactive capacity of the ZVI under varying ZVI concentrations and varying flowrate operations.
- to conduct a sensitivity analysis on the input parameters of the model to identify the key parameters that influence the performance of the removal process under varying ZVI concentrations and flowrate conditions.
- to build predictive models to investigate the effect of different inlet Cr(VI) concentrations on the overall removal performance, ZVI reactive media amount and mineral formations.

As mentioned earlier, the design stage with modeling tools is essential in PRB systems because refilling or replacing the reactive media afterward could lead to substantial costs and over time, these substantial costs can make PRBs more expensive to maintain compared to other remediation methods. To ensure effective design and consecutively operation of PRB systems, the geochemical modeling tools can be used. These models allow researchers to predict how reactive media will behave over time, including processes like media passivation that could affect the barrier's performance. Geochemical modeling helps assess the influence of various factors, such as pollutant concentrations, flow rates, and the properties of the medium, on the effectiveness of a PRB.

Since the developed kinetic reaction network includes the surface area passivation due to secondary mineral formations, it will be possible to assess the overall effect of different secondary minerals on the reactive media. The modeling results include the concentration of the minerals precipitated over the simulation time and also mineral distributions along the columns can be seen. Since the experimental study that this modeling work is based on varying ZVI amounts and flowrate conditions, the modeling results will reveal the change in secondary mineral precipitation behaviors under these varying reactive media amounts and the flow conditions. The prediction models will be built to investigate the effect of different inlet Cr(VI) concentrations on the overall removal performance of the columns. Overall, with the listed objectives of this study, the modeling efforts in this work offer valuable insights into key geochemical processes influencing Cr removal by ZVI and are expected to enhance understanding of Cr reduction by ZVI, particularly in field applications such as iron-based PRBs.

## **CHAPTER 2**

### **LITERATURE REVIEW**

Hexavalent chromium, a heavy metal, is extensively utilized in several industrial sectors and poses a significant toxicity risk to people, animals, plants, and microbes. The global issue of chromium contamination of soil and groundwater is a major concern.

This chapter provides a brief summary of a literature survey focusing on oxidation-reduction chemistry, environmental fate and transport, as well as treatment and disposal strategies related to chromium. The literature study presented in this chapter is aimed to provide background information and current research on hexavalent chromium.

#### **2.1 Chromium in the Environment**

Chromium is the 21<sup>st</sup> element in terms of abundance in earth's crust, and is naturally present in the nature (Gallios & Vaclavikova, 2008).

Chromium, as a transition metal, has various oxidation levels. The highest and the lowest oxidation states are VI and -VI, respectively (Gheju, 2018). Within this range, the III is the most stable state, and the VI state is the second most stable state (Gheju, 2018). The other states i.e., II, IV, and V are inherently unstable and these states transform to either III or VI oxidation levels quickly (Gheju, 2018).

Due to its remarkable stability, chromium with oxidation level of III is the most common phase found in nature (Gheju, 2018). Converting Cr(III) to lower or higher forms would take a significant amount of energy (Gheju, 2018). As a result,

chromium is mostly found in its trivalent state, principally ferrous chromite ( $\text{FeOCr}_2\text{O}_3$ ), and also in smaller quantities as rare mineral ochre ( $\text{Cr}_2\text{O}_3$ ) (Gheju, 2018). Although Cr(VI) has high solubility and need for oxidation, it is the second stable form (Gheju, 2018). However, naturally occurring Cr(VI) is uncommon, such as in the mineral crocoite ( $\text{PbCr}_2\text{O}_4$ ), and is often present due to anthropogenic pollution sources (Gheju, 2018).

Chromium compounds in natural aquatic settings are stable only in III and VI levels, and these states have distinct chemical properties (U.S. Environmental Protection Agency, 2000). In environmental conditions, hexavalent chromium (Cr(VI)) is mutagenic, carcinogenic, and acutely toxic (U.S. Environmental Protection Agency, 2000). Additionally, it exhibits high solubility, mobility, and travels at a velocity comparable to that of the groundwater. Conversely, the trivalent chromium (Cr(III)), exhibits comparatively less toxicity and remains stationary when subjected to moderately alkaline to slightly acidic conditions (U.S. Environmental Protection Agency, 2000).

Chromium naturally occurs mostly in ultramafic igneous and metamorphic rocks (Chrysochoou et al., 2016). According to the investigation conducted by Chrysochoou et al., 2016, the levels of Cr(VI) in ultramafic settings show significant variation, ranging from  $< 1 \mu\text{g/L}$  to around  $70 \mu\text{g/L}$ . In groundwater Cr i.e., can be referred as geogenic, normally does not surpass  $90 \mu\text{g/L}$  total Cr or  $70 \mu\text{g/L}$  Cr(VI), in spite of the variations in geochemical circumstances in different places (Chrysochoou et al., 2016).

Turkey has chromium reserves in ultrabasic rocks, and these rocks are distributed randomly (MTA, 2022). Turkey has about 800 chrome mines and chrome ore deposits that are either single or grouped (MTA, 2022). These chrome deposits are geographically dispersed throughout 6 areas (MTA, 2022). The distribution of chrome deposits in Turkey is shown by Figure 2.1.

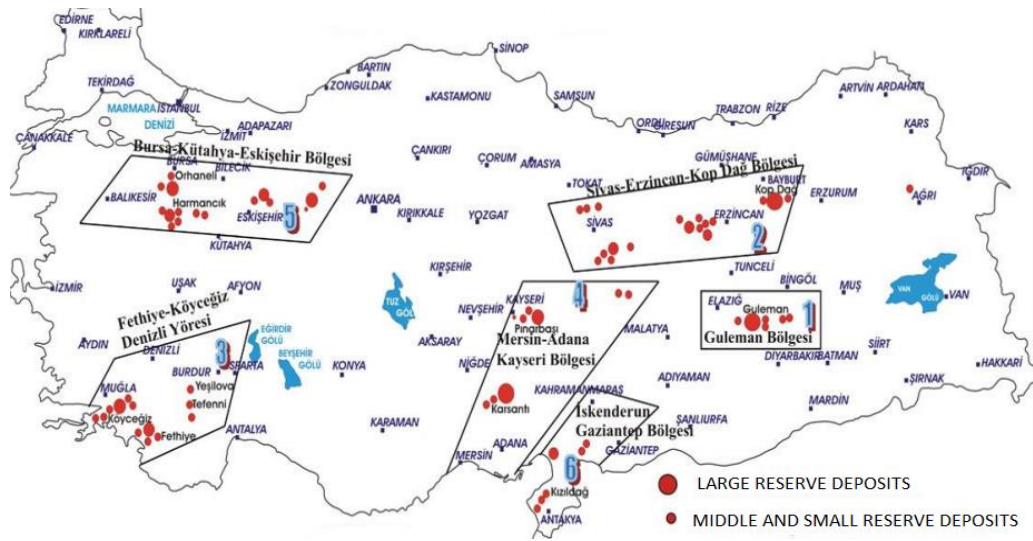


Figure 2.1 Various Chromium Deposits in Turkey (MTA, 2022)

Table 2.1 shows the state of chromium production in Turkey compared to that of other countries around the world. Turkey has a 6% share in the world chrome mining industry and 26 million tons of chrome reserves (MTA, 2022).

Table 2.1 Chromium Production in World (in thousands of tons) (USGS, 2022)

Countries	2020	2021
South Africa	13,200	18,000
Turkey	8,000	7,000
Kazakhstan	7,000	7,000
India	2,500	3,000
Finland	2,290	2,300
Others	3,980	4,100
<b>Total</b>	<b>37,000</b>	<b>41,000</b>

Chromite ore processing waste is a hazardous waste and Cr(VI) can leach to the environment through these wastes (Yalçın, 2003). Turkey being the second largest

country in chromium production, ore refining can be regarded as a significant source for contamination of soil and water systems. For instance, in the province of Mersin, there is production of inert waste and mineral wastes from enrichment facilities. The Mersin Provincial Directorate of Environment, Urbanization, and Climate Change has reported that the annual production of chromium mineral waste from enrichment facilities in 2022 is 212,540 tons (Mersin Valiliği Çevre Şehircilik ve İklim Değişikliği İl Müdürlüğü, 2022).

As stated before, Cr(VI) pollution is mostly related to industrial operations such as steel industry, chrome plating industry, textile industry, tanning industry and mining industry. Among these industries, chrome plating industry and mining industry has the highest chromium content within their effluents Karegar et al. (2015). As cited in Becker et al., (2006) study, 10 stations are sampled around a wetland to which chromite ore processing facilities are adjacent and sediment toxicity tests are conducted to the samples collected from these stations. The tests show that Chromium content for the chromite ore processing waste is between 199 – 3970 mg/kg by Becker et al. (2006). For the chrome plating industry wastewater, Cr(VI) concentration of 5721.95 mg/l is stated by Karegar et al. (2015).

Figure 2.2, shows the Electric potential (Eh) vs. pH diagram for Cr, which provides equilibrium information and illustrate the oxidation states and chemical compositions that occur within certain ranges of Eh and pH (U.S. Environmental Protection Agency, 2000). From the Figure 2.2 it can be inferred that Cr(III) is the predominating ion at pH values < 3.0. When the pH of a Cr(III)-water system exceeds 3.5, the process of hydrolysis occurs, resulting in the formation of trivalent chromium hydroxy species including  $\text{CrOH}^{+2}$ ,  $\text{Cr(OH)}_2^+$ ,  $\text{Cr(OH)}_3$ , and  $\text{Cr(OH)}_4$  (U.S. Environmental Protection Agency, 2000).

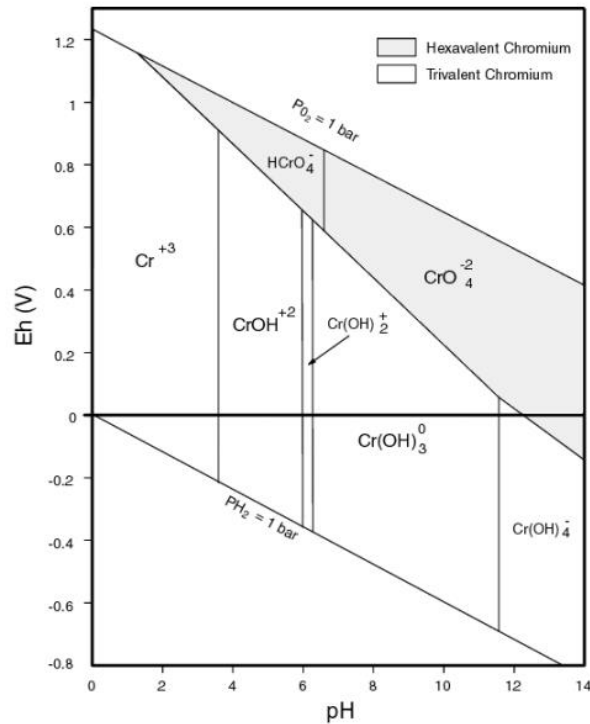


Figure 2.2 Eh vs Ph Diagram for Chromium Metal (Palmer and Wittbrodt, 1991)

Chromium is primarily released into the environment from various industrial activities, specifically: the processes of leather tanning and mordanting, the use of chromium pigments and dyes in textile industries, the ore refinement and production of substances containing chromium, the production of various types of steels, the corrosion control, the refractory industry, wood protection, galvanization, waste conveyance, and the anodizing of aluminum (Gheju, 2018). According to Chiha et al., 2006, in liquids the Cr(VI) concentration discharged from these sources ranges between 0.5 to 270,000 mg/L. Significant amounts of chromium could also be disposed to natural bodies of water as a result of inadvertent spills, leaks, inadequate storage methods, or incorrect disposal of waste associated with the usage of chromium (Zazo et al., 2008).

Figure 2.3 shows the percentage contribution of EU industries for Chromium emission in water bodies. As can be seen from the Figure 2.3, thermal power stations and other combustion facilities are the primary contributors, with waste and

wastewater treatment following closely behind. Ashes produced as a byproduct of burning coal, lignite, and municipal solid waste have a high concentration of hexavalent chromium (Tumolo et al., 2020).

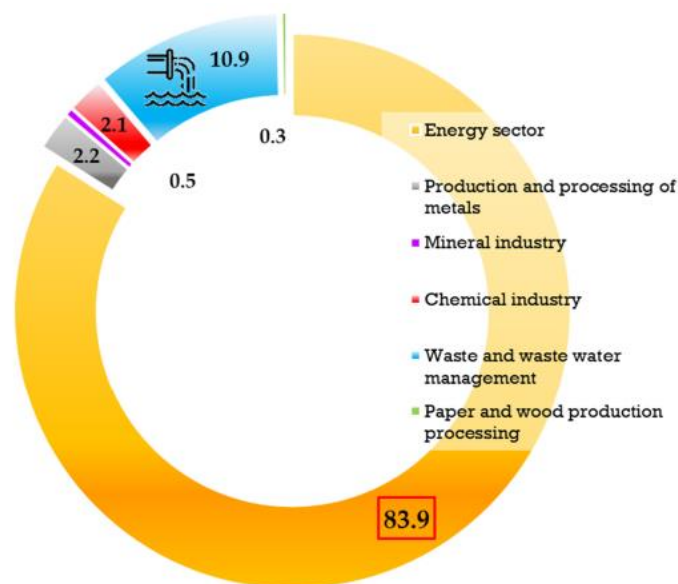


Figure 2.3 Contribution of EU Industries for Chromium Emissions in Water (Tumolo et al., 2020)

Studies on the effects of naturally occurring quantities of Cr(VI) have been scarce and recent, while the toxic and carcinogenic consequences of industrial pollution have been established since the nineteenth century (Tumolo et al., 2020).

### 2.1.1 Drinking water standards for Cr

Nationwide regulations govern chromium limits in water. The drinking water standards for total Cr are given by Table 2.2. These standards can be regarded as the maximum limit values that should be attained by various treatment methods.

Table 2.2 Drinking water standards for total Cr

Legislation	Standards
Council Directive 98/83/EC on the quality of water intended for human consumption (EU Parliament and the Council, 2020)	50 µg/L
National Primary Drinking Water Regulations (NPDWR) (U.S. Environmental Protection Agency, 2009)	100 µg/L
WHO Guidelines for drinking-water quality (WHO Team, 2022)	50 µg/L
İçme Suyu Temin Edilen Suların Kalitesi ve Arıtılması Hakkında Yönetmelik (T.C. Resmi Gazete, 2019)	50 µg/L

## 2.2 Cr(VI) Treatment Methods

Several in situ methods or procedures employ chemical reduction/fixation to remediate chromium. These methods involve geochemical fixing, PRBs, reactive zones, and natural attenuation. Chemical reduction/fixation remediation strategies aim to immobilize chromium precipitates in the aquifer system. Additional methods for the remediation of areas polluted with chromium include soil flushing/enhanced extraction, electrokinetics, and biological processes such as phytoremediation (U.S. Environmental Protection Agency, 2000). Biological processes can also utilize certain substances as substrates to facilitate remediation process and induce the Cr(VI) reduction, absorption, or precipitation. These procedures can be employed in PRBs and reactive zones. Phytoremediation is another method that use the ability of plants to absorb chromium pollution as a treatment method that takes place on-site (U.S. Environmental Protection Agency, 2000).

Other than the methods mentioned above, there exists another technique that can be implemented at numerous locations which is called pump-and-treat technology. Pump-and-treat method basically operates by removing polluted groundwater, often

over extended durations, and implementing hydraulic measures to restrict the spread of contaminants (U.S. Environmental Protection Agency, 2000). It should be mentioned that with pump-and-treat technology, at first the effluent's pollution levels are high, whereas with the continuation of pumping, the pollution concentration levels are lowered considerably. It should be noted that the concentrations of these residuals can stay above the Maximum Contaminant Levels (MCLs) and can persist for extended durations, a phenomenon known as "tailing" (U.S. Environmental Protection Agency, 2000).

Research during the last two decades has mostly concentrated on advancing more towards in situ technology. The number of remediation methods and their uses has expanded recently due to advancements in technical knowledge, inventive concepts, technical and economic resources, and increasingly complicated site concerns (Hyman and Dupont, 2001; Leeson et al., 2013; Naidu, 2013 as cited in Naidu & Birke, 2015). One parameter that can be used to compare the remediation technologies with each other is the cost. However developing meaningful comparisons of remediation technology's costs is challenging due to several factors. These reasons are summarized below (Naidu & Birke, 2015).

- Technology costs are highly susceptible to site-specific geological, geochemical, and contaminant conditions, particularly in the case of in situ technologies. Costs are reported under a unique set of local conditions (Naidu & Birke, 2015).
- The metrics used to report costs by vendors include costs per volume of contaminant treated, decrease in pollutant concentrations, reduction in contaminant mobility, mass of contaminant eliminated, or surface area treated. This variance in metrics make comparison difficult (Naidu & Birke, 2015).
- The vendors only provide fixed costs, not variable expenses. If the user is just interested in comparing the cost of installed operations, this approach may be appropriate. However, often the user is more concerned with the

whole project cost. Remediation systems with high and fluctuating initial costs may not be cost-effective, even if their operational costs seem reasonable (Naidu & Birke, 2015).

- Comparing unit costs is only meaningful if there is consistency in the procedures and assumptions used to calculate them. Using varying interest rates to calculate the expenses of a cleaning system throughout its full life cycle might lead to very different results on the cost competitiveness of a technology (Naidu & Birke, 2015).

PRB, when applicable, is more cost-effective than ex situ technology since it does not incur operating and maintenance expenses (Naidu & Birke, 2015). A PRB is a sustainable groundwater remediation method that aligns with green practices and is considered one of the most environmentally friendly techniques, second only to monitored natural attenuations (Naidu & Birke, 2015). Reactive materials often consist of waste items such as mulch, sawdust, and some iron ore slags, or recovered materials such as iron scrap (Naidu & Birke, 2015). Therefore, PRBs have been receiving considerable attention recently in the United States and Europe (Naidu & Birke, 2015).

The effectiveness and durability of a PRB system depends on the design phase, as there is less opportunity to make corrections after the system is constructed (Naidu & Birke, 2015). Therefore, it is crucial to conduct a thorough high-resolution site analysis to comprehend the plume's nature and extent, choose the appropriate reactive material, design the hydraulic system, and assess the vertical spread of pollution (Naidu & Birke, 2015). PRB remediation technology is advancing with the introduction of new and creative reactive materials to address various pollutants using novel building methods (Naidu & Birke, 2015).

### **2.2.1 Permeable Reactive Barrier (PRBs) Technology**

In situ reactive barriers consist of a permeable reactive substance that passively eliminates contaminants from incoming groundwater. The barriers do not need continuous maintenance or energy input, and above-ground treatment and discharge of groundwater is unnecessary. PRB technology works by placing reactive barriers filled with reactive media at a right angle with respect to the polluted groundwater path (Powell et al., 1998). According to Song et al., (2021), with the help of the natural hydraulic gradient the contaminated plume moves through the media. Pollutants interact with the media and transform into non-hazardous and more stable chemicals or they attach to the reactive media.

Various treatment methodologies have been developed to eliminate heavy metals from water sources. Underground Permeable Reactive Barriers (PRBs) have received significant attention as a remedial solution in recent times. This is because of the projected cost-benefit ratio of PRBs and their ability to reduce the spread of toxins that have been challenging and costly (Batelle Memorial Institute, 2012). PRBs at three Navy installations were assessed for cost and benefit by Batelle Memorial Institute (2012). While the installation cost for Pump and Treat technology is stated to be around \$7,000,000, the installation cost of PRBs is around \$1,000,000. The normalized treatment costs for PRBs i.e., the cost per groundwater treated, is stated to be around \$ 4 / 1,000 gals and for the pump and treat technology, it is stated to be \$ 8 / 1,000 gals (Batelle Memorial Institute, 2012). So there is a significant difference between these two technologies in terms of normalized treatment costs and the normalized treatment cost associated with the PRBs is half of the normalized cost for Pump and Treat technology (Batelle Memorial Institute, 2012).

To accomplish their remediation objectives, PRBs must perform two functions: (1) intercept polluted groundwater plumes and (2) reduce pollutant concentrations to levels below regulatory limits or remediation targets (Bilardi et al., 2023). The primary performance concern of the PRB systems is the capacity of the PRB to stop

the target pollution from spreading beyond the plume cutoff position and lowering the risk to downgradient receptors (Member Agencies of the Federal Remediation Technologies Roundtable, 2002). Longevity of PRB system, or the question of how long a PRB can keep its reactive and hydraulic performance, is the primary performance problem in the long run. Due to native groundwater component precipitation, granular zerovalent iron reactivity decreases with time and this is considered as long run performance issue (Member Agencies of the Federal Remediation Technologies Roundtable, 2002).

The infill material within PRB is referred to as reactive medium. The choice and utilization of reactive medium materials are mostly based on contaminants and their associated processes. However, hydrogeological parameters like pH, ion strength, and coexisting ions can sometimes restrict the usage of certain materials. The reagent's permeability must be equivalent or greater than the surrounding aquifer permeability (Faisal et al., 2020 as cited in Song et al., 2021). The amount of the filled material must be carefully determined to ensure the proper permeability for the reaction involved in removing contaminants. Preserving adequate hydraulic conductivity within the medium is what sets apart the filled material used in PRB systems. The structured response coming from the reactive medium in PRB is vital in elimination of heavy metals from groundwater. (Song et al., 2021).

ZVI, as a reactive medium, has been widely used for enhanced removal of materials from aqueous solutions by virtue of its exceptional reductivity and adsorption capabilities. The attention on ZVI materials has shifted from single materials to composite materials and materials combined with microorganisms (Song et al., 2021).

The advantage and disadvantage of ZVI and other primary materials often utilized in PRBs are outlined in Table 2.3.

Table 2.3 Pros and cons of different reactive materials used in PRBs and related utilization situations (Song et al., 2021)

Reactive Materials in PRBs	Advantages	Disadvantages	Utilization Situations
ZVI	<ul style="list-style-type: none"> <li>✓ high surface area;</li> <li>✓ excellent reducibility;</li> <li>✓ iron-oxides adsorption and oxidation on ZVI surface</li> </ul>	<ul style="list-style-type: none"> <li>✓ aggregation;</li> <li>✓ passivation causing reduced capacity;</li> <li>✓ small size leading to clogging</li> </ul>	<ul style="list-style-type: none"> <li>✓ reduced environment;</li> <li>✓ low hydraulic conditions;</li> <li>✓ best at close to neutral or slightly acidic circumstances</li> </ul>
Metal (hydro)Oxides/Sulfides	<ul style="list-style-type: none"> <li>✓ strong adsorption;</li> <li>✓ precipitation onto metal(oids) by hydroxyl ion or sulfide;</li> <li>✓ possessing ion exchange ability;</li> <li>✓ neutralizing acidic surroundings</li> </ul>	<ul style="list-style-type: none"> <li>✓ oxidation in aerobic conditions for example FeS results in restricted operational conditions;</li> <li>✓ Small size affects hydraulic conductivity</li> </ul>	<ul style="list-style-type: none"> <li>✓ reducing environment for metal sulfide</li> </ul>

**Table 2.3 (Continued)**

<b>Reactive Materials in PRBs</b>	<b>Advantages</b>	<b>Disadvantages</b>	<b>Utilization Situations</b>
Industrial Waste	<ul style="list-style-type: none"> <li>✓ broad sources;</li> <li>✓ economical;</li> <li>✓ adsorption by a large specific surface area;</li> <li>✓ high mechanical strength</li> </ul>	<ul style="list-style-type: none"> <li>✓ complex chemical constituents;</li> <li>✓ possible further contamination;</li> <li>✓ restricted treatment effectiveness</li> </ul>	<ul style="list-style-type: none"> <li>✓ adapting to different hydrological conditions and low pollution concentrations</li> </ul>
Ion Exchange Resin	<ul style="list-style-type: none"> <li>✓ high ion exchange capacity;</li> <li>✓ outstanding removal effectiveness</li> </ul>	<ul style="list-style-type: none"> <li>✓ reversible adsorption process;</li> <li>✓ expensive</li> </ul>	<ul style="list-style-type: none"> <li>✓ lower hydrodynamic conditions;</li> <li>✓ consistent components of treated plume</li> </ul>
Organic Polymers	<ul style="list-style-type: none"> <li>✓ high specific surface area;</li> <li>✓ porous structure;</li> <li>✓ biodegradable materials like chitosan;</li> </ul>	<ul style="list-style-type: none"> <li>✓ costly preparation method;</li> <li>✓ challenges in maintaining hydraulic conductivity</li> </ul>	<ul style="list-style-type: none"> <li>✓ low hydraulic state</li> </ul>

**Table 2.3 (Continued)**

<b>Reactive Materials in PRBs</b>	<b>Advantages</b>	<b>Disadvantages</b>	<b>Utilization Situations</b>
Carbonaceous Materials	<ul style="list-style-type: none"> <li>✓ substantial surface area;</li> <li>✓ porous structure;</li> <li>✓ chelation with metal ions;</li> </ul>	<ul style="list-style-type: none"> <li>✓ costly preparation procedure;</li> <li>✓ low mechanical strength</li> </ul>	<ul style="list-style-type: none"> <li>✓ adjusting to different hydraulic conditions</li> <li>✓ lower pollutant concentration</li> </ul>
Microorganism related Materials	<ul style="list-style-type: none"> <li>✓ redox capacity;</li> <li>✓ enhancing electron transport;</li> <li>✓ adsorption via secretions;</li> <li>✓ cost-effective operation</li> </ul>	<ul style="list-style-type: none"> <li>✓ appropriate culture environment;</li> <li>✓ extended development of culture;</li> <li>✓ supplementary nutritional provision</li> </ul>	<ul style="list-style-type: none"> <li>✓ combined pollution consists of both inorganic and organic materials in low hydraulic conditions,</li> <li>✓ forming stable chemicals inside the remediated plume.</li> </ul>

ZVI has been the most frequently used as reactive agent in both lab scale experiments and real-world applications for remedial purposes (Obiri-Nyarko et al., 2014). Between 1994 and 2005, almost 200 PRB apps were created in Europe, North America, and Australia, with 120 of them being ZVI-based. According to Wu et al., (2020), ZVI is considered as a propitious option due to its powerful reduction capability, cost-effectiveness, ecological compatibility, and easy separability. ZVI core-shell materials are fabricated by the coating and building of core-shell structures

(Song et al., 2021). The significant limitations associated with ZVI include deactivation due to mineral build up on the reactive media. In this regard using ZVI as a single reactive material in PRBs has been questioned. Table 2.4 outlines the pros and cons of several applications including ZVI.

Table 2.4 Comparing different uses of ZVI (Song et al., 2021)

<b>Forms of ZVI</b>	<b>Advantages</b>	<b>Disadvantages</b>
Single ZVI	High surface area; excellent adsorption and reducibility; easy preparation method	Agglomeration, passivation, inadequate size for PRBs.
Mixed ZVI	Basic preparation method including mechanical mixing; reduction of clumping; enhanced elimination of contaminants in combination with other solid materials; preservation of hydraulic conductivity	inefficient elimination; inactivation; obstruction; primary adsorption mechanism
Core-shell ZVI	Reducing aggregation by creating a core-shell structure; using the reducibility of ZVI in a synergistic manner to form a big composite material; multiple mechanisms	Complex preparation procedure; expensive; requires many chemical agents; risk of secondary contamination

According to Melitas et al., (2001), metals in a zero-valence state, such as iron, operate as source for electrons to convert redox active metals into metals with low solubility. According to Scherer et al., (2000), iron can be considered as a strong reducing agent due to the low standard potential of the  $Fe^0 - Fe^{2+}$  pair. The

appropriateness of reagents with ZVI base for remediation is also determined by nonviscous and porous quality of some iron corrosion products. These products cause corrosion to pursue till exhaustion of ZVI (Noubactep & Schöner, 2010). For Cr(VI) reduction, ZVI-based alloys are suitable because of their non-adhesive and porous properties, which cause the corrosion to persist until ZVI is depleted (Noubactep & Schöner, 2009).

### **2.2.1.1 Reduction Mechanism for Cr(VI)**

The redox processes involving Cr(VI) removal with Fe(0) are not completely acknowledged. Yet, a widespread agreement on the fundamental theory of Cr(VI) reduction has been evolving (Karvonen, 2004). Metallic iron and other zero-valence metals can reduce redox active metals to less water-soluble valence states by donating electrons (Melitas et al., 2001).

The process of electrochemical corrosion happens when iron metal is submerged in water. Iron releases electrons, creating soluble cations, and oxidized species pick them up, becoming reduced (Powell et al., 1998). As long as oxygen is present, aerobic corrosion of iron occurs quickly, but anaerobic corrosion takes much longer (Tarr, 2003). Due to the anaerobic conditions in most PRB applications and due to encountered pH ranges in natural water bodies, ZVI dissolution rate is overly slow. The main impact factor pH, affects the circumstances for the formation of iron oxides (Noubactep & Schöner 2010). ZVI corrosions under both anaerobic and aerobic conditions cause a drop in redox potential and a rise in solution pH.

For Cr(VI) reduction with ZVI reagents, multiple routes have been proposed. The first step, known as heterogeneous (direct) Cr(VI) reduction, entails electron transfer from the ZVI surface to Cr (Gheju, 2011). According to Fiuza et al. (2010), Cr(VI) reduction can occur through various steps as follows:

- 1) At the solid-liquid interface Cr(VI) movement occur between bulk solution and ZVI surface passing the Nernst boundary layer and Cr(VI) attaches to the unreacted surface of ZVI.
- 2) Chromium (VI) is reduced at the ZVI surface, leading to mixed Fe(III) and Cr(III) hydroxides or oxyhydroxides precipitates.
- 3) Some reduced forms attach/detach from media surface. The detached reduction products are carried to the bulk solution.

The three steps described by Fiuza et al., (2010) are illustrated in Figure 2.4. After the adsorption and consecutive reduction process, Cr(III) and Fe(III) (oxy)hydroxide precipitates are formed. This final product is adsorbed onto or desorbed from the ZVI surface.

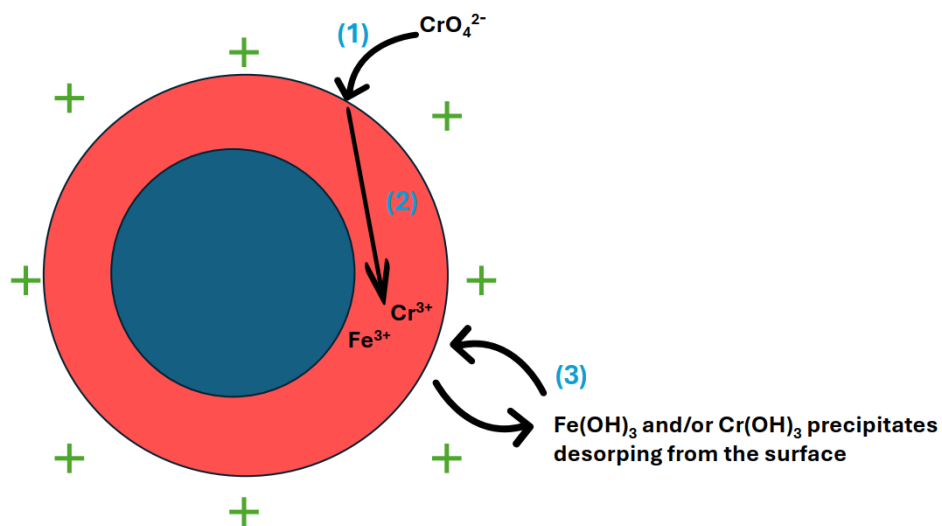
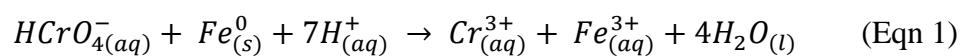
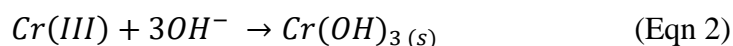


Figure 2.4 Illustration of the process of adsorption-reduction taking place when Cr(VI) is reduced by ZVI (Adapted from Fiuza et al., (2010))

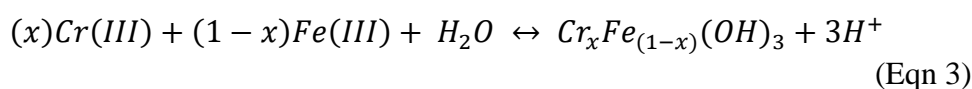
The second process, known as homogeneous (indirect) Cr(VI) reduction, occurs when dissolved  $Fe^{2+}$  ions reduce Cr(VI). When ZVI reduces Cr(VI) either directly or indirectly, the overall reaction can be written as follows (Gheju, 2011):



According to Blowes et al. (1997), when Cr(III) is produced, either absorption onto the Fe(0) surface or precipitates as a solid occurs in the solution. The critical i.e., slow, step frequently involves production of the Cr(III) precipitate. This is usually a hydrolyzed chromium species or a Cr(III) compound bound to OH<sup>-</sup> ions shown as follows.



At 25°C, constant for product solubility i.e., K<sub>sp</sub>, of Cr(OH)<sub>3</sub> is 6.3 × 10<sup>-31</sup>, and it precipitates easily when the pH is above 7. Additionally, mixed Fe (III) and Cr (III) hydroxides can be formed as precipitates. Both of these precipitates typically have low solubility. The formation of Fe (III) and Cr (III) hydroxide or oxyhydroxide precipitate is as follows (Gheju, 2011).



Under circumstances where pH value is greater than or equal to 7.0, Fe(III), Fe(II), and Cr(III) compounds formed during reduction of Cr(VI) are therefore eliminated from water by precipitating as basic hydroxides or co-precipitating as oxyhydroxides (Gheju, 2011).

During oxide film formation, Cr(VI) becomes trapped within the iron oxides by coprecipitation. It may not be possible to completely decrease Cr(VI) within ZVI and H<sub>2</sub>O systems, but it can be effectively removed and securely trapped inside ZVI corrosion products (Noubactep, 2010). Multiple investigations have shown a significant decline in reduction rates during the second time period of Cr(VI) remediation, after substantial reduction rates in the initial interval. This behavior is likely due to the formation of Fe(III)/Cr(III) hydroxides and oxyhydroxides or secondary phases, which are responsible for preventing Cr(VI) ions from reaching the iron surface (Gheju, 2011).

Several lab and field scale studies for Cr(VI) remediation by Fe(0) have been carried out (Melitas et al., 2001; Mayer et al., 2001; Kaplan & Gilmore, 2004; Gui et al.,

2009; Wanner et al., 2011). These studies have indicated that Cr(VI) reduction and precipitation rate are adequate for application in ground-water remediation systems. When Cr(VI) is eliminated from the system, Eh decreases sharply from initially oxidized circumstances ( $Eh > 100$  mV) to extremely reduced conditions ( $Eh < -300$  mV), and the pH increases sharply from originally near neutral settings ( $6.5 < pH < 8.5$ ) to more basic conditions ( $pH > 9.5$ ) (Powell et al., 1998).

The chromium solid-phase interactions were studied in materials retrieved from a full-scale zerovalent iron PRB application study situated near Elizabeth City, NC, at the US Coast Guard Support Center (Wilkin et al., 2005). The core minerals collected from the in the PRB system were examined with scanning electron microscopy, where the presence of various minerals as calcite/aragonite, iron carbonate hydroxides, magnetite, lepidocrocite, ferrihydrite, mackinawite, and carbonate green rust were reported based on mineralogical analysis (Wilkin et al., 2005). Main Fe observed at the downgradient boundary suggested minimal to no secondary phase formations at these downgradient locations (Wilkin et al., 2005). The reduction in pore space was mainly caused by the production of carbonate precipitates, sulfide precipitates, and the byproducts of iron-metal oxidation, where the accumulation of mineral precipitates affected the hydraulic efficiency of PRBs adversely (Wilkin et al., 2005). Several carbonate minerals, such as calcite ( $CaCO_3$ ), aragonite ( $CaCO_3$ ), and siderite ( $FeCO_3$ ), are frequently observed on Fe(0) surfaces (Kaplan & Gilmore, 2004). Carbonate minerals are created as dissolved carbonate level rises while pH is increasing, caused by consumption of protons during the redox process (Kaplan & Gilmore, 2004).

#### **2.2.1.1.1 Cr(VI) Reduction Kinetics**

Cr(VI) removal kinetics with different ZVI forms have been investigated by various studies (Gheju, 2011). Some studies have calculated the reaction order, while other studies have begun the kinetic investigations by assuming that the reduction followed

a first order kinetic model. Reduction kinetics might vary under different experimental settings, being described as first or zero order or having a order less than one. The referred rate expressions are explained as follows.

The rate associated with chromate removal by ZVI is represented by first order kinetic equation as shown below (Alowitz & Scherer, 2002; Kaplan & Gilmore, 2004).

$$\frac{dC_{Cr(VI)}}{dt} = -k_{obs} \cdot C_{Cr(VI)} \quad (\text{Eqn 4})$$

where  $k_{obs}$  is the reaction rate constant for a first order (1/s), dissolved Cr(VI) is denoted as  $C_{Cr(VI)}$  (mol/L) and the contact time between species is denoted by  $t$  (s). Integration of this equation yields to the following equation:

$$C_t = C_0 \cdot e^{-k_{obs}t} \quad (\text{Eqn 5})$$

Gould (1982) conducted a kinetic study using relatively pure ZVI metallic iron with respect to different circumstances in batch reactors. According to their study, Cr(VI) removal depended on Cr(VI) and H<sup>+</sup> concentrations and reagent ZVI surface area. Cr(VI) reduction rate was 0.5 order in terms of Cr(VI) and H<sub>3</sub>O<sup>+</sup> concentrations, and first order with respect to the reagent surface area, as expressed in the equation below:

$$\frac{dC_{Cr(VI)}}{dt} = -k \times [Cr^{6+}]^{0.5} \times [H_3O^+]^{0.5} \times S_{Fe(0)} \quad (\text{Eqn 6})$$

where,  $k$  is the reaction rate constant (L/cm<sup>2</sup>.min) for the mixed-order reaction rate,  $[Cr^{6+}]$  and  $[H_3O^+]$  are the Cr(VI) and hydronium concentrations (mol/L) and  $S_{Fe(0)}$  is the surface area of iron (cm<sup>2</sup>/L) (Gould, 1982; Melitas et al., 2001; Mayer et al., 2001; Kaplan & Gilmore, 2004; Gui et al., 2009).

Plenty of researchers have conducted studies on reduction kinetics utilizing various ZVI forms under varied preliminary experiment settings (Gheju, 2011). In general, the reduction kinetics with ZVI as reagent might were observed to vary depending

on the experimental circumstances, with reported reaction orders ranging from first-order, zero-order, to even less than unity. The study conducted by Melitas et al. (2001) investigated Cr(VI) removal using both batch reactors and packed column experiments, where their column reactors were run with 100 to 10,000  $\mu\text{g/L}$  Cr(VI) concentrations and  $\text{CaSO}_4$  was used as background solution in their experiments. Their study reported a zero-order kinetic model to describe their Cr(VI) removal process in their experiments. In another study conducted by Mayer et al. (2001), field data from PRB installation at a US Coast Guard Support Center field site located in North Carolina region was used. Their multicomponent reactive transport model included Cr(VI) removal kinetics of 0.5 order in terms of Cr(VI) and  $\text{H}^+$  concentrations, as described above.

Kaplan & Gilmore (2004) conducted a column study similar to Uyuşur's (2006) study. The study investigated three combinations of sand and Fe(0) with different weight percentages of Fe(0): 20%, 50%, and 100%. Additionally, three types of aqueous phases were assessed: deionized water, a 0.2 M  $\text{NaHCO}_3$  aqueous solution, and state groundwater. A solution containing 5 mg/L of Cr(VI), which was prepared using potassium dichromate ( $\text{K}_2\text{Cr}_2\text{O}_7$ ), was added to the column. Their results showed that the reactivity of Fe(0) significantly changed when its surface was coated by secondary mineral layers that developed during the Fe(0) oxidation reactions. Magnetite ( $\text{Fe}_3\text{O}_4$ ), green rust ( $\text{Fe}_{6-x}^{\text{II}}\text{Fe}_x^{\text{III}}(\text{OH})_{12}\text{CO}_3 \cdot y\text{H}_2\text{O}$ ), goethite ( $\text{FeOOH}$ ), and ferric hydroxide ( $\text{Fe}(\text{OH})_3$ ), as well as several carbonate minerals, including calcite ( $\text{CaCO}_3$ ), aragonite ( $\text{CaCO}_3$ ), and siderite ( $\text{FeCO}_3$ ) phases were observed on the Fe(0) surfaces.

Gui et al. (2009) conducted column experiments for Cr(VI) removal using either 10 mg/L of Cr(VI) or 10 mg/L of Cr(VI) combined with 300 mg/L of  $\text{CaCO}_3$  solutions. Their removal kinetics were also expressed with Cr(VI) removal kinetics of 0.5 order in terms of Cr(VI) and  $\text{H}^+$  concentrations, and the reactive surface area of Fe(0) was modified based on the secondary minerals present.

Wanner et al. (2011) also conducted column experiments with 1 mg/L of inlet Cr(VI) to investigate Cr removal by ZVI. Their mineral precipitation and dissolution were kinetically expressed based on the transition state theory. During mineral precipitation and dissolution processes, both the volume fractions and reactive surfaces of minerals resulted in irreversible alterations. Their reactive model modified the surface area of the minerals based on the evolving volume fractions in the experiments (Wanner et al., 2011).

The literature review shows significant advancements in the understanding of PRBs and the use of ZVI reactive media for remediating Cr(VI). Scientists have enhanced the comprehension of the durability and efficiency of PRBs. Current research is rather more being conducted on emerging reactive media. The chemistry of corroding iron has been widely investigated in relation to the remediation of Cr(VI) with ZVI, although it is not fully comprehended. Considerable attention has been dedicated to the examination of secondary precipitates formed on the surfaces of the reactive media, ZVI. However, studies on the impact of secondary phases on the overall capacity of the reactive media are still limited. Compared to other studies presented under this section, this modeling work includes the investigation of removal performance under both varying reactive media amounts and flowrate conditions. Also as mentioned earlier, this modeling work relies on the experimental data presented by Uyuşur (2006); Uyuşur and Ünlü (2009). In this regard, the developed kinetic reaction network is specific to the conditions set in the referred experimental study, where the influent and background solution compositions set in the experimental study are rather simple compared to the other reactive transport modeling studies (Wanner et al., 2011; Gui et al., 2009; Mayer et al., 2001). Therefore, this study is different than the presented literature studies in terms of kinetic reaction network, the solution compositions and overall modeling approach.

This study mainly focuses on the four aspects of Cr(VI) remediation from groundwater bodies. These aspects are summarized as follows: (1) developing a kinetic reaction rate approach that integrates the passivation of reactive media with

secondary minerals and its effects on the reactive medium, specifically zero-valent iron. Modeling is a powerful tool to depict the removal mechanism behind the remediation process and to present a reaction network related to the proposed removal mechanism. (2) Investigating the impact of secondary mineral formation on the total reactive capacity of the ZVI under varying ZVI concentrations and varying flowrate operations. The literature review indicates that the effect of secondary minerals on the overall capacity of zero-valent iron (ZVI) is currently under investigation. (3) Conducting a sensitivity analysis on the input parameters of the model. The literature review shows that the input parameters used in the model works are not assessed within a certain range. By conducting a sensitivity analysis with the calibrated models, it will be possible to see the effect of different input parameters on the removal process. (4) Building prediction models to investigate the effect of different inlet Cr(VI) concentrations on the overall removal performance. In this regard, the model response to the change in inlet Cr(VI) concentrations are to be assessed in terms of removal performance, reactive media amount and mineral formations.

Therefore the modelling efforts presented in this study would provide insights on the important geochemical processes affecting Cr removal by ZVI; and is expected to shed light in modeling Cr reduction by iron-based removal technologies, such as permeable reactive barrier applications in the field.



## CHAPTER 3

### MATERIALS AND METHODS

#### 3.1 Modeling Approach and Description of Experimental Studies

In this study, a reaction network related to the removal mechanism of Cr(VI) by ZVI is presented. A kinetic reaction rate approach is developed that integrates the passivation of reactive media with evolving secondary minerals, where the impact of the decrease in ZVI reactive surface on the Cr removal efficiency is demonstrated with varying amounts of ZVI and varying flow rates used in the system. The conceptual model and chemical reaction network developed in this work is based on the lab scale column experiments conducted by Uyuşur (2006); Uyuşur and Ünlü (2009).

The lab experiments consisted of 15 cm long and 7 cm<sup>2</sup> cross section area of column set-ups. The packed material consisted of three different ratios (w/w) for iron powder and quartz sand mixture: 50% ZVI, 25% ZVI and 10% ZVI. The ZVI powder was mixed with inert quartz sand and it then is used as packing material for the columns. The iron powder had a particle density of 7.87 g/cm<sup>3</sup> and a BET specific surface area of 0.04 m<sup>2</sup>/g (Uyuşur, 2006). Also there was a control column with 100 % quartz sand (QS). Three sets of experiments were conducted with each column with varying flowrates. The hydraulic properties of each set is presented by Table 3.1. These properties are regarded as input parameters of the model (Uyuşur, 2006). The ZVI amount is calculated by given pore volume, specific surface area of the ZVI and ratio between surface area of iron and solution volume. It should be mentioned that the model simulations are based on the 1D reactive transport processes and only the length of the columns can be defined in the model. The reactive media amount is an

important model input parameter and it is not stated explicitly in the experimental study. Therefore, from the given data related to the reactive media, the reactive media amount in moles are calculated for each simulated columns. Sample calculation for the 50IR column is given below. The cross sectional area of the columns are taken as 1 cm<sup>2</sup>. It is known that the cross sectional area of the columns is 7 cm<sup>2</sup>. In this regard, the amount of reactive media is divided by 7.

It should be mentioned that among the columns presented in Table 3.1, only 10IR and 25IR Columns with 0.07 and 0.127 mL/cm<sup>2</sup>.min fluxes and 50IR Column with 0.127 mL/cm<sup>2</sup>.min flux are simulated.

### **1<sup>st</sup> Step**

$$C_{ZVI}(g/mL) = \frac{\text{Surface Area of Fe to Volume of Solution Ratio (m}^2/mL)}{\text{Specific Surface Area of Iron (m}^2/g)} \quad (\text{Eqn 7})$$

$$C_{ZVI}(g/mL) = \frac{0.065 \text{ m}^2/mL}{0.04 \text{ m}^2/g} = 1.63 \text{ g/mL}$$

### **2<sup>nd</sup> Step**

$$ZVI \text{ Amount (g)} = C_{ZVI}(g/mL) \times \text{Pore Volume (mL)} \quad (\text{Eqn 8})$$

$$ZVI \text{ Amount (g)} = 1.63 \text{ g/mL} \times 64.3 \text{ mL} = 104.49 \text{ g}$$

### **3<sup>rd</sup> Step**

$$ZVI \text{ Amount (moles)} = \frac{ZVI \text{ Amount (g)}}{\text{Molecular Weight of Fe (g/moles)}} \quad (\text{Eqn 9})$$

$$ZVI \text{ Amount (moles)} = \frac{104.49 \text{ g}}{55.845 \text{ g/moles}} = 1.87 \text{ moles}$$

$$\frac{ZVI \text{ Amount (moles)}}{7} = \frac{1.87 \text{ moles}}{7} = \mathbf{0.267 \text{ moles}}$$

Table 3.1 The hydraulic properties of the columns (Uyuşur, 2006)

	50IR			25IR			10IR			100QS
<b>Flux (Q) (mL/cm<sup>2</sup>.min) (q)</b>	0.07	0.127	0.17	0.07	0.127	0.057	0.07	0.127	0.057	0.057
<b>Flow velocity (v) (cm/day)</b>	153.8	260.19	389.19	181.44	335.08	129.74	196.13	340.03	148.62	180.24
<b>Flow velocity (v) (m/year)</b>	561.37	982.55	1420.6	662.25	1223	473.57	715.87	1241.1	542.48	657.9
<b>Residence time (t<sub>res</sub>) (hour)</b>	2.34	1.38	0.92	1.98	1.07	2.77	1.84	1.06	2.42	2
<b>Dispersion coeff. (D) (cm<sup>2</sup>/min)</b>	1.53	0.947	2.9	0.316	0.266	0.021	1.579	0.0252	0.0209	0.0789
<b>Pore Volume (PV) (mL)</b>	64.3	64.3	64.3	53.7	53.7	53.7	49.8	49.8	49.8	47.9
<b>Porosity (<math>\phi</math>)</b>	0.628	0.628	0.628	0.524	0.524	0.524	0.486	0.486	0.486	0.452
<b>Bulk density (<math>\rho_b</math>) (g/cm<sup>3</sup>)</b>	1.96	1.96	1.96	1.883	1.883	1.883	1.629	1.629	1.629	1.452
<b>Ratio between Volume of Solution and ZVI Surface Area (<math>\rho_m</math>) (m<sup>2</sup>/mL)</b>	0.065	0.065	0.065	0.0365	0.0365	0.0365	0.0137	0.0137	0.0137	NA
<b>Surface Area of Iron (A) (m<sup>2</sup>)</b>	4.178	4.178	4.178	1.96	1.96	1.96	0.682	0.682	0.682	NA
<b>Specific Surface Area of Iron (m<sup>2</sup>/g)</b>	0.04	0.04	0.04	0.04	0.04	0.04	0.04	0.04	0.04	NA
<b>Initial ZVI Amount (moles)</b>	0.267	0.267	0.267	0.124	0.124	0.124	0.0429	0.0429	0.0429	NA

### 3.1.1 Interpretation of Column Experiments

According to the results obtained with column experiments, the sole removal mechanism for Cr(VI) is through redox reactions with ZVI in the system. Cr(VI) removal because of adsorption on sand particles or iron oxides did not take place under the set conditions. Actually, the possibility of adsorption onto produced iron oxides was tested by sequential water and phosphate removals. and it was determined that that no Cr(VI) removal took place(Uyuşur, 2006).

An important drawback related with reactive iron barrier was stated as solidification of ZVI reagent due to the formation of precipitated phases. The ZVI surface morphology was analyzed using surface analytic techniques in order to detect the reaction products (Uyuşur, 2006). The presence of these precipitates was identified using Scanning Electron Microscopy (SEM) and Energy Dispersive X-Ray Analysis (EDX). It was stated that through analysis and visual observations, the presence of ferrihydrite could be deduced from the coating on the specific surface of the samples. The mineral phases that were expected to form consist of mixed Cr(III)-Fe(III) (oxy)hydroxide solids, various Fe oxides, hydroxides, and oxyhydroxides and carbonate precipitates such as siderite ( $\text{FeCO}_3$ ), aragonite/calcite ( $\text{CaCO}_3$ ). The formation of these carbonate precipitates was linked to the high concentration of carbonate in the background solution (Uyuşur, 2006).

It was stated that the minerals formed and the possible generation of gaseous hydrogen didn't have a substantial effect on the porosity and, as a result, the system's hydraulic performance. It was also stated that since the columns were relatively short i.e., 15 cm in length, higher flowrates were generated compared to field scale conditions, and thus cementation in reactive media wasn't serious in the study (Uyuşur, 2006).

The results of the experimental study showed that the column with 50% ZVI showed the maximum treatment efficiency. The results obtained from different groundwater fluxes were compared and it was inferred that when flux increased, the minerals

blocking the unreacted surface might not buildup and this results in more surface area ready to use for reduction. At lower fluxes thicker oxide films were produced and the film could have intercepted Cr(VI) diffusion transfer within the column (Uyuşur, 2006).

Overall, the experiments were conducted to measure and analyse the effects of different hydraulic conditions on the Cr removal efficiency. In this regard, the modelling work presented in this study can be considered to be complementary; since the impact of different operational conditions on the operation performance of the reactive material is set as one of the objectives of the modeling efforts demonstrated here.

### **3.2 Numerical Modeling Tool: Phreeq-C**

The hydrogeochemical model program called PHREEQC is used to simulate Cr(VI) removal by ZVI. Phreeqc is a computational software designed to simulate chemical reactions and the movement of substances in underground water systems. There are several programs that simulate reactive transport. Phreeqc's main benefit lies in its robust numerical solution technique and its utilization of comprehensive databases including thermodynamic data for elements, compounds, and reactions. This allows Phreeqc to accurately compute a wide range of parameters (Holch, 2008). The capabilities of Phreeq-C includes the followings: (Vizcek, 2016)

- Computation of the concentrations, activity, molalities, saturation indices, pH, and pE values of elements
- Simulating water mixing process
- Simulating the balance between solid and liquid phases
- Simulating the impact of temperature or pH variations
- Simulating the movement of mass through convection, as well as the spreading and mixing of substances through dispersion and diffusion.

The Phreeq-C input file is laid out using keywords. The resulting file in Phreeq-C provides the solution compositions, the saturation indices of the mineral phases together with pH, pE, activity, charge balance, ionic strength, and analysis error.

The limitations of the modeling tool Phreeq-C can be listed as follows: (Parkhurst, 1995).

- Phreeq-C only supports one dimensional (1D) flow conditions (Parkhurst, 1995).
- The results in Phreeq-C rely on thermodynamic data that embodied in the model (Parkhurst, 1995).
- The modeling tool assumes homogenous conditions for each cell in the transport model (Parkhurst, 1995).
- Phreeq-C in general is not built for complex and dynamic systems. The modeling tool can struggle to converge in case of non-linear reactions (Parkhurst, 1995).

It should be mentioned that these limitations actually shape the overall modeling work. How these limitations can impact its use for field scale applications are discussed under Section 4.

### **3.3 Conceptual Model**

As stated in Section 2.2.1.1, the Cr(VI) elimination with the help of ZVI may follow the steps given below (Gheju, 2010).

- Diffusion of  $\text{CrO}_4^{2-}$  from bulk solution to positively charged ZVI surface
- $\text{CrO}_4^{2-}$  adsorption onto ZVI surface
- $\text{CrO}_4^{2-}$  is reduced at the surface of ZVI and simple precipitates are formed i.e,  $\text{Cr}(\text{OH})_3$  or  $\text{Fe}(\text{OH})_3$
- Some reaction products are adsorbed/desorped from the surface
- Desorped products are transported to the bulk solution

According to the removal process explained by Gheju (2010), a schematic is created to illustrate the overall process. Figure 3.1 shows the conceptual model representing the removal mechanism incorporated in the reaction models for each column.

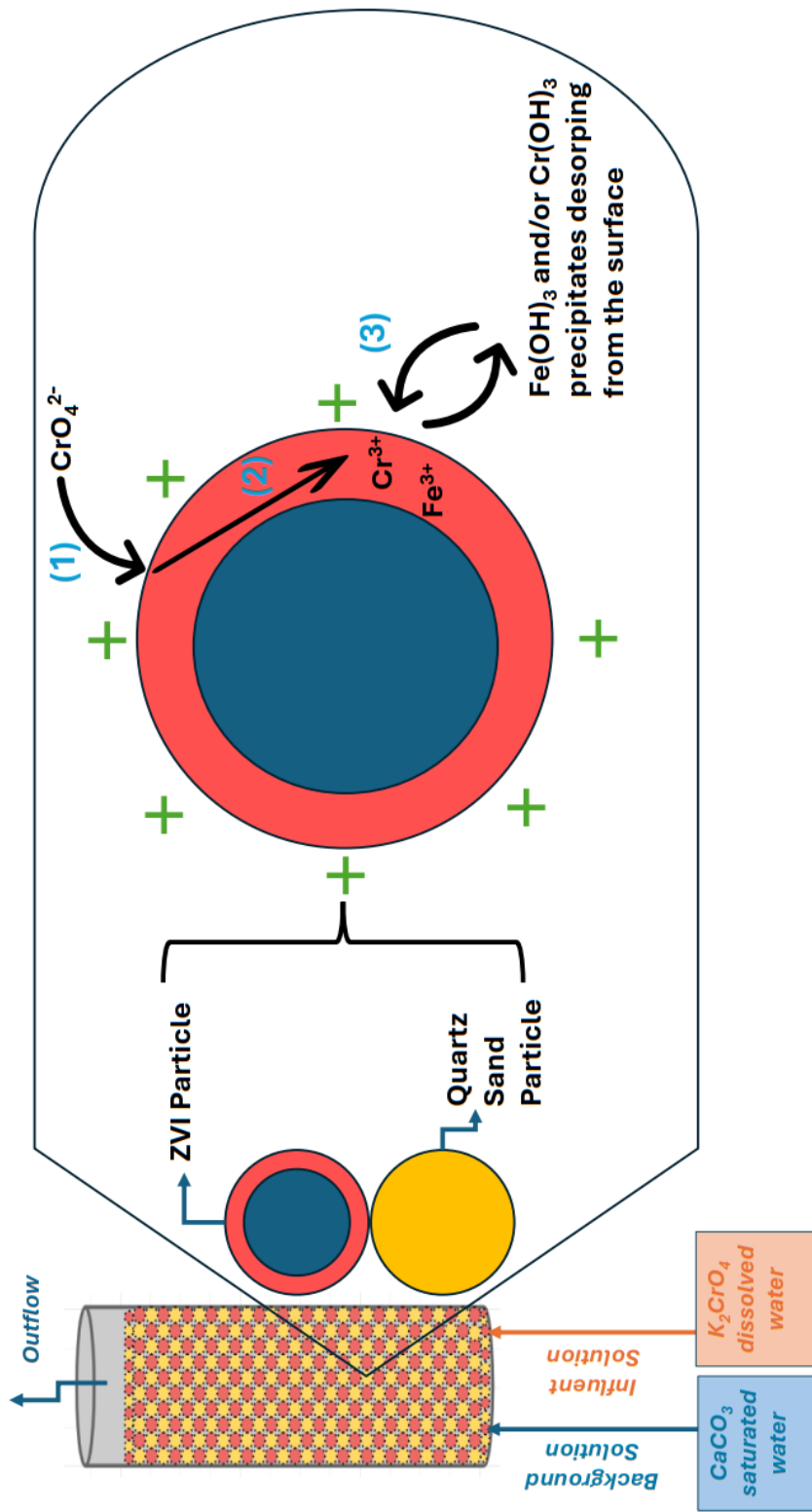


Figure 3.1 The illustration for the proposed Cr(VI) removal mechanism inside the column

### 3.3.1 Reaction Network Used in the Model

The geochemical processes included in this reaction network can be grouped into three categories: Aqueous speciation, mineral dissolution and precipitation, and Cr(VI) reduction reactions. Among these three processes, aqueous speciations and mineral precipitation-dissolutions are considered to be at equilibrium. Cr(VI) reduction process on the other hand is considered as a kinetically controlled process. The reactions involved in these processes, their corresponding rate constants and the governing equations representing each process are explained as follows.

#### 3.3.1.1 Aqueous Speciation

The aqueous speciation reactions are considered to be at equilibrium. The reactions are given in Table 3.2 together with the corresponding LogK values. The reactions are represented by using the following equation (Arora et al., 2014).

$$C_i = K_i^{-1} \gamma_i^{-1} \prod_{j=1}^{N_c} (\gamma_j C_j)^{v_{ij}} \quad (\text{Eqn 10})$$

where C is the concentration (mol/kgw), K is the thermodynamic equilibrium constant,  $\gamma$  is the activity coefficient,  $v_{ij}$  are the stoichiometric coefficients in the reaction,  $N_c$  is the number of primary and secondary species (Arora et al., 2014).

In the reaction network, there are 9 primary species and 30 aqueous complexes. The referred primary species are the following:  $K^+$ ,  $H^+$ ,  $CO_3^{2-}$ ,  $Ca^{2+}$ ,  $Na^+$ ,  $Cl^-$ ,  $Fe^{3+}$ ,  $Cr^{3+}$ ,  $Cr^{6+}$ . The aqueous speciation reactions and their equilibrium constants are given in Table 3.2 below.

Table 3.2 Aqueous speciation reactions used in the model simulation from *minteq.v4.dat*, (U.S. Environmental Protection Agency, 1998)

	Aqueous speciation reaction	LogK
1.	$2H_2O \leftrightarrow O_2 + 4H^+ + 4e^-$	-85.9951
2.	$2H^+ + 2e^- \leftrightarrow H_2$	-3.15
3.	$H_2O \leftrightarrow OH^- + H^+$	-13.997
4.	$Fe^{3+} + H_2O \leftrightarrow FeOH^{2+} + H^+$	-2.187
5.	$Fe^{3+} + 2H_2O \leftrightarrow Fe(OH)_2^+ + 2H^+$	-4.594
6.	$Fe^{3+} + 4H_2O \leftrightarrow Fe(OH)_4^- + 4H^+$	-12.56
7.	$2Fe^{3+} + 2H_2O \leftrightarrow Fe_2(OH)_2^{4+} + 2H^+$	-21.588
8.	$3Fe^{3+} + 4H_2O \leftrightarrow Fe_3(OH)_4^{5+} + 4H^+$	-2.854
9.	$Cr(OH)_2^+ + H^+ \leftrightarrow Cr(OH)^{2+} + H_2O$	5.9118
10.	$Cr(OH)_2^+ + H_2O \leftrightarrow Cr(OH)_3 + H^+$	-8.4222
11.	$Cr(OH)_2^+ + H_2O \leftrightarrow Cr(OH)_4^- + 2H^+$	-17.8192
12.	$Cr(OH)_2^+ \leftrightarrow CrO_2^- + 2H^+$	-17.7456
13.	$Ca^{2+} + H_2O \leftrightarrow CaOH^+ + H^+$	-12.697
14.	$Cr(OH)_2^+ + 2H^+ + Cl^- \leftrightarrow CrCl^{2+} + 2H_2O$	9.6808
15.	$Cr(OH)_2^+ + 2Cl^- + 2H^+ \leftrightarrow CrCl_2^+ + 2H_2O$	8.658
16.	$Cr(OH)_2^+ + 2Cl^- + H^+ \leftrightarrow CrOHCl_2 + H_2O$	2.9627
17.	$H^+ + CO_3^{2-} \leftrightarrow HCO_3^-$	10.329
18.	$2H^+ + CO_3^{2-} \leftrightarrow H_2CO_3$	16.681
19.	$Ca^{2+} + H^+ + CO_3^{2-} \leftrightarrow CaHCO_3^+$	11.599
20.	$CO_3^{2-} + Ca^{2+} \leftrightarrow CaCO_3$	3.2

**Table 3.2 (Continued)**

	<b>Aqueous speciation reaction</b>	<b>LogK</b>
21.	$Na^+ + CO_3^{2-} \leftrightarrow NaCO_3^-$	1.27
22.	$Na^+ + H^+ + CO_3^{2-} \leftrightarrow NaHCO_3$	10.079
23.	$CrO_4^{2-} + H^+ \leftrightarrow HCrO_4^-$	6.51
24.	$CrO_4^{2-} + 2H^+ \leftrightarrow H_2CrO_4$	6.4188
25.	$2CrO_4^{2-} + 2H^+ \leftrightarrow Cr_2O_7^{2-} + H_2O$	14.56
26.	$CrO_4^{2-} + Cl^- + 2H^+ \leftrightarrow CrO_3Cl^- + H_2O$	7.3086
27.	$CrO_4^{2-} + Na^+ \leftrightarrow NaCrO_4^-$	0.6963
28.	$K^+ + CrO_4^{2-} \leftrightarrow KCrO_4^-$	0.57
29.	$2K^+ + CrO_4^{2-} \leftrightarrow K_2CrO_4$	-0.5134
30.	$2K^+ + 2CrO_4^{2-} + 2H^+ \leftrightarrow K_2Cr_2O_7$	-17.2424

The initial conditions considered in the modelling runs rely on the experimental conditions, as conducted by (Uyuşur, 2006). As stated by Uyuşur (2006), the background solution in the experimental columns were saturated with  $CaCO_3$ , in order to replicate groundwater systems that contains carbonate. Therefore, the solubility of  $CaCO_3$  (s) in de-ionized water was exposed to  $P_{CO_2} = 10^{-3.5}$  atm. pH of the background solution was reported to be within range of 7.3 to 8.1 (Uyuşur, 2006). The influent solutions introduced to the columns were produced by dissolving potassium chromate salt ( $K_2CrO_4$ ) to the background solution. The inlet concentrations of Cr(VI) were 20 mg/l. The concentration of 20 mg/L was established based on the average levels of Cr(VI) found in plumes (Uyuşur, 2006). Based on these experimental conditions, the solution composition of the inflowing water to the columns is provided in Table 3.3.

Table 3.3 The influent solution composition

Influent Solution	
Constituents	Concentration
Cr(VI)	20 mg/L
K <sup>+</sup>	40 mg/L

### 3.3.1.2 Mineral Dissolution and Precipitation

The mineral dissolution and precipitation reactions are considered to be in equilibrium. The reactions are given in Table 3.4 together with the corresponding LogK value. As shown in Table 3.4, the minerals included in the reaction network are aragonite (CaCO<sub>3</sub>), calcite (CaCO<sub>3</sub>), ferrihydrite (Fe(OH)<sub>3</sub>), goethite (FeO(OH)) and hematite (Fe<sub>2</sub>O<sub>3</sub>). Based on the inlet calcite (CaCO<sub>3</sub>) saturation of background solutions as stated in the experimental methods, the background solution compositions in the model runs were saturated with calcite. The rest of the mineral phases were initially absent and were allowed to form as secondary minerals throughout the process. The reaction rate constants (LogK) are represented by using the following equation (Arora et al., 2014).

$$K_m = \prod_{j=1}^{N_c} (\gamma_j C_j)^{v_{mj}}$$

(Eqn 11)

where  $K_m$  is the equilibrium constant for the mineral,  $N_c$  is the number of primary species,  $v_{mj}$  are the stoichiometric coefficients of primary species  $j$  in mineral  $m$ . It should be mentioned that subscript  $m$  refers to minerals (Arora et al., 2014).

Table 3.4 Secondary mineral reactions taken into account in the model simulation and the rate constants correlating with these reactions from *minteq.v4.dat*, (U.S. Environmental Protection Agency, 1998)

Mineral	Secondary Mineral Reactions	LogK
Aragonite	$CaCO_3 + H^+ = Ca^{2+} + HCO_3^-$	-8.3
Calcite	$CaCO_3 + H^+ = Ca^{2+} + HCO_3^-$	-8.48
Ferrihydrite	$Fe(OH)_3 + 3H^+ = Fe^{3+} + 3H_2O$	3.191
Goethite	$FeO(OH) + 3H^+ = Fe^{3+} + 2H_2O$	0.491
Hematite	$Fe_2O_3 + 6H^+ = 2Fe^{3+} + 3H_2O$	6.386
Chromium Hydroxide	$Cr(OH)_3 + H^+ = Cr(OH)_2^+ + H_2O$	1.3355

### 3.3.1.3 Cr(VI) Reduction

Cr(VI) reduction with ZVI in the model simulations is described with a mixed-order reaction rate as given in Table 3.5 below. This equation is actually a combination of first order reaction rate expression and equations for reactive surface area update of ZVI. The reactive surface area of the ZVI is updated due to the Fe(0) depletion with corrosion and due to the effect of passivation with secondary mineral precipitation as explained below.

The reactive surface area of iron in the kinetic expressions is adjusted with an a two-third power relationship as follows. The mentioned relationship is only due to iron depletion with corrosion (Jeen et al., 2007; Mayer et al., 2001).

$$S_{Fe^0} = S_{Fe^0}^0 \times \left( \frac{\varphi_{Fe^0}}{\varphi_{Fe^0}^0} \right)^{2/3} \quad (\text{Eqn 12})$$

where,  $S_{Fe0}$  and  $S_{Fe0}^0$  are the current and initial reactive surface area of the ZVI,  $\varphi_{Fe0}$  and  $\varphi_{Fe0}^0$  are the current and initial amount of the ZVI (Jeen et al., 2007; Mayer et al., 2001).

The changing iron reactivity resulting from mineral accumulation can be estimated using an empirically established correlation between reactivity and secondary mineral deposition, as expressed in the equation below (Jeen et al., 2007).

$$S(x, t) = S_0 \times \exp\left(-\sum_i \alpha_i \varphi_i(x, t)\right) \quad (\text{Eqn 13})$$

where,  $S(x,t)$  and  $S_0$  are the current and initial reactive surface area of the ZVI,  $\alpha_i$  is the proportionality constant of the mineral phase  $i$ ,  $\varphi_i(x,t)$  is the amount of the mineral  $i$ ,  $x$  and  $t$  represents location and time respectively (Jeen et al., 2007).

Therefore, the surface area updates corresponding to these processes are represented by the Eqn 12 and Eqn 13 are integrated to the rate expression as seen in Table 3.5 below.

Table 3.5 Kinetically controlled Cr(VI) reduction reaction used in the model simulation together with rate expression

<b>Corrosion Reaction</b>
$Fe^0 + 8H^+ + CrO_4^{2-} = Fe^{3+} + Cr^{3+} + 4H_2O$
<b>Rate Expression</b>
$R_{Cr(VI)} = -k_{SA-Cr(VI)-Fe^0} \times S \times C_{Cr(VI)} \times \left(\frac{\varphi_{Fe^0}}{\varphi_{Fe^0}^0}\right)^{2/3} \times \exp\left(-\sum_i \alpha_i \varphi_i(x, t)\right)$
where, $k_{SA-Cr(VI)-Fe^0}$ is the rate constant (L/m <sup>2</sup> .sec) normalized to Fe surface area $S$ (m <sup>2</sup> Fe / L), $C_{Cr(VI)}$ is the Cr(VI) concentration (mol/L), $\varphi_{Fe0}$ and $\varphi_{Fe0}^0$ are the current and initial moles of the ZVI, $\alpha_i$ is the proportionality constant of the mineral phase $i$ , $\varphi_i(x,t)$ is the amount of the mineral $i$ , $x$ and $t$ represents location and time respectively.

### 3.3.2 Transport Process

One dimensional (1D) diffusive, dispersive and advective transport is taking place within the columns. The model simulations are therefore based on the 1D reactive transport processes to represent the column experiments carried out by the experimental studies. The governing general equation for the transport process is as follows (Steefel et al., 2014).

$$\frac{\partial(\phi C_i)}{\partial t} = \nabla \cdot (\phi D \nabla C_i) - \nabla \cdot (q \cdot C_i) - \sum_{r=1}^{N_r} v_{ir} R_r$$

(Eqn 14)

where,  $\phi$  is the porosity ( $\text{m}^3$  of void /  $\text{m}^3$  of medium),  $C_i$  is the concentration,  $\nabla$  is the divergence operator,  $D$  is the hydrodynamic dispersion coefficient ( $\text{m}^2/\text{s}$ ),  $q$  is the Darcy flux ( $\text{m}^3$  of  $\text{H}_2\text{O}$  /  $\text{m}^2 \cdot \text{s}$ ),  $v_{ir}$  is the stchiometric coefficient for the reactive phase,  $R_r$  is the reaction term (Steefel et al., 2014)

In Phreeq-C, the 1D columns are defined by a series of cells and each of these cells have the same pore volume. Lengths are specified for each cell, and the time step indicates the duration required for a pore volume of water to travel across each cell. The velocity of water in each cell is calculated by dividing the length of the cell by the time step (Parkhurst & Apello, 2013).

The columns used in the experiments were 15 cm in length. The 1D numerical model of reactive transport is defined with a uniform grid discretization of 0.1 cm, where each column is divided into 150 cells. The grid system of the columns are shown by Figure 3.2 below. The transport related parameters for the columns are given in Table 3.6 below.

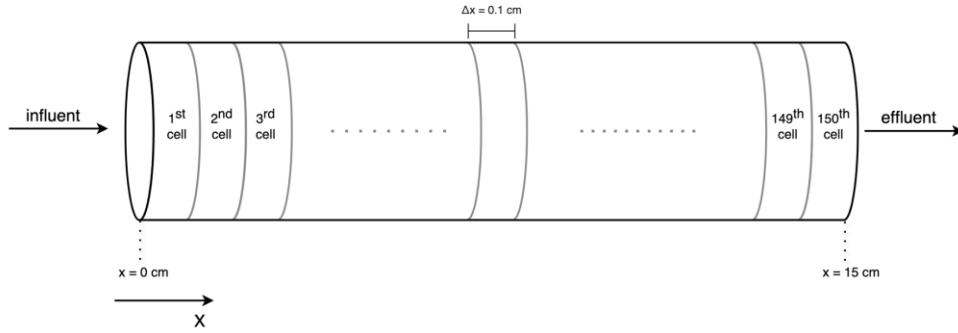


Figure 3.2 Grid System of the Simulated Columns

In order to control numerical dispersion, the grid spacing and the size of a time step can be determined by applying the Peclet and Courant criteria. The Peclet Criterion (Pe) controls the spatial discretization with respect to porewater velocity and dispersivity on a cell basis. Courant Criterion (Co) controls the temporal discretization with respect to porewater velocity and spatial discretization (Socolofsky & Jirka, 2001). The referred criterias are shown by the following equations.

$$Pe = \frac{v_x \Delta x}{D_{xx}} < 2 \quad (\text{Eqn 15})$$

$$Co = \frac{v_x \Delta t}{\Delta x} \leq 1 \quad (\text{Eqn 16})$$

where,  $v_x$  is the contaminant velocity,  $D_{xx}$  is the dispersion coefficient, and  $\Delta t$  and  $\Delta x$  are the size of the time step and the grid size in x-direction, respectively (Socolofsky & Jirka, 2001).

The referred Pe and Co values are calculated for each column used in the modelling runs and are shown in Table 3.6; which are consistent with the referred criteria.

Table 3.6 Transport related input data used in the model simulations

<b>Parameters</b>	<b>10IR Column</b>		<b>25IR Column</b>		<b>50IR Column</b>
Flux (mL/cm <sup>2</sup> .min)	0.07	0.127	0.07	0.127	0.127
Flow velocity (cm/day)	196.13	361.51	269.16	345.60	260.19
Inlet Cr(VI) Concentration (mg/L)	20	20	20	20	20
Initial ZVI Amount (moles)	0.267		0.124		0.0429
Porosity	0.486		0.524		0.628
Grid Size $\Delta x$ (cm)	0.1	0.1	0.1	0.1	0.1
Time Step $\Delta t$ (sec)	44.1	23.9	32.1	25.0	33.2
Simulation Length (days)	16	6	20	17	24
Dispersivity (m)	0.1159	0.001067	0.02508	0.01143	0.05241
Diffusion Coefficient at 298.15 K in water (for Cr <sup>3+</sup> ) (m <sup>2</sup> /s)	0.595 $\times 10^{-9}$	0.595 $\times 10^{-9}$	0.595 $\times 10^{-9}$	0.595 $\times 10^{-9}$	0.595 $\times 10^{-9}$

**Table 3.6 (Continued)**

<b>Parameters</b>	<b>10IR Column</b>	<b>25IR Column</b>	<b>50IR Column</b>	<b>Parameters</b>	<b>10IR Column</b>
Peclet Number (Pe)	0.0086	0.94	0.040	0.087	0.019
Courant Number (Co)	1.00	1.00	1.00	1.00	1.00

## CHAPTER 4

### RESULTS AND DISCUSSIONS

The reaction network and transport processes that have been used to build the reactive transport models were detailed under Section 3.3. In this section, simulation results of Cr(VI) reduction with ZVI reactive media is presented for varying ZVI concentrations and flowrate conditions, based on the experiments of Uyuşur (2006) and Uyuşur and Ünlü (2009). The impact of the ZVI reactive surface area modification, based on the depletion of Fe(0) and secondary mineral precipitation, on the Cr(VI) removal efficiency is discussed. Then the sensitivity of key input parameters to the models are presented and discussed in the sensitivity analysis section. Lastly, model predictions of Cr(VI) reduction by ZVI under varying inlet Cr(VI) concentrations are demonstrated.

#### 4.1 Non-reactive Transport Simulation

In the modelling study, first nonreactive transport simulation of tracer through a control test column containing only quartz sand was conducted, in order to examine the impact of only transport in the absence of reactions. Chloride ( $\text{Cl}^-$ ) was introduced into the sand column as a conservative tracer. As explained under Section 3.3, the transport through the columns follows one dimensional (1D) diffusive, dispersive and advective transport.

Comparison of the model simulation results with the experimentally measured data for  $\text{Cl}^-$  concentrations is given by Figure 4.1.

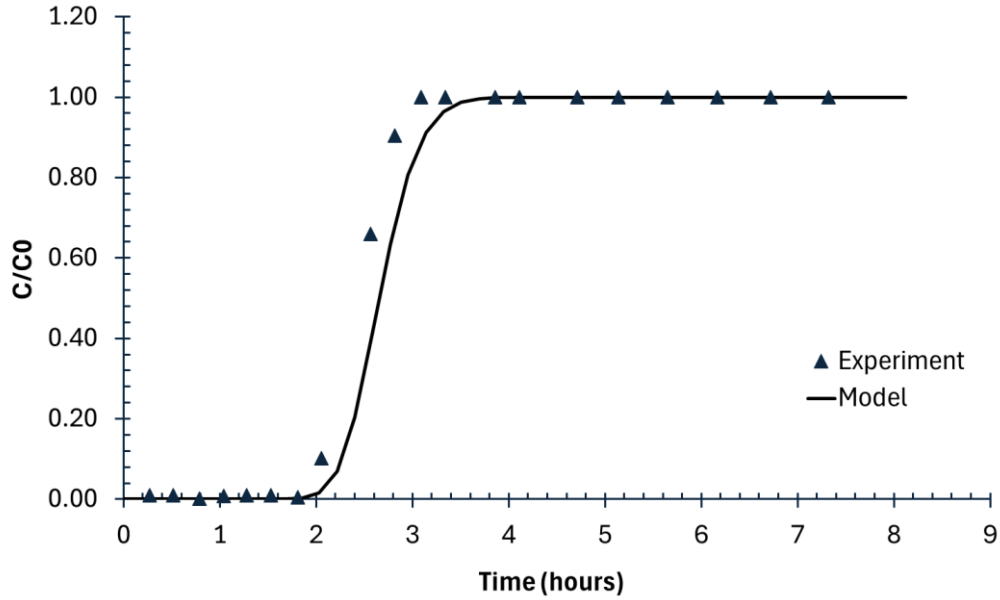


Figure 4.1 Comparison of model and experimental  $\text{Cl}^-$  concentrations for the tracer column test

To assess the quality of fit between experimental and model data two statistical parameters are used:  $R^2$ , Coefficient of determination and MSE, Mean Square Error.  $R^2$  and MSE values are calculated as follows (Walpole & Myers, 1989).

$$R^2 = 1 - \left\{ \frac{\sum(X - Y)^2}{[\sum X^2] - \frac{[\sum X]^2}{NOB}} \right\} \quad (\text{Eqn 17})$$

$$MSE = \left\{ \sqrt{\frac{1}{NOB} \cdot \left( \sum (X - Y)^2 \right)} \right\} \quad (\text{Eqn 18})$$

where, X and Y are experimental and modeled data, respectively. NOB is number of experimental data points.

The results of statistical error analysis for the non-reactive transport simulation are provided in Table 4.1 below.

Table 4.1 The  $R^2$  and MSE values between experimental and model data of control column experiment

	$R^2$	MSE
Experimental and Model Data for $Cl^-$	0.9740	0.0072

According to Profillidis (2019), an  $R^2$  value between 0.8 and 1 corresponds to a strong positive correlation between the two data. It is stated that a perfect model, i.e., a model data perfectly fitting to experimental data, would produce zero errors, where RMSE would equal 0.0 (Profillidis, 2019). As shown by Table 4.1, for  $Cl^-$  predictions, the 0.9740  $R^2$  value and the MSE value being close to zero indicates a strong correlation between the model and experimental data.

## 4.2 Reactive Transport Simulations

The reactive transport simulations are conducted using a reaction network that is developed to incorporate the decrease in ZVI reactive surface area due to the depletion of Fe(0), as well as surface passivation due to secondary mineral precipitation (Table 3.5). This has been accomplished by initially testing various reaction kinetics and gradually incorporating the terms for Fe(0) depletion and secondary mineral precipitation. At first step, reactive surface area update only due to Fe(0) depletion (Eqn 12) is added to the rate expression. In the second step, secondary mineral precipitation effect (Eqn 13) is incorporated to the rate expression. At each step, the model has been calibrated with the reaction rate constants and kinetic parameters pertaining to the ZVI reactive surface area.. The

model simulation results have then been compared with the experimental results to see the quality of model fits, where the fit quality of the models has been measured with  $R^2$  and MSE values. The calibrated models using the two reaction kinetic approaches, together with the experimental results are given in Figure 4.2 for the 10IR Column experiment with  $0.07 \text{ mL/cm}^2 \cdot \text{min}$  flux, for demonstration purposes. The fit quality between the model and the experimental data for the two model simulations is measured with  $R^2$  and MSE values which are presented in Table 4.2 below.

As can be seen from Figure 4.2 as well as calculated  $R^2$  and MSE values for the first step as given in Table 4.2, with the defined rate expression for the first step, the model results could not entirely capture the experimental data (see black lines in Figure 4.2).

As explained in Section 3.3.1.3, the equation for the reactive surface area update (Eqn 12) reported by Mayer et al. (2001) does not consider the surface area update of the iron due to mineral precipitation. The referred reactive surface area update is only for the reactivity decrease due to Fe(0) depletion. However, as pointed out by various previous studies on ZVI based treatment, mineral precipitation, particularly carbonate minerals contribute to the decrease in the reactivity of iron (Blowes et al., 1997; Wanner et al., 2011; Kaplan & Gilmore, 2004). With the integration of secondary mineral precipitation effect into the rate expression by means of the exponential function (Eqn 13) presented by Jeon et al. (2007), a reasonably well match with the experimental data is accomplished (see blue lines in Figure 4.2). According to our simulation results,  $\text{CaCO}_3$  mineral precipitates during Cr(VI) reduction through the column. In this regard, the model is calibrated for the rate constant  $k$  and the proportionality constant of mineral  $\text{CaCO}_3$  precipitation, as seen in Table 3.5. Therefore, the model results imply that the effect of secondary mineral precipitation would need to be involved in rate expressions to model Cr(VI) reduction with ZVI.

Table 4.2 Calibrated kinetic parameters,  $R^2$  and MSE values for experimental and model data fit considering reaction kinetics with only Fe(0) depletion (Step 1) and also with surface passivation due to secondary mineral precipitation (Step 2)

Column ID	Rate Constant, k	Rate expression term involvement	Mineral Proportional-ity Constant, $\alpha$	$R^2$	MSE
10IR - 0.07 mL/cm <sup>2</sup> .min	$1.44 \times 10^{-4}$ (L/m <sup>2</sup> .sec)	Depletion of Fe(0) only (Eqn 12) (Step 1)	-	0.6904	0.079
10IR - 0.07 mL/cm <sup>2</sup> .min	$7.30 \times 10^{-5}$ (L/m <sup>2</sup> .sec)	Depletion of Fe(0) (Eqn 12) and surface passivation due to secondary mineral precipitation (Eqn 13) (Step 2)	200	0.9826	0.0027

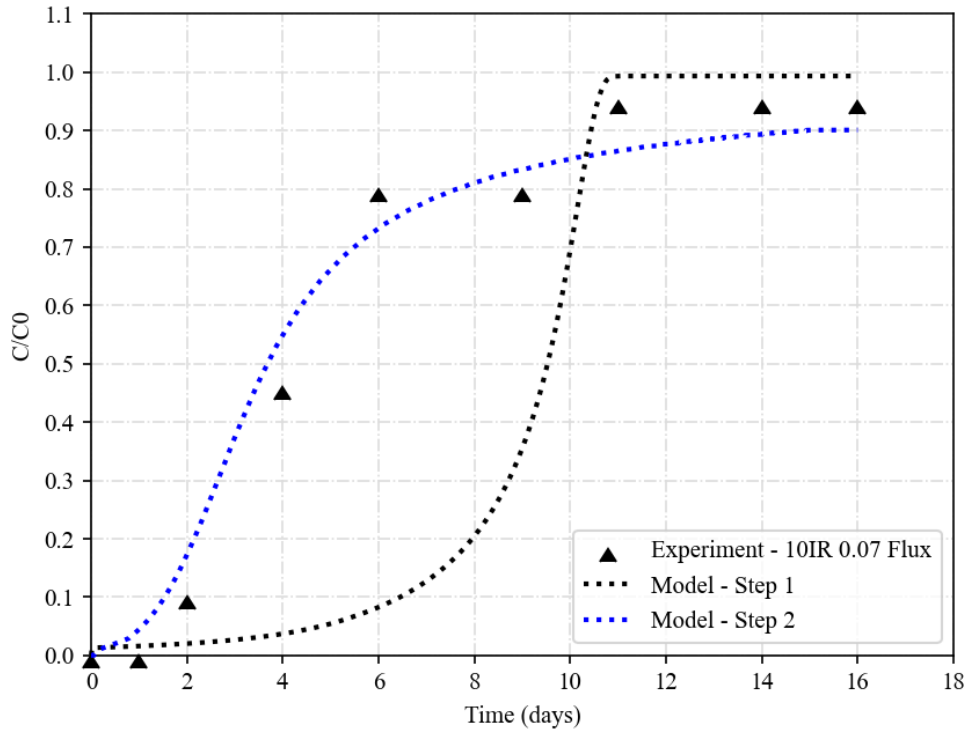


Figure 4.2 Comparative simulation results of the kinetic approaches with (blue lines) and without (black lines) the incorporation of secondary mineral formation terms with the experimental results (black symbols) for 10IR column with 0.07 mL/cm<sup>2</sup>.min flux

The simulations of the rest of the column experiments throughout this study has been carried out by considering the approach where both the effects of Fe(0) depletion and surface passivation due to secondary mineral precipitation are integrated into the kinetic rate expression for Cr removal by ZVI (as seen in Table 3.5). In the proceeding sections, the simulation results with calibrated parameters are presented for each column. Simulation results of the experiments are compared and the results are discussed.

#### 4.2.1 Simulation results of Cr(VI) removal with ZVI for varying Fe(0) concentrations and flowrate conditions

Reactive transport simulations of Cr(VI) removal by ZVI are conducted for the column experiments carried out by Uyuşur (2006); Uyuşur and Ünlü (2009); considering varying groundwater fluxes (0.07 and 0.127 mL/cm<sup>2</sup>.min) and ZVI concentrations (10%, 25% and 50% iron powder – corresponding to 10IR, 25IR and 50IR columns, respectively).

The model and the experimental results for the effluent Cr(VI) concentration with respect to inlet Cr(VI) concentration i.e., C/C<sub>0</sub>, versus time (days) for 10IR and 25IR Columns with 0.07 mL/cm<sup>2</sup>.min flux is given in Figure 4.3. The model and the experimental results of the 10IR, 25IR and 50IR Columns with 0.127 mL/cm<sup>2</sup>.min flux is given in Figure 4.4.

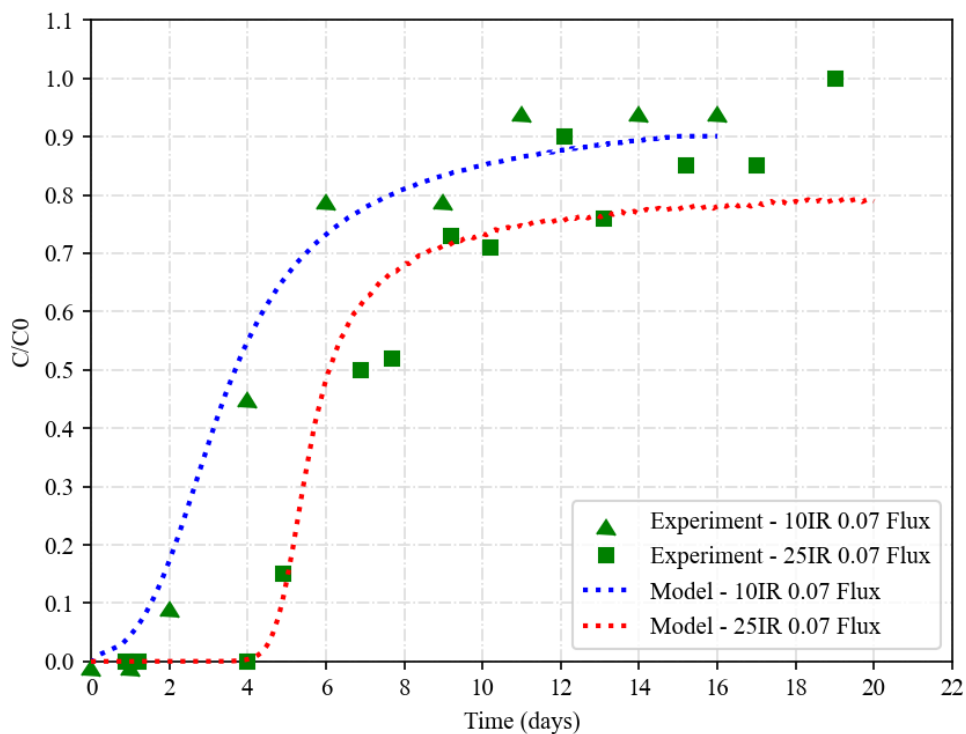


Figure 4.3 Experimental and modelling simulation results of the 10IR and 25IR Columns with 0.07 mL/cm<sup>2</sup>.min flux

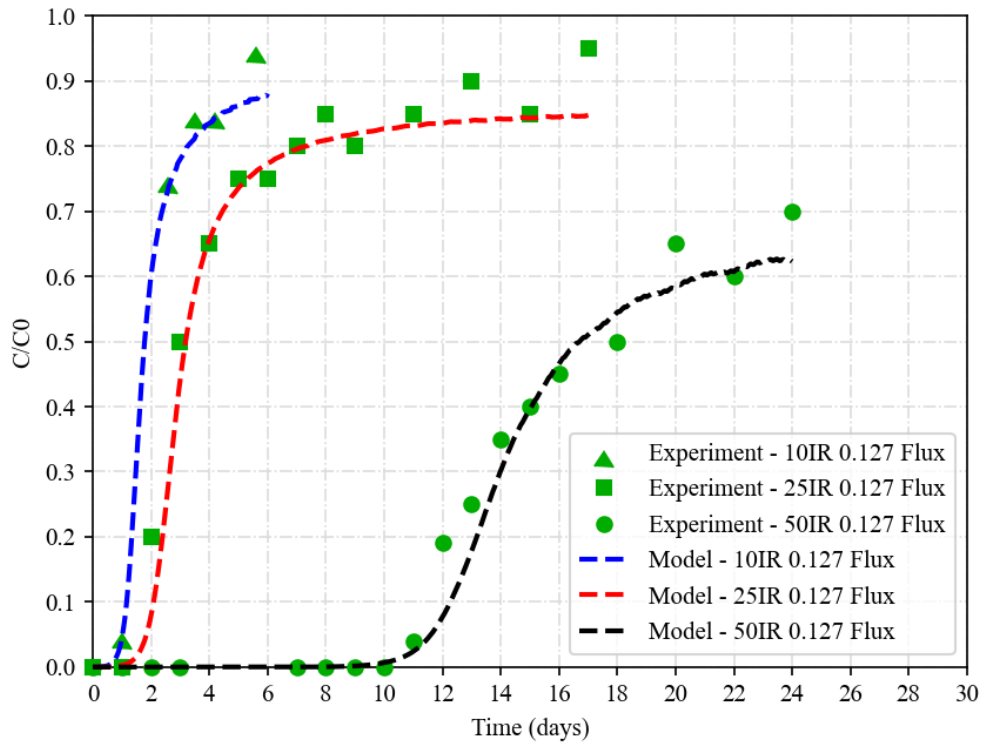


Figure 4.4 Experimental and modelling simulation results of the 10IR, 25IR and 50IR Columns with 0.127 mL/cm<sup>2</sup>.min flux

The calibrated model parameters for the 10IR and 25IR Columns with 0.07 mL/cm<sup>2</sup>.min flux are summarized in Table 4.3 below.

Table 4.3 Calibrated model parameters for 10IR and 25IR Columns with 0.07 mL/cm<sup>2</sup>.min flux

Input Parameter	10IR 0.07 mL/cm <sup>2</sup> .min Flux	25IR 0.07 mL/cm <sup>2</sup> .min Flux
Initial ZVI Amount (moles)	0.0429	0.124
Rate Constant, k (L/m <sup>2</sup> .sec)	$7.30 \times 10^{-5}$	$2.11 \times 10^{-4}$
Proportionality Constant for CaCO <sub>3</sub> Mineral, $\alpha$	200	300

**Table 4.3 Cont'd**

<b>Input Parameter</b>	<b>10IR 0.07 mL/cm<sup>2</sup>.min Flux</b>	<b>25IR 0.07 mL/cm<sup>2</sup>.min Flux</b>
Proportionality Constant for Hematite Mineral, $\alpha_{\text{Fe}_2\text{O}_3}$	-	300
Proportionality Constant for Chromium Hydroxide Mineral, $\alpha_{\text{Cr}(\text{OH})_3}$	-	500

The calibrated model parameters for the 10IR, 25IR and 25IR Columns with 0.127 mL/cm<sup>2</sup>.min flux are summarized in Table 4.4 below.

Table 4.4 Calibrated model parameters for the 10IR, 25IR and 50IR Columns with flux of 0.127 mL/cm<sup>2</sup>.min

<b>Input Parameter</b>	<b>10IR 0.127 mL/cm<sup>2</sup>.min Flux</b>	<b>25IR 0.127 mL/cm<sup>2</sup>.min Flux</b>	<b>50IR 0.127 mL/cm<sup>2</sup>.min Flux</b>
Initial ZVI Amount (moles)	0.0429	0.124	0.267
Rate Constant, k (L/m <sup>2</sup> .sec)	$2.12 \times 10^{-5}$	$6.30 \times 10^{-5}$	$5.38 \times 10^{-5}$
Proportionality Constant for CaCO <sub>3</sub> Mineral, $\alpha$	450	300	100
Proportionality Constant for Hematite Mineral, $\alpha_{\text{Fe}_2\text{O}_3}$	-	300	100
Proportionality Constant for Chromium Hydroxide Mineral, $\alpha_{\text{Cr}(\text{OH})_3}$	-	500	300

Figure 4.3 shows that, 10IR Column with  $0.07 \text{ mL/cm}^2\cdot\text{min}$  flux starts to be exhausted within the 1<sup>st</sup> day of the experiment. By the 3<sup>rd</sup> to 4<sup>th</sup> day of the experiment,  $C/C_0$  reaches 50% which means almost half of the influent Cr(VI) concentration i.e., 10 mg/L, is measured at the effluent. By the 15<sup>th</sup> day of the experiment, the column reaches exhaustion and almost no treatment occurs afterward. For the  $0.127 \text{ mL/cm}^2\cdot\text{min}$  flux, the column starts to be exhausted within 1<sup>st</sup> day of the experiment. Within the 2<sup>nd</sup> day of the experiment,  $C/C_0$  reaches 55%. And by the 6<sup>th</sup> day of the experiment, the column reaches complete exhaustion and almost no reduction occurs afterwards.

As Figure 4.3 shows that the  $C/C_0$  profiles migrate rapidly at earlier times after first detection. For the 10IR Column with  $0.07 \text{ mL/cm}^2\cdot\text{min}$  flux, within almost 7 days,  $C/C_0$  increases by 80%. After the 7<sup>th</sup> day to the 16<sup>th</sup> day of the simulation,  $C/C_0$  only increases by 10%. This indicates that the increase in  $C/C_0$  at later times is not as rapid as it is at the early times and ZVI maintains some reactivity even after secondary minerals decrease this reactivity quickly at early times. Similarly for the 25IR column behaviors, the  $C/C_0$  profiles also migrate rapidly at earlier times after first detection. For instance, with  $0.07 \text{ mL/cm}^2\cdot\text{min}$  flux, from the 4<sup>th</sup> day to almost 7<sup>th</sup> day,  $C/C_0$  increases to almost 65%. And from the 7<sup>th</sup> day to 20<sup>th</sup> day, for almost 13 day,  $C/C_0$  increases only 19%. This indicates that  $C/C_0$  profile at later times do not migrate as rapidly as the early times and ZVI maintain some reactivity even after secondary minerals decrease this reactivity quickly at early times. The progressive passivation of ZVI can be observed with 50IR Column as well. From the 10<sup>th</sup> day to the 20<sup>th</sup> day of the simulation,  $C/C_0$  increases by 60%. Afterward, the graph indicates that the increase in  $C/C_0$  is rather slower than it is at earlier times. This progressive passivation of ZVI and maintenance of reactivity was also observed in Jeen et al.'s (2007) study on TCE treatment with ZVI.

Figure 4.3 shows that in 25IR Column with  $0.07 \text{ mL/cm}^2\cdot\text{min}$  flux, on the 4<sup>th</sup> day of the simulation, the column starts to be exhausted. By the 6<sup>th</sup> day of the simulation,  $C/C_0$  reaches 50% which means half of the influent Cr(VI) concentration i.e., 10 mg/L, is measured at the effluent. By the almost 19<sup>th</sup> day of the experiment,  $C/C_0$

reaches up to 100% according to experimental data which means that the column is completely exhausted and from that time on no treatment will occur and influent Cr(VI) concentration will be measured at the effluent. Compared to 25IR Column with 0.07 mL/cm<sup>2</sup>.min flux, Figure 4.4 shows that with a higher flux of 0.127 mL/cm<sup>2</sup>.min, the column started to be exhausted on almost 1<sup>st</sup> day of the simulation. By the 3<sup>rd</sup> day of the simulation, C/C<sub>0</sub> reaches to 50%, and by the 17<sup>th</sup> day of the simulation, the column is almost completely exhausted.

Figure 4.4 shows that the 50IR Column with 0.127 mL/cm<sup>2</sup>.min flux starts to be exhausted after 10<sup>th</sup> day of the simulation. By the 17<sup>th</sup> day of the simulation, C/C<sub>0</sub> reaches to 50% and by the 24<sup>th</sup> day C/C<sub>0</sub> value reaches to almost 70%. 50IR Column has the highest ZVI i.e., reactive media, among the columns, where for 10 days no Cr(VI) is measured at the effluent which means for 10 days Cr(VI) is remediated. When the performance of all 3 columns are compared, it is seen that the 50IR Column provides the best remediation activity among the columns, as also reported by Uyuşur (2006); Uyuşur and Ünlü (2009).

The reaction rate constants and the proportionality constants,  $\alpha$  for the secondary mineral precipitates are estimated by calibration for all column experiments. The estimated values are given in Table 4.5. It can be concluded that the simulation results are consistent with the experimental results. The fit quality between the model and the experimental data is measured with R<sup>2</sup> and MSE and the values are also presented for all column simulations in Table 4.5 below, indicating a very good agreement between measured and predicted concentration values, and hence reasonably well calibration of the numerical reactive transport models.

Table 4.5 R<sup>2</sup> and MSE values along with other model parameters for 10IR, 25IR and 50IR Columns with 0.07 and 127 mL/cm<sup>2</sup>.min fluxes

Column ID	Rate Constant, k (L/m <sup>2</sup> .s)	Proportionality Constant for CaCO <sub>3</sub> Mineral, $\alpha_{CaCO3}$	Proportionality Constant for Fe <sub>2</sub> O <sub>3</sub> Mineral, $\alpha_{Fe2O3}$	Proportionality Constant for Cr(OH) <sub>3</sub> Mineral, $\alpha_{Cr(OH)3}$	R <sup>2</sup>	MSE
10IR 0.07 mL/cm <sup>2</sup> .min Flux	$7.30 \times 10^{-5}$	200	-	-	0.975	0.005
10IR 0.127 mL/cm <sup>2</sup> .min Flux	$2.12 \times 10^{-5}$	450	-	-	0.986	0.005
25IR 0.07 mL/cm <sup>2</sup> .min Flux	$2.11 \times 10^{-4}$	300	300	500	0.937	0.009
25IR 0.127 mL/cm <sup>2</sup> .min Flux	$6.30 \times 10^{-5}$	300	300	500	0.979	0.003
50IR 0.127 mL/cm <sup>2</sup> .min Flux	$5.38 \times 10^{-5}$	100	100	200	0.981	0.001

#### 4.2.2 Impact of Secondary Mineral Formation

As stated above, in 10IR Columns the only mineral contributed to the ZVI reactivity decrease was  $\text{CaCO}_3$ . Compared to 10IR Columns, 25IR and 50IR Columns have a higher amount of ZVI. To match the experimental results, in addition to  $\text{CaCO}_3$ ,  $\text{Fe}_2\text{O}_3$  and  $\text{Cr}(\text{OH})_3$  mineral precipitation have also been incorporated into the rate expression and their proportionality constants are determined by calibration (see Table 4.4 and Table 4.5). Gui et al. (2009), Pratt et al (1997) and Wanner et al. (2011) also report the presence of these two minerals ( $\text{Fe}_2\text{O}_3$  and  $\text{Cr}(\text{OH})_3$ ) as a surface coat to ZVI.

Table 4.5 shows the rate constant,  $k$  for the 10IR Column with  $0.07 \text{ mL/cm}^2\cdot\text{min}$  flux is 3 times higher than that of the 10IR Column with  $0.127 \text{ mL/cm}^2\cdot\text{min}$  flux. Similarly for the 25IR column, the rate constant,  $k$  value for the column with  $0.07 \text{ mL/cm}^2\cdot\text{min}$  was 3 times higher than the  $0.127 \text{ mL/cm}^2\cdot\text{min}$  flux column. The proportionality constant,  $\alpha$  associated with  $\text{CaCO}_3$  mineral for the 10IR Column with  $0.127 \text{ mL/cm}^2\cdot\text{min}$  is higher compared to that of the 10IR Column with  $0.07 \text{ mL/cm}^2\cdot\text{min}$  flux. According to Jeon et al. (2007) and Gui et al. (2009), a higher value of the proportionality constant,  $\alpha$  means that the contribution to reactivity loss is higher. For the 25IR columns, the proportionality constants,  $\alpha$  for the three minerals were the same for both  $0.07$  and  $0.127 \text{ mL/cm}^2\cdot\text{min}$  fluxes, where the proportionality constant for  $\text{Cr}(\text{OH})_3$  was higher compared to  $\text{CaCO}_3$  and  $\text{Fe}_2\text{O}_3$ . Therefore,  $\text{CaCO}_3$  and  $\text{Fe}_2\text{O}_3$  were observed to have equal effects on Fe(0) surface passivation for 25IR columns, whereas  $\text{Cr}(\text{OH})_3$  had a higher impact. For the 50IR Column with  $0.127 \text{ mL/cm}^2\cdot\text{min}$  flux, the  $\text{Cr}(\text{OH})_3$  mineral had a higher proportionality constant compared to other minerals, again indicating the higher impact of  $\text{Cr}(\text{OH})_3$  precipitation in reducing the ZVI surface reactivity. When the calibrated proportionality constants for the three minerals are compared among 10IR, 25IR and 50IR columns, the results show that the impact of ZVI surface passivation is reduced with increasing ZVI concentrations. Due to the higher amount of available

Fe(0) surface with higher ZVI, the impact of secondary mineral precipitation becomes less pronounced.

The concentration changes of the referred minerals with respect to time and distance are provided below. Figure 4.5 shows the  $\text{CaCO}_3$  concentration (mol/kgw) versus time behaviour for 10IR, 25IR and 50IR Columns with 0.07 and 0.127  $\text{mL/cm}^2\cdot\text{min}$  fluxes.

The distribution of  $\text{CaCO}_3$ ,  $\text{Fe}_2\text{O}_3$ , and  $\text{Cr}(\text{OH})_3$  minerals along the columns for 0.127  $\text{mL/cm}^2\cdot\text{min}$  fluxes are shown between Figure 4.8-Figure 4.14.

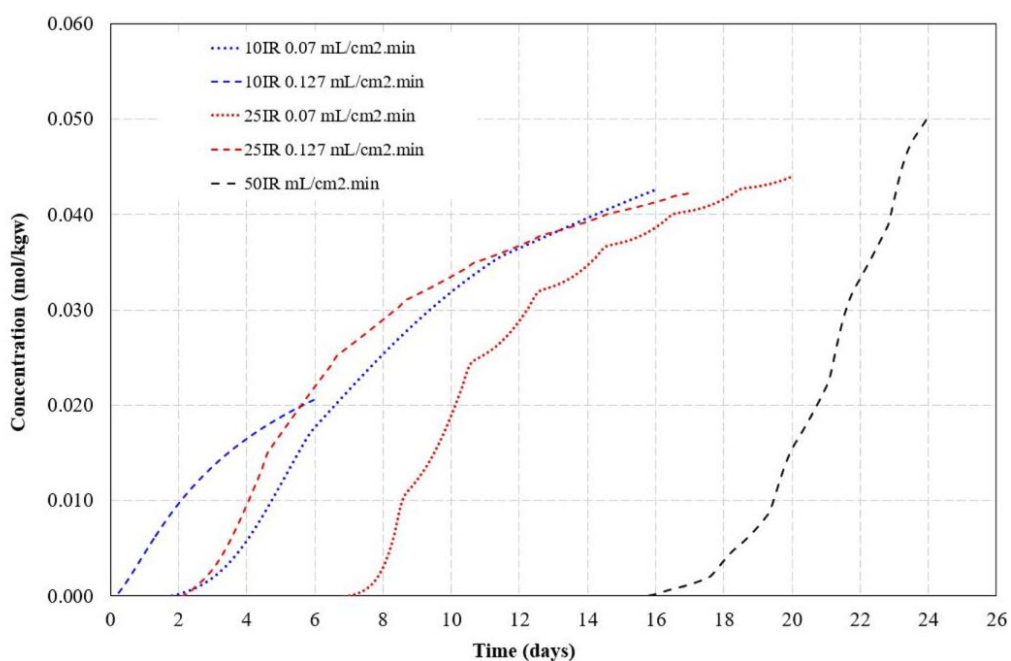


Figure 4.5  $\text{CaCO}_3$  concentration (mol/kgw) versus time for 10IR, 25IR and 50IR Columns with 0.07 and 0.127  $\text{mL/cm}^2\cdot\text{min}$  fluxes

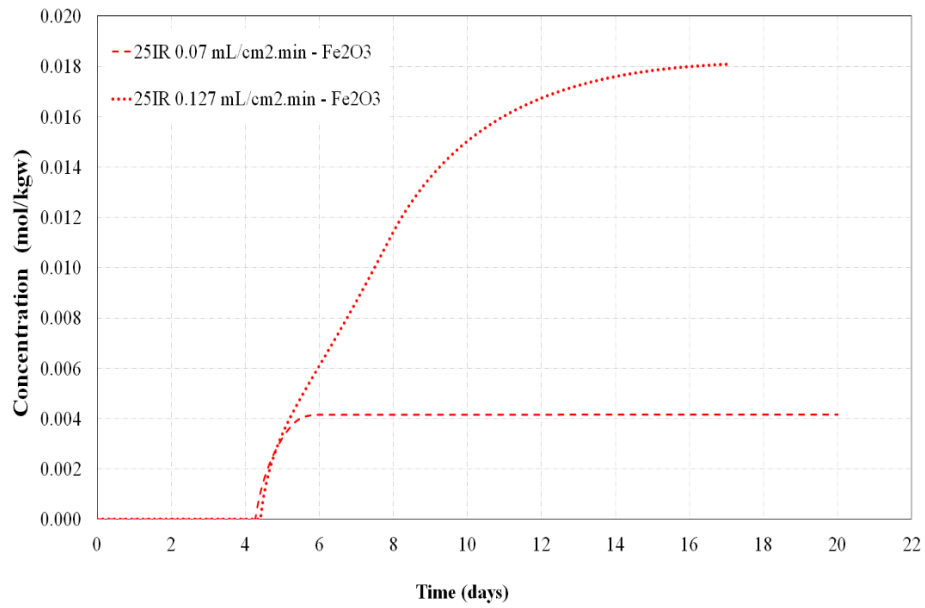


Figure 4.6 Fe<sub>2</sub>O<sub>3</sub> concentration (mol/kgw) versus time for 25IR Columns with 0.07 and 0.127 mL/cm<sup>2</sup>.min fluxes at the first 2 cm of the column

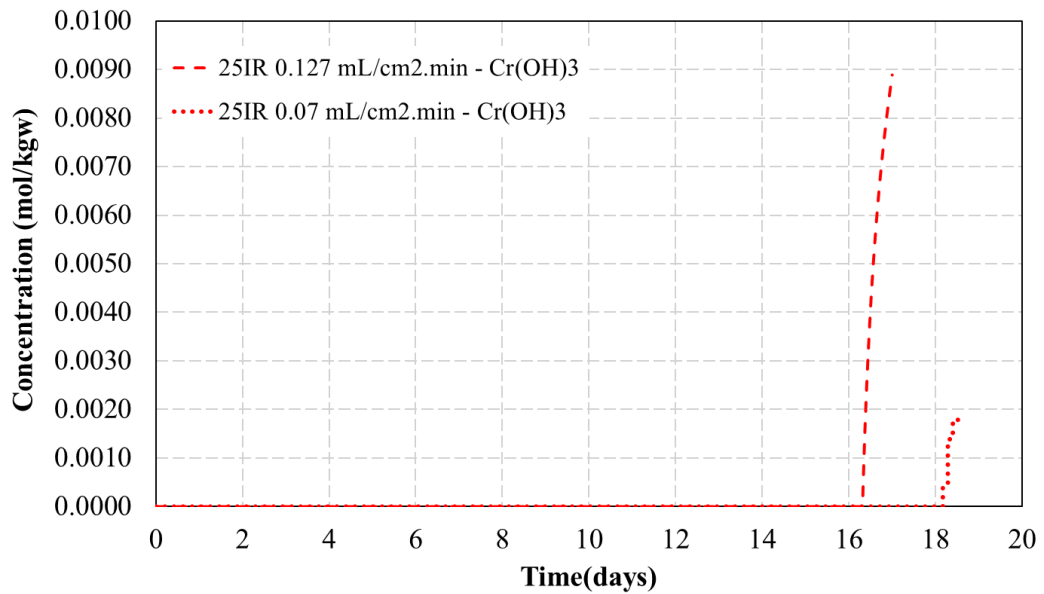


Figure 4.7 Cr(OH)<sub>3</sub> concentration (mol/kgw) versus time for 25IR Columns with 0.07 and 0.127 mL/cm<sup>2</sup>.min fluxes at the first 2 cm and 1 cm of the column, respectively

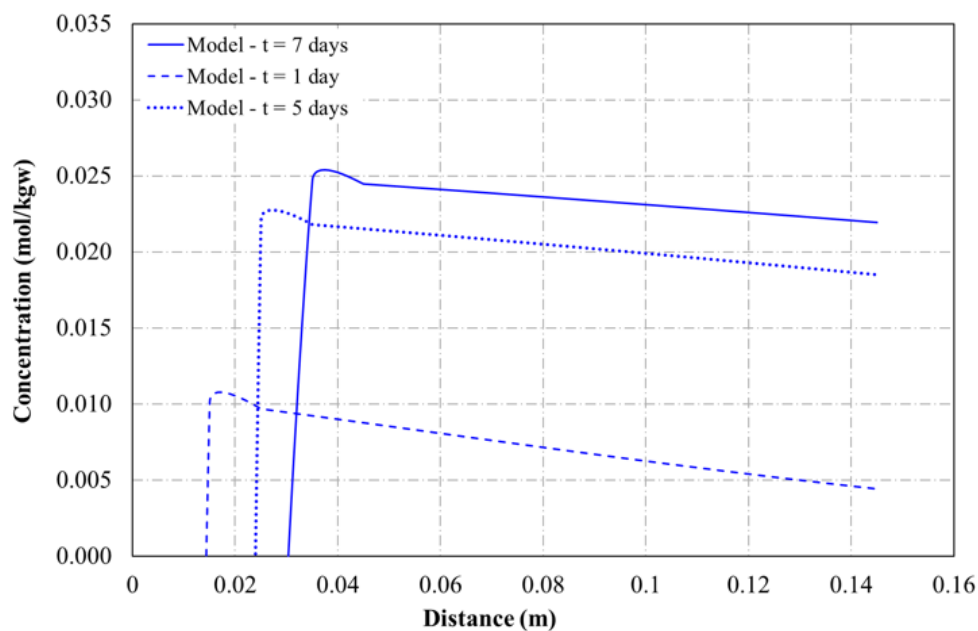


Figure 4.8  $\text{CaCO}_3$  concentration (mol/kgw) versus distance along the column (m) for 10IR Column with  $0.127 \text{ mL/cm}^2 \cdot \text{min}$  flux for day 1, 5, and 7

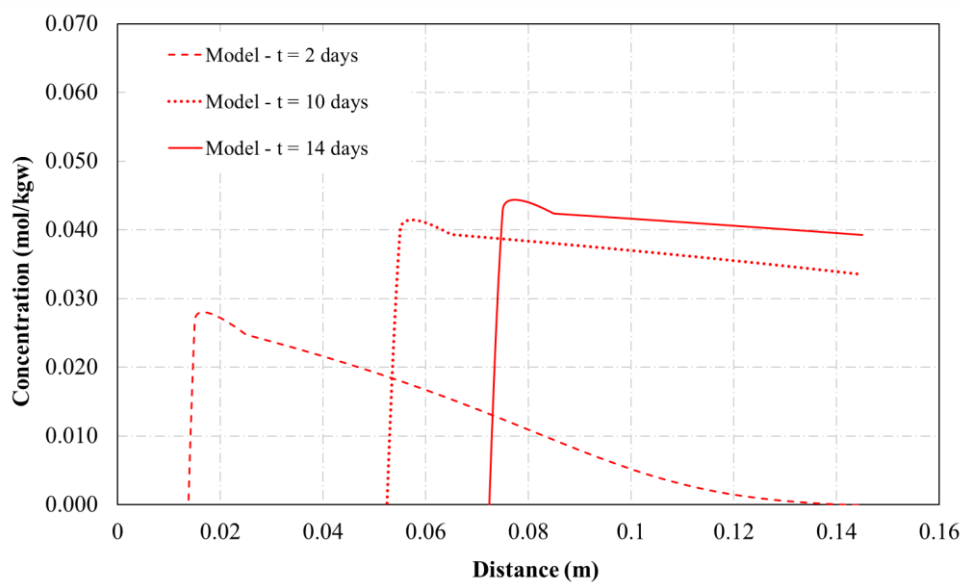


Figure 4.9  $\text{CaCO}_3$  concentration (mol/kgw) versus distance along the column (m) for 25IR Column with  $0.127 \text{ mL/cm}^2 \cdot \text{min}$  flux for day 2, 10 and 14

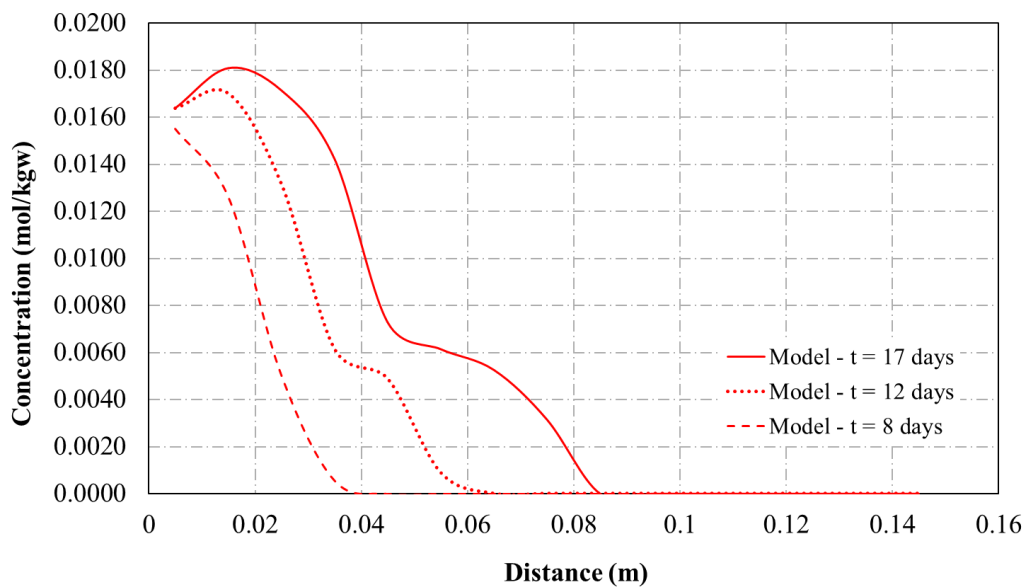


Figure 4.10 Fe<sub>2</sub>O<sub>3</sub> concentration (mol/kgw) versus distance along the column (m) for 25IR Column with 0.127 mL/cm<sup>2</sup>.min flux for day 8, 12 and 17

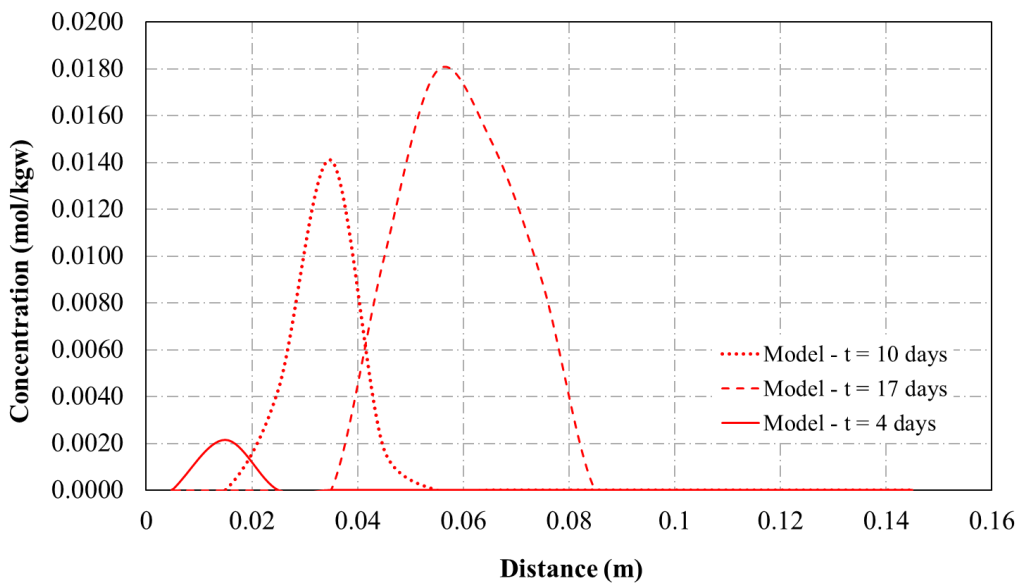


Figure 4.11 Cr(OH)<sub>3</sub> concentration (mol/kgw) versus distance along the column(m) for 25IR Column with 0.127 mL/cm<sup>2</sup>.min flux for day 4, 10 and 17

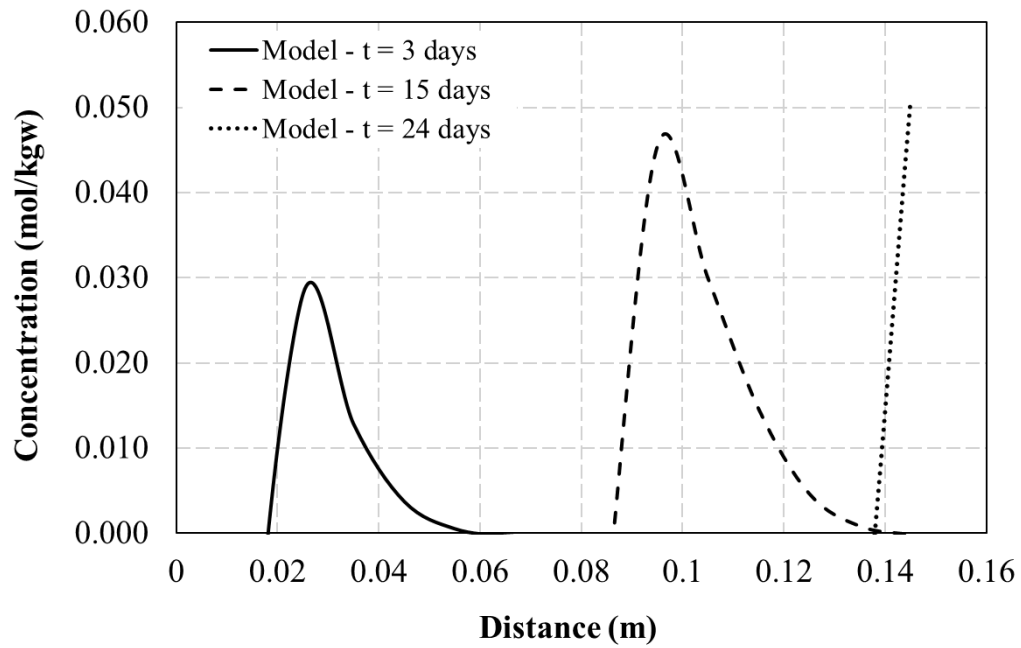


Figure 4.12 CaCO<sub>3</sub> concentration (mol/kgw) versus distance along the column (m) for 50IR Column with 0.127 mL/cm<sup>2</sup>.min flux for day 3, 15 and 24

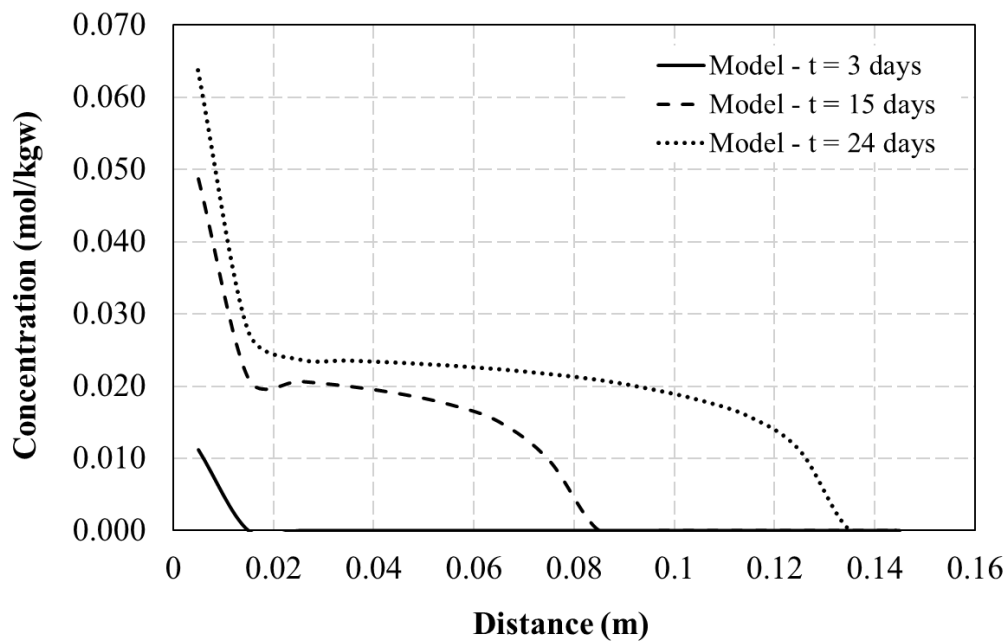


Figure 4.13 Fe<sub>2</sub>O<sub>3</sub> concentration (mol/kgw) versus distance along the column (m) for 50IR Column with 0.127 mL/cm<sup>2</sup>.min flux for day 3, 15 and 24

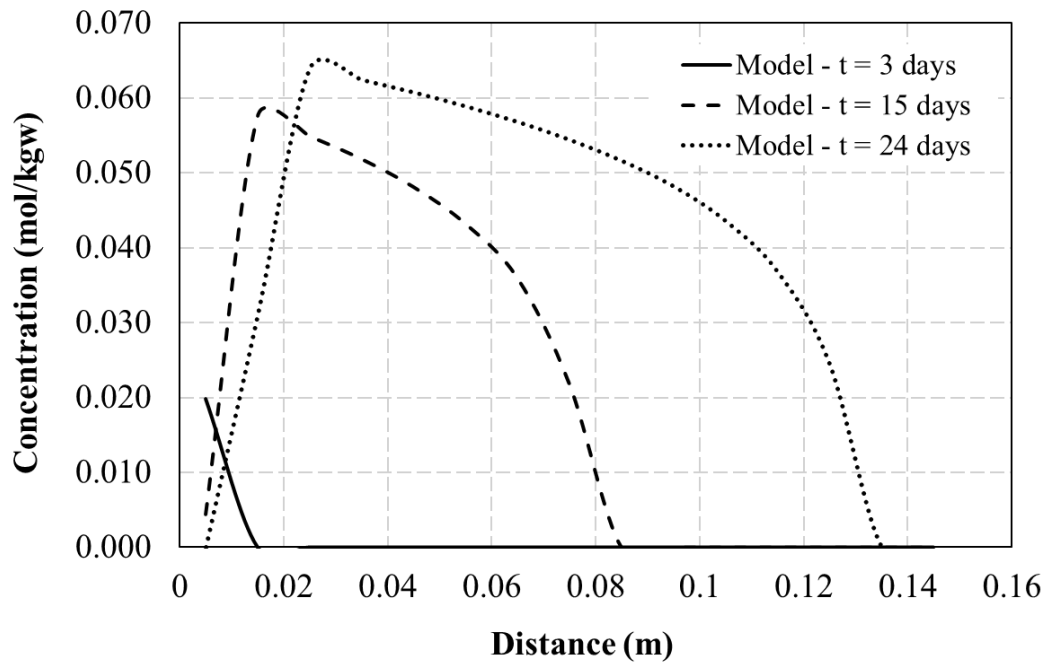


Figure 4.14 Cr(OH)<sub>3</sub> concentration (mol/kgw) versus distance along the column(m) for for 50IR Column with 0.127 mL/cm<sup>2</sup>.min flux for day 3, 15 and 24

Figure 4.5 shows that CaCO<sub>3</sub> mineral accumulates gradually in all column reactors. Simulation results show that the CaCO<sub>3</sub> mineral concentration at the end of the column in the 10IR Column with 0.07 mL/cm<sup>2</sup>.min flux is 2 times higher than that of the 10IR Column with 0.127 mL/cm<sup>2</sup>.min.

As Table 4.5 shows the CaCO<sub>3</sub> proportionality constants are higher for 0.127 mL/cm<sup>2</sup>.min flux column compared to 0.07 mL/cm<sup>2</sup>.min flux simulations, more significant effect on the ZVI reactivity would be expected under higher flowrate operations, as supported by previous works by Jeen et al. (2007); Gui et al. (2009).

In the 25IR columns, model results show that most of the time the column with 0.127 mL/cm<sup>2</sup>.min flux has a higher CaCO<sub>3</sub> mineral concentration compared to the lower flux, although both fluxes have the same proportionality constant,  $\alpha$  for CaCO<sub>3</sub> mineral. Since CaCO<sub>3</sub> mineral concentration is higher at most of the time during the simulation in 0.127 mL/cm<sup>2</sup>.min flux, the reactivity decrease due to CaCO<sub>3</sub> mineral is expected to be more significant than it does with 0.07 mL/cm<sup>2</sup>.min flux.

Comparative simulations for  $\text{Fe}_2\text{O}_3$  mineral with time for both fluxes i.e., Figure 4.6, also shows that  $\text{Fe}_2\text{O}_3$  mineral in  $0.127 \text{ mL/cm}^2\cdot\text{min}$  flux is almost 5 times higher than that of  $0.07 \text{ mL/cm}^2\cdot\text{min}$  flux, where the proportionality constant,  $\alpha$  for  $\text{Fe}_2\text{O}_3$  mineral is also the same between two fluxes. Therefore, similarly the reactivity decrease due to  $\text{Fe}_2\text{O}_3$  mineral is expected to be more significant in higher flux conditions, where the contribution to the overall reactivity decrease is higher and the column will be exhausted earlier.

The mineral distributions along the columns (Figure 4.6-Figure 4.14) show that mineral accumulation is most prominent near the influent end of the column, with particular high concentrations in  $\text{Fe}_2\text{O}_3$  mineral formations. This behavior is mainly due to the oxidation of  $\text{Fe}(0)$  to form  $\text{Fe(III)}$ oxide precipitates; corresponding to the initial decrease in reactivity of ZVI at the influent end of the column. These results are consistent with the solid phase analysis of column experiments, where “upward” sections of 50IR column samples showed high concentrations of iron (hydr)oxides (Uyuşur, 2006; Uyuşur and Ünlü, 2009). The accumulation of minerals near the influent end of the columns is also reported by Jeen et al. (2007).

The model simulation results show that the  $\text{Cr(OH)}_3$  mineral has the lowest concentration among the three minerals as shown by Figure 4.7, Figure 4.11 and Figure 4.14. Also the results demonstrate that  $\text{Cr(OH)}_3$  mineral precipitates in a pulse like behavior along the column and it precipitates mainly at the influent end of the column. The lower  $\text{Cr(III)}$  phase precipitates are also supported by the EDX analysis reported by Uyuşur (2006); Uyuşur and Ünlü (2009). According to Mayer et al. (2001), at field scale PRBs  $\text{Cr(III)}$  concentrations do not exhibit considerable increases and the conditions within the PRBs predominantly promote the production of amorphous  $\text{Cr(OH)}_3$ . These amorphous  $\text{Cr(OH)}_3$  mineral precipitates are reported in a small band near the influent end of the PRB, supporting our model demonstrations (Mayet et al. 2001).

### 4.2.3 Implications on ZVI Reactive Surface Area

The proposed reaction the rate expression used in this study involves both the decrease in reactivity of iron due to the the depletion of Fe(0) and the secondary mineral precipitation. The reactive transport model simulations can further be used to investigate the changes in mole fractions of ZVI with respect to the Cr(VI) reduction reactions and increases in secondary mineral phase mole fractions throughout the column experiments, leading to the decrease in ZVI reactive surface area. In this section, the change in iron concentrations within columns along with the changes in reactive surface area of ZVI are compared and the effect of mineral precipitation is discussed for the varying flux and ZVI concentration conditions.

Comparative simulations demonstrating the changes in the total moles of ZVI with respect to time for 10IR, 25IR and 50IR columns with the 0.07 mL/cm<sup>2</sup>.min and 0.127 mL/cm<sup>2</sup>.min fluxes are given in Figure 4.15.

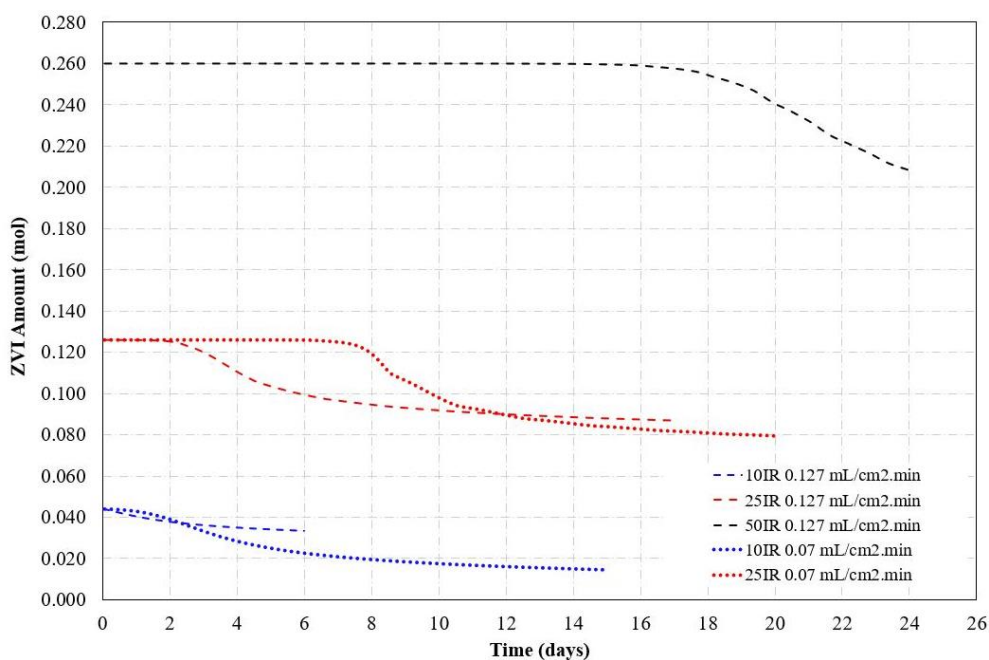


Figure 4.15 Changes in the total moles of ZVI with respect to time for 10IR, 25IR and 50IR columns with the 0.07 mL/cm<sup>2</sup>.min and 0.127 mL/cm<sup>2</sup>.min fluxes

In Figure 4.15, it is seen that the total amount of ZVI is decreased by almost 33% in 10IR Column and it decreased by almost 67% in 25IR Column operated with the 0.07 mL/cm<sup>2</sup>.min flowrates. This shows that after 15 days of simulation in 10IR Column, the 33% of the initially present ZVI amount is used. In case of 25IR Column, 67% of the ZVI initially present is used as a reducing agent within the experiment. The results also reveal that the ZVI reactivity decrease is higher in 25IR Column compared to 10IR Column, consistent with the higher reaction rate constant, and CaCO<sub>3</sub> proportionality constant associated with the 25IR Column (see Table 4.4 and Table 4.5). Since the 25IR Column has a higher amount of ZVI, the required reactivity decrease in ZVI would require higher rate constant and proportionality constant values to be set in the model as expected.

Comparing the simulation results for the operation of 0.127 mL/cm<sup>2</sup>.min flowrates in 10IR, 25IR and 50IR columns, it is seen that the amount of ZVI is decreased by almost 22% in 10IR Column and it decreased by almost 33% in 25IR Column, whereas within the first 7 days of simulation, the decrease in the total ZVI amount in the 50IR Column was not significant. As stated previously, with 50IR Column the exhaustion starts after the 10<sup>th</sup> day of the simulation. Figure 4.15 shows that at the end of 24 days of simulation, the ZVI amount decreases by almost 20%. When the decrease in the amounts of ZVI reactivity are compared, it can be concluded that 50IR Column provides the best remediation activity among the columns and the passivization of the reactive media due to mineral precipitation was not as effective as it was with 10IR and 25IR Columns.

According to a study conducted by Wanner et al. (2011), after 100 days of simulation at most 4.4% of the initial ZVI volume fraction was used as a reducing agent by various oxidized agents. It should be mentioned that in Wanner et al. (2011) work, the reactive surface area update was dependent on volume fraction of the minerals and the change in porosity. According to Uyuşur (2006), the mineral precipitation during the experiments does not significantly affect the porosity of the columns; therefore any changes in porosity are not considered in this work. So the change in porosity within the Wanner et al.'s (2011) work, in addition to other factors including

the type of ZVI media used, might explain their relatively lower ZVI volumetric fraction decrease.

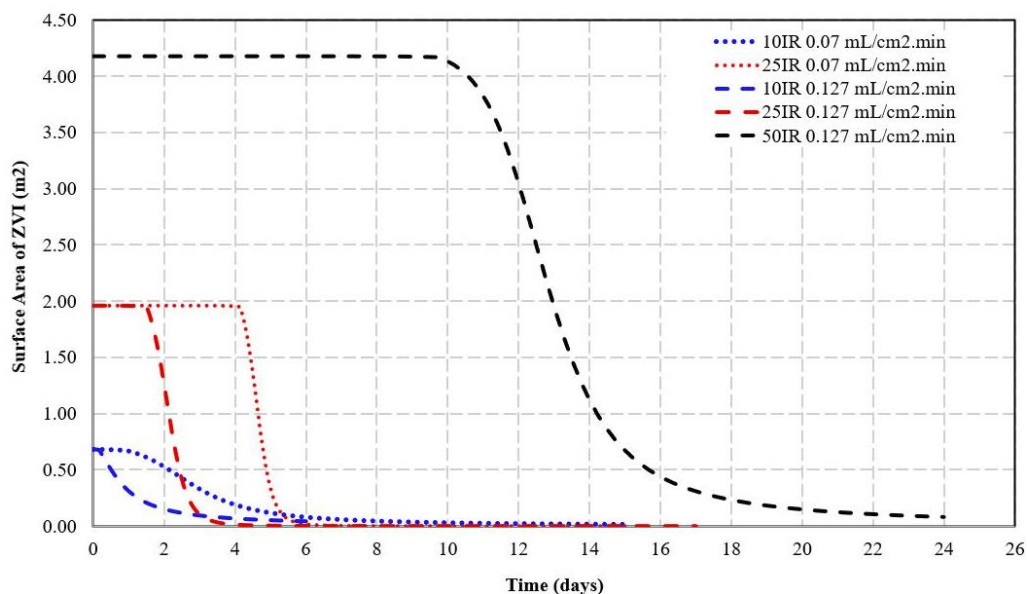


Figure 4.16 Changes in the reactive surface area of ZVI ( $\text{m}^2$ ) with respect to time for 10IR, 25IR and 50IR columns with the  $0.07 \text{ mL/cm}^2.\text{min}$  and  $0.127 \text{ mL/cm}^2.\text{min}$  fluxes

Figure 4.16 shows the calculated changes in the reactive surface area of ZVI ( $\text{m}^2$ ) with respect to time for 10IR, 25IR and 50IR columns with the  $0.07 \text{ mL/cm}^2.\text{min}$  and  $0.127 \text{ mL/cm}^2.\text{min}$  fluxes. From Figure 4.16, it is seen that the reactive surface area of the ZVI is decreased completely at the end of simulation. It can be inferred that within the 4 days of simulation, the reactive surface area of the reactive media within the 10IR Column operated at  $0.07 \text{ mL/cm}^2.\text{min}$  flux is decreased by 74%, whereas within the 25IR Column it did not change. However, from day 4 to day 6 i.e., within 2 days the reactive surface area decreased by 100%. This situation shows that although at the end of the simulation, there was ZVI present within the columns, the surface area of this reactive media is covered with secondary minerals such as  $\text{CaCO}_3$ ,  $\text{Fe}_2\text{O}_3$  and  $\text{Cr}(\text{OH})_3$ . With 10IR Column, the decrease in reactive surface area starts almost at the first day of the simulation, corresponding to the increase in effluent Cr concentrations at the end of the column. This behavior can also be seen

with 25IR Column, where the exhaustion starts after the 4th day of the simulation as shown in Figure 4.3 and in parallel, the reactive surface area of the referred column starts to decrease with the 4th day of the simulation.

Figure 4.16 shows that within the 10IR Column with 0.127 flux, starting from the first day of the simulation, the reactive surface area of the ZVI decreases and by the almost 4th day of the simulation, the reactive surface area is consumed completely. For the 25IR Column, for almost 2 days, the reactive surface area does not change, however afterwards the reactive surface area decreases and within almost 2 days it is consumed completely. In parallel to this, the exhaustion of the columns starts from the day 1 and day 2 of the simulations with 10IR and 25IR Columns, respectively. For the 50IR Column, the reactive surface area starts to decrease after the 10th day of the simulation and in parallel to this the column exhaustion starts after the 10th day of the simulation as shown in Figure 4.16. Therefore, these results demonstrate the impact of surface passivation by the precipitation of secondary minerals including  $\text{CaCO}_3$ ,  $\text{Fe}_2\text{O}_3$  and  $\text{Cr}(\text{OH})_3$ , despite the presence of ZVI throughout the column for Cr reduction.

The precipitation of secondary minerals within the system are also impacted by the change of pH during the Cr(VI) reduction process. It should be mentioned that pH can be influenced by other species in the solution other than the ZVI corrosion and mineral precipitation. In general it is stated that at the influent end of the column a pH increase is observed and afterwards pH profiles becomes flat, where the pH increase is associated with ZVI corrosion and afterwards carbonate buffers keep the pH stable in the system (Wanner et al.,2011; Jeen et al.,2007; Gui et al.,2009). The pH profiles of the 10IR, 25IR and 50IR Columns with 0.127 mL/cm<sup>2</sup>.min flux are shown in Figure 4.17, corresponding to day 5, 10 and 20 of the simulation period.

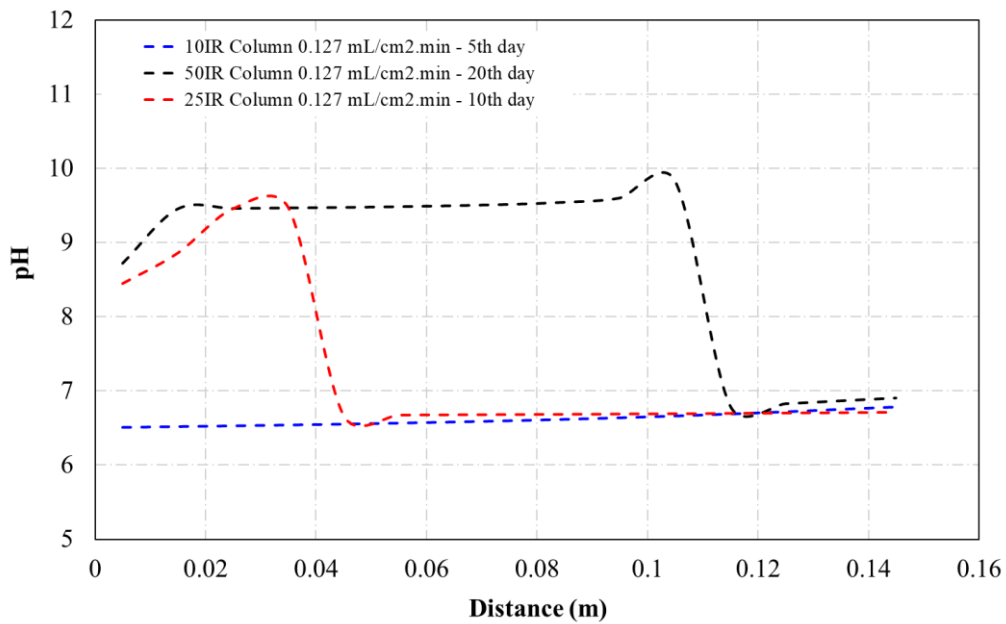


Figure 4.17 pH change along the 10IR, 25IR and 50IR Columns with 0.127 mL/cm<sup>2</sup>.min flux at day 5, 10 and 20, respectively

Figure 4.17 shows a very slight increase in pH along the 10IR Column which can be associated with iron corrosion. The absence of Fe<sub>2</sub>O<sub>3</sub> and Cr(OH)<sub>3</sub> precipitation and the presence of CaCO<sub>3</sub> throughout the column provides a buffering capacity to remain the pH relatively stable. In the 25IR Column, firstly pH increases and then it suddenly drops and the pH profile flattens. Similar to 25IR Columns, with 50IR Column the pH increases first and then flattens. The pH level stays alkaline between 2 cm the 10 cm of the column and then drops to around neutral values. Again the initial pH increase is the result of Fe(0) oxidation by Cr reduction reaction in the columns and with 50IR the high pH conditions are maintained longer along the column compared to the other columns. Then the gradual decrease in Fe<sub>2</sub>O<sub>3</sub> formation due to the decrease in Fe(0) oxidation reaction allows the system for Cr(OH)<sub>3</sub> precipitation, which lowers the pH. After the gradual decrease in Cr(OH)<sub>3</sub> formation, CaCO<sub>3</sub> precipitation occurs which buffers the system, keeping pH nearly constant in the remaining portion along the columns.

### 4.3 Sensitivity Analysis

Sensitivity analysis can be defined as a tool to measure how the variability in input parameters affect the output of a model. In this study, sensitivity analysis is performed only for kinetic parameters, including rate constant (k) and the mineral proportionality constants ( $\alpha$ -CaCO<sub>3</sub>,  $\alpha$ -Fe<sub>2</sub>O<sub>3</sub> and  $\alpha$ -Cr(OH)<sub>3</sub>).

As a sensitivity analysis method one-at-a-time (OAT) technique is used which means that one input variable is changed while the other input parameters are kept constant. Analysis mainly performed to show how the model output deviates i.e., C/C<sub>0</sub> versus time profiles, when one specific model input parameter is increased or decreased by a certain amount while the other parameters are kept constant.

The sensitivity of the model to a specific parameter can be calculated by the Normalized Parameter Sensitivity ( $S_P$ ) index as follows (Hamby, 1994).

$$S_P = \frac{C_{P+\Delta P} - C_{base}}{C_{base}} \times \left| \frac{P}{\Delta P} \right| \quad (\text{Eqn 19})$$

where, P denotes parameter and  $\Delta P$  denotes change in parameter,  $C_{base}$  is the model output in base case and  $C_{P+\Delta P}$  is the model output when the input parameter P is changed in  $\Delta P$  amount.

As explained previously, the input parameters of the model are rate constant, k and proportionality constant,  $\alpha$  values of minerals CaCO<sub>3</sub>, Fe<sub>2</sub>O<sub>3</sub> and Cr(OH)<sub>3</sub>. The model output of 10IR Column with 0.07 and 0.127 mL/cm<sup>2</sup>.min fluxes, 25IR Column with 0.07 and 0.127 mL/cm<sup>2</sup>.min fluxes and 50IR Column with 0.127 mL/cm<sup>2</sup>.min flux are assessed by increasing and decreasing the calibrated value of the referred input parameters by 50%. The referred S index is calculated for 5 time intervals to cover the C/C<sub>0</sub> profile. The S index values are later summarized to reach a total value of  $S_P$ .

The change in C/C0 profiles as a result of referred increase and decrease in input parameters and the calculated S<sub>P</sub> indexes are presented for each column separately below.

#### 4.3.1 Sensitivity Analysis for 10IR Columns

In Table 4.6 below, the calibrated values of the input parameters are given. In scope of sensitivity analysis, each of these parameters are increased and decreased by 50% while the other parameters are kept constant. In this regard, there are 4 cases for each 10IR Columns other than base case. The referred cases are shown in Table 4.6. Case 1 and 2 show the values of input parameters when the rate constant values are increased and decreased by 50%, respectively. Case 3 and 4 show the values of input parameters when the proportionality constant,  $\alpha$  for CaCO<sub>3</sub> mineral is increased and decreased by 50%, respectively. The change in C/C0 profiles can be seen between Figure 4.18 and Figure 4.21.

Table 4.6 The values of input parameters for each case of sensitivity analysis with 10IR Columns with 0.07 and 0.127 mL/cm<sup>2</sup>.min fluxes

	<b>Input Parameter</b>	<b>10IR 0.07 mL/cm<sup>2</sup>.min Flux</b>	<b>10IR 0.127 mL/cm<sup>2</sup>.min Flux</b>
<b>Base Case</b>	Rate Constant, k (L/m <sup>2</sup> .sec)	7.30×10 <sup>-5</sup>	2.12×10 <sup>-5</sup>
	$\alpha$ - CaCO <sub>3</sub>	200	450
<b>Case 1</b>	Rate Constant, k (L/m <sup>2</sup> .sec)	1.09×10 <sup>-4</sup>	3.18×10 <sup>-5</sup>
	$\alpha$ - CaCO <sub>3</sub>	200	450
<b>Case 2</b>	Rate Constant, k (L/m <sup>2</sup> .sec)	3.65×10 <sup>-5</sup>	1.06×10 <sup>-5</sup>
	$\alpha$ - CaCO <sub>3</sub>	200	450

**Table 4.6 (Continued)**

	<b>Input Parameter</b>	<b>10IR 0.07 mL/cm<sup>2</sup>.min Flux</b>	<b>10IR 0.127 mL/cm<sup>2</sup>.min Flux</b>
<b>Case 3</b>	Rate Constant, k (L/m <sup>2</sup> .sec) $\alpha$ - CaCO <sub>3</sub>	$7.30 \times 10^{-5}$ 300	$2.12 \times 10^{-5}$ 675
<b>Case 4</b>	Rate Constant, k (L/m <sup>2</sup> .sec) $\alpha$ - CaCO <sub>3</sub>	$7.30 \times 10^{-5}$ 100	$2.12 \times 10^{-5}$ 225

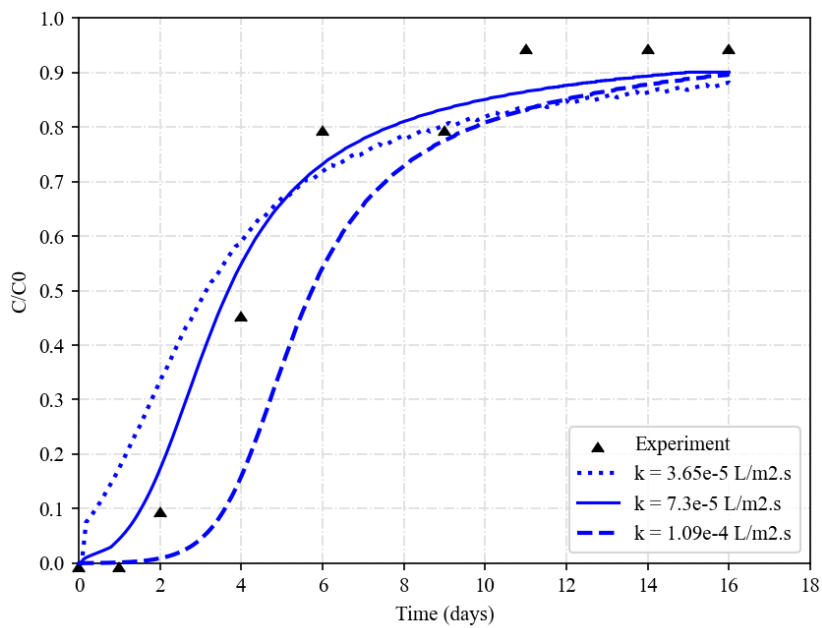


Figure 4.18 Change in C/C0 vs time graph of 10IR Column 0.07 mL/cm<sup>2</sup>.min flux for Case 1 and Case 2 – 50% increase and decrease in rate constant,k

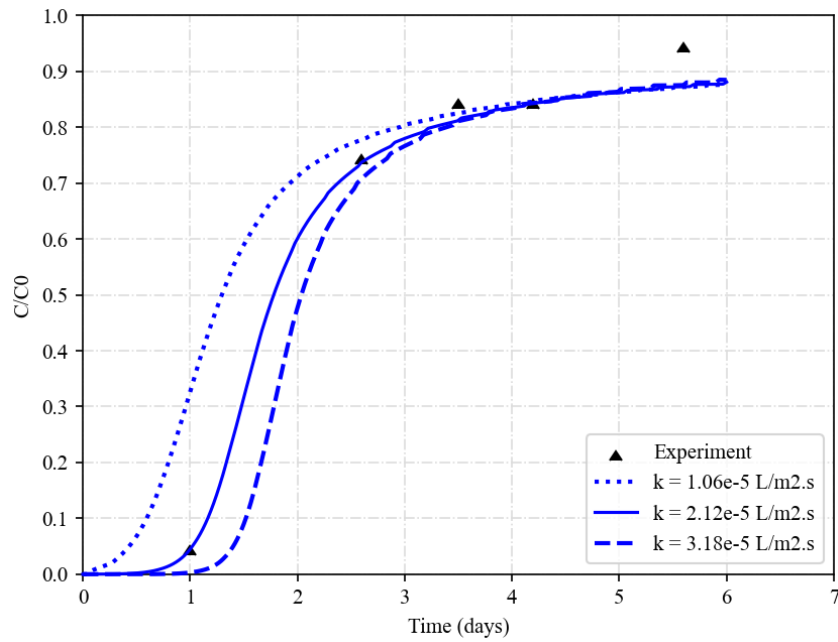


Figure 4.19 Change in  $C/C_0$  vs time graph of 10IR Column  $0.127 \text{ mL/cm}^2 \cdot \text{min}$  flux for Case 1 and Case 2 - 50% increase and decrease in rate constant,  $k$

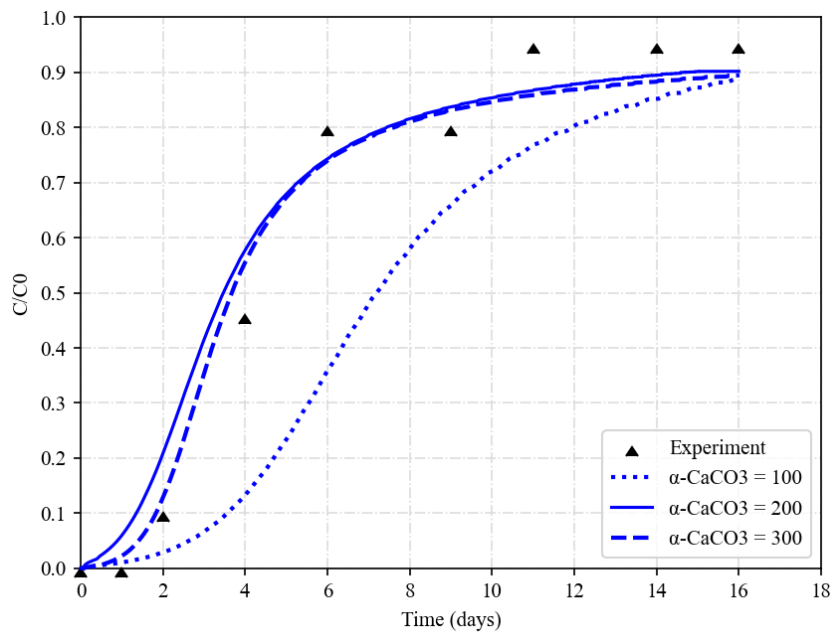


Figure 4.20 Change in  $C/C_0$  vs time graph of 10IR Column  $0.07 \text{ mL/cm}^2 \cdot \text{min}$  flux for Case 3 and Case 4 - 50% increase and decrease in  $\alpha - \text{CaCO}_3$

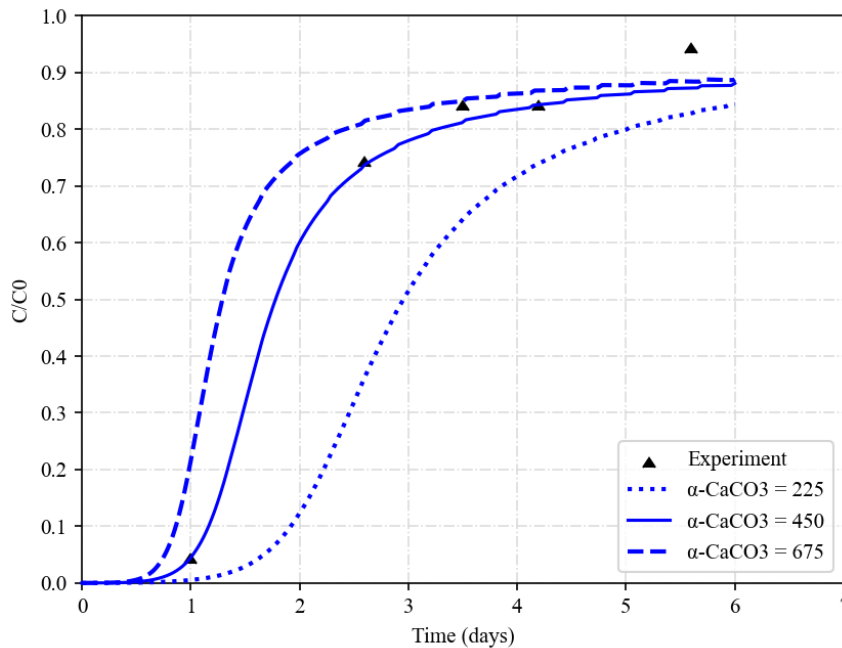


Figure 4.21 Change in  $C/C_0$  vs time graph of 10IR Column  $0.127 \text{ mL/cm}^2 \cdot \text{min}$  flux for Case 3 and Case 4 – 50% increase and decrease in  $\alpha - \text{CaCO}_3$

For the 10IR Column with  $0.07 \text{ mL/cm}^2 \cdot \text{min}$  flux, the experimental and model results show that starting from the day 1, Cr(VI) can be detected at the effluent which means  $C/C_0$  takes a value different than zero. Figure 4.18 shows that when the rate constant,  $k$  is increased by 50%, the first detection of Cr(VI) at the effluent is delayed. And when the rate constant,  $k$  value decreased by 50%, the first detection of Cr(VI) at the effluent occur earlier compared to base condition.

As shown in Figure 4.19, the effluent Cr(VI) is measured at the first day of the simulation for the base condition as well as for the cases where rate constant,  $k$  value is decreased and increased by 50%. However, when the rate constant,  $k$  value decreased by 50%,  $C/C_0$  reaches to higher values than the case where rate constant,  $k$  value increased by 50%.

The sensitivity of the model for the proportionality constant,  $\alpha$  for mineral  $\text{CaCO}_3$  with 10IR Column  $0.07 \text{ mL/cm}^2 \cdot \text{min}$  is assessed in Figure 4.20. As one can see when

the  $\alpha$  -  $\text{CaCO}_3$  increased by 50%, the simulation results did not deviate much from the base condition compared to case where  $\alpha$  -  $\text{CaCO}_3$  decreased by 50%.

The sensitivity of model for the proportionality constant,  $\alpha$  for mineral  $\text{CaCO}_3$  with 10IR Column  $0.127 \text{ mL/cm}^2\cdot\text{min}$  is assessed in Figure 4.21. As one can see when the  $\alpha$  -  $\text{CaCO}_3$  decreased by 50%, the  $C/C_0$  values decrease at any time during simulation. And when the  $\alpha$  -  $\text{CaCO}_3$  increased by 50%, the  $C/C_0$  values increase at any time during simulation. The results in case where  $\alpha$  -  $\text{CaCO}_3$  decreased by 50% deviated more from the base condition compared to the case where  $\alpha$  -  $\text{CaCO}_3$  increased by 50%.

Normalized parameter sensitivity values ( $S_P$ ) are calculated for rate constant,  $k$  and proportionality constant for  $\text{CaCO}_3$  mineral,  $\alpha$  -  $\text{CaCO}_3$ . For the rate constant,  $k$ , the calculated  $S_P$  indexes are given by Table 4.7 and Table 4.8. The  $S_P$  indexes for the proportionality constant,  $\alpha$  -  $\text{CaCO}_3$  are given by Table 4.9 and Table 4.10.

Table 4.7 Normalized Parameter Sensitivity Index Calculation for 10IR Column - 0.07 ml/cm<sup>2</sup>.min flux –Case 1 and 2

Parameter	Base Case Value (P)	Perturbation in Parameter Value (P+ΔP)	P/ΔP	Base Case Model Output - C/C0 C <sub>P</sub>	Time (day)	Model Output (Case 1 and 2) C <sub>P+ΔP</sub>	Normalized Parameter Sensitivity (S <sub>P</sub> )			
Rate Constant, k (L/m <sup>2</sup> .s)	7.30×10 <sup>-5</sup>	1.09×10 <sup>-4</sup> Case 1	2	0.18	at day 2	0.00	-2.00			
				0.55	at day 4	0.17	-1.38			
				0.72	at day 6	0.55	-0.47			
				0.82	at day 9	0.78	-0.10			
				0.87	at day 11	0.82	-0.11			
				0.90	at day 14	0.88	-0.04			
				0.18	at day 2	0.35	1.89			
	3.65×10 <sup>-5</sup> Case 2	2	0.55	at day 4	0.60	0.18				
			0.72	at day 6	0.71	-0.03				
			0.82	at day 9	0.80	-0.05				
			0.87	at day 11	0.82	-0.11				
			0.90	at day 14	0.87	-0.07				
			<b>Sum of S<sub>P</sub></b>							<b>-2.30</b>

Table 4.8 Normalized Parameter Sensitivity Index Calculation for 10IR Column - 0.127 ml/cm<sup>2</sup>.min flux –Case 1 and 2

Parameter	Base Case Value (P)	Perturbation in Parameter Value (P+ΔP)	P/ΔP	Base Case Model Output - C/C0 Cp	Time (day)	Model Output (Case 1 and 2) Cp+AP	Normalized Parameter Sensitivity (Sp)
Rate Constant, k (L/m <sup>2</sup> .s)	2.12×10 <sup>-5</sup>	3.18×10 <sup>-5</sup> Case 1	2	0.75	at day 1	0.70	-0.13
				0.85	at day 2	0.83	-0.05
				0.88	at day 3	0.85	-0.07
				0.90	at day 4	0.88	-0.04
				0.90	at day 5	0.88	-0.04
				0.90	at day 6	0.88	-0.04
	2.12×10 <sup>-5</sup>	1.06×10 <sup>-5</sup> Case 2	2	0.75	at day 1	0.82	0.19
				0.85	at day 2	0.88	0.07
				0.88	at day 3	0.91	0.07
				0.90	at day 4	0.94	0.09
				0.90	at day 5	0.95	0.11
				0.90	at day 6	0.95	0.11
<b>Sum of Sp</b>						<b>0.25</b>	

Table 4.9 Normalized Parameter Sensitivity Index Calculation for 10IR Column - 0.07 ml/cm<sup>2</sup>.min flux –Case 3 and 4

Parameter	Base Case Value (P)	Perturbation in Parameter Value (P+ΔP)	P/ΔP	Base Case Model Output - C/C0 Cp	Time (day)	Model Output (Case 3 and 4) Cp+ΔP	Normalized Parameter Sensitivity (Sp)		
Proportinality constant, $\alpha$ - CaCO <sub>3</sub>	200	300 Case 3	2	0.18	at day 2	0.12	-0.67		
				0.55	at day 4	0.54	-0.04		
				0.72	at day 6	0.72	0.00		
				0.82	at day 9	0.81	-0.02		
				0.87	at day 11	0.86	-0.02		
				0.90	at day 14	0.89	-0.02		
				0.18	at day 2	0.03	-1.67		
	100 Case 4	2	0.55	at day 4	0.12	-1.56			
			0.72	at day 6	0.37	-0.97			
			0.82	at day 9	0.66	-0.39			
			0.87	at day 11	0.77	-0.23			
			0.90	at day 14	0.85	-0.11			
			<b>Sum of Sp</b>						<b>-5.71</b>

Table 4.10 Normalized Parameter Sensitivity Index Calculation for 10IR Column - 0.127 ml/cm<sup>2</sup>.min flux –Case3 and 4

Parameter	Base Case Value (P)	Perturbation in Parameter Value (P+ΔP)	P/ΔP	Base Case Model Output - C/C0 Cp	Time (day)	Model Output (Case 3 and 4) Cp+ΔP	Normalized Parameter Sensitivity (Sp)
Proportionality constant, $\alpha$ - CaCO <sub>3</sub>	450	675 Case 3	2	0.75	at day 1	0.82	0.19
				0.85	at day 2	0.88	0.07
				0.88	at day 3	0.91	0.07
				0.90	at day 4	0.92	0.04
				0.90	at day 5	0.92	0.04
				0.90	at day 6	0.92	0.04
	450	225 Case 4	2	0.75	at day 1	0.65	-0.27
				0.85	at day 2	0.78	-0.16
				0.88	at day 3	0.82	-0.14
				0.90	at day 4	0.85	-0.11
				0.90	at day 5	0.87	-0.07
				0.90	at day 6	0.88	-0.04
<b>Sum of Sp</b>							<b>-0.33</b>

As explained above, for 10IR Columns with 0.07 and 0.127 mL/cm<sup>2</sup>.min fluxes, the simulation results with the defined cases are compared to see how the model results change. The deviations from the base conditions are expressed with normalized parameter sensitivity index (S<sub>P</sub>). Table 4.11 summarizes the absolute values of the S<sub>P</sub> index for each of the columns.

Table 4.11 Absolute S<sub>P</sub> values of the rate constant, k and proportionality constant, α-CaCO<sub>3</sub> for 10IR Columns with 0.07 and 0.127 mL/cm<sup>2</sup>.min fluxes

Parameter	10IR 0.07 mL/cm <sup>2</sup> .min - S <sub>P</sub>	10IR 0.127 mL/cm <sup>2</sup> .min - S <sub>P</sub>
Rate Constant, k (L/m <sup>2</sup> .s)	2.30	0.25
Proportionality Constant, α - CaCO <sub>3</sub>	5.71	0.33

Higher the value of S<sub>P</sub>, the greater the sensitivity of the model for that parameter. As shown in Table 4.11, S<sub>P</sub> values for the α - CaCO<sub>3</sub> parameter are higher than that of rate constant, k. In this regard, one can say that for the 10IR Columns the model is more sensitive to α - CaCO<sub>3</sub> parameter than it is with rate constant, k.

#### 4.3.2 Sensitivity Analysis for 25IR Columns

Similar to 10IR Columns, for 25IR Columns, each input parameter is increased and decreased by 50% one-at-a-time and the change in C/C<sub>0</sub> profiles are shown. With 25IR Columns, there are 3 proportionality constant, α values: α - CaCO<sub>3</sub>, α - Fe<sub>2</sub>O<sub>3</sub> and α - Cr(OH)<sub>3</sub>. So, there are 8 cases other than base case to assess in scope of sensitivity analysis for each column. The referred cases are given by Table 4.12 below. The change in C/C<sub>0</sub> profiles can be seen between Figure 4.22 and Figure 4.29.

Table 4.12 The values of input parameters for each case of sensitivity analysis with 25IR Columns with 0.07 and 0.127 mL/cm<sup>2</sup>.min fluxes

	<b>Input Parameter</b>	<b>25IR 0.07 mL/cm<sup>2</sup>.min Flux</b>	<b>25IR 0.127 mL/cm<sup>2</sup>.min Flux</b>
<b>Base Case</b>	Rate Constant, k (L/m <sup>2</sup> .sec)	2.11×10 <sup>-4</sup>	6.30×10 <sup>-5</sup>
	α – CaCO <sub>3</sub>	300	300
	α – Fe <sub>2</sub> O <sub>3</sub>	300	300
	α – Cr(OH) <sub>3</sub>	500	500
<b>Case 1</b>	Rate Constant, k (L/m <sup>2</sup> .sec)	3.17×10 <sup>-4</sup>	9.45×10 <sup>-5</sup>
	α – CaCO <sub>3</sub>	300	300
	α – Fe <sub>2</sub> O <sub>3</sub>	300	300
	α – Cr(OH) <sub>3</sub>	500	500
<b>Case 2</b>	Rate Constant, k (L/m <sup>2</sup> .sec)	1.06×10 <sup>-4</sup>	3.15×10 <sup>-5</sup>
	α – CaCO <sub>3</sub>	300	300
	α – Fe <sub>2</sub> O <sub>3</sub>	300	300
	α – Cr(OH) <sub>3</sub>	500	500
<b>Case 3</b>	Rate Constant, k (L/m <sup>2</sup> .sec)	2.11×10 <sup>-4</sup>	6.30×10 <sup>-5</sup>
	α – CaCO <sub>3</sub>	450	450
	α – Fe <sub>2</sub> O <sub>3</sub>	300	300
	α – Cr(OH) <sub>3</sub>	500	500
<b>Case 4</b>	Rate Constant, k (L/m <sup>2</sup> .sec)	2.11×10 <sup>-4</sup>	6.30×10 <sup>-5</sup>
	α – CaCO <sub>3</sub>	150	150

**Table 4.12 (Continued)**

	<b>Input Parameter</b>	<b>25IR 0.07</b> <b>mL/cm<sup>2</sup>.min</b>	<b>25IR 0.127</b> <b>mL/cm<sup>2</sup>.min</b>
		<b>Flux</b>	<b>Flux</b>
<b>Case 5</b>	Rate Constant, k (L/m <sup>2</sup> .s)	2.11×10 <sup>-4</sup>	6.30×10 <sup>-5</sup>
	α – CaCO <sub>3</sub>	300	300
	α – Fe <sub>2</sub> O <sub>3</sub>	450	450
	α – Cr(OH) <sub>3</sub>	500	500
<b>Case 6</b>	Rate Constant, k (L/m <sup>2</sup> .s)	2.11×10 <sup>-4</sup>	6.30×10 <sup>-5</sup>
	α – CaCO <sub>3</sub>	300	300
	α – Fe <sub>2</sub> O <sub>3</sub>	150	150
	α – Cr(OH) <sub>3</sub>	500	500
<b>Case 7</b>	Rate Constant, k (L/m <sup>2</sup> .s)	2.11×10 <sup>-4</sup>	6.30×10 <sup>-5</sup>
	α – CaCO <sub>3</sub>	300	300
	α – Fe <sub>2</sub> O <sub>3</sub>	300	300
	α – Cr(OH) <sub>3</sub>	750	750
<b>Case 8</b>	Rate Constant, k (L/m <sup>2</sup> .s)	2.11×10 <sup>-4</sup>	6.30×10 <sup>-5</sup>
	α – CaCO <sub>3</sub>	300	300
	α – Fe <sub>2</sub> O <sub>3</sub>	300	300
	α – Cr(OH) <sub>3</sub>	250	250

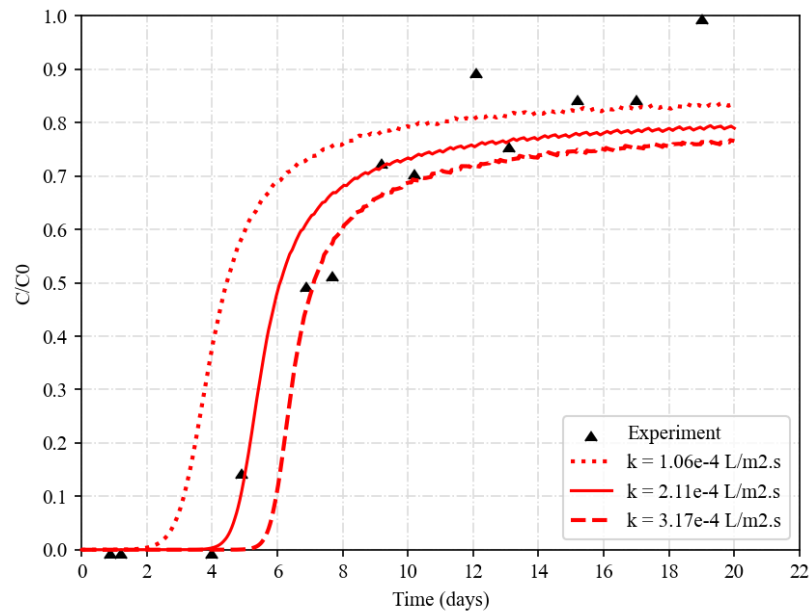


Figure 4.22 Change in  $C/C_0$  vs time graph of 25IR Column  $0.07 \text{ mL/cm}^2 \cdot \text{min}$  flux for Case 1 and Case 2 – 50% increase and decrease in rate constant,  $k$

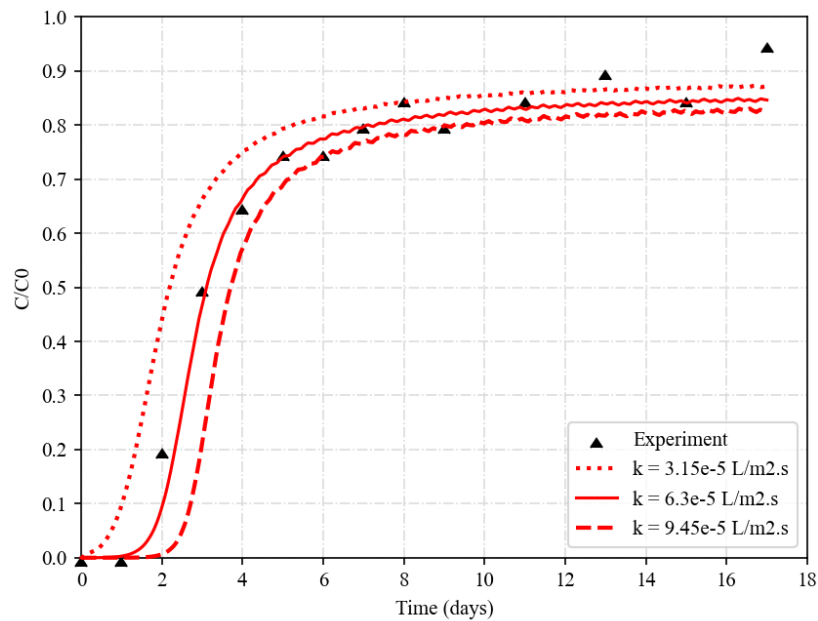


Figure 4.23 Change in  $C/C_0$  vs time graph of 25IR Column  $0.127 \text{ mL/cm}^2 \cdot \text{min}$  flux for Case 1 and Case 2 - 50% increase and decrease in rate constant,  $k$

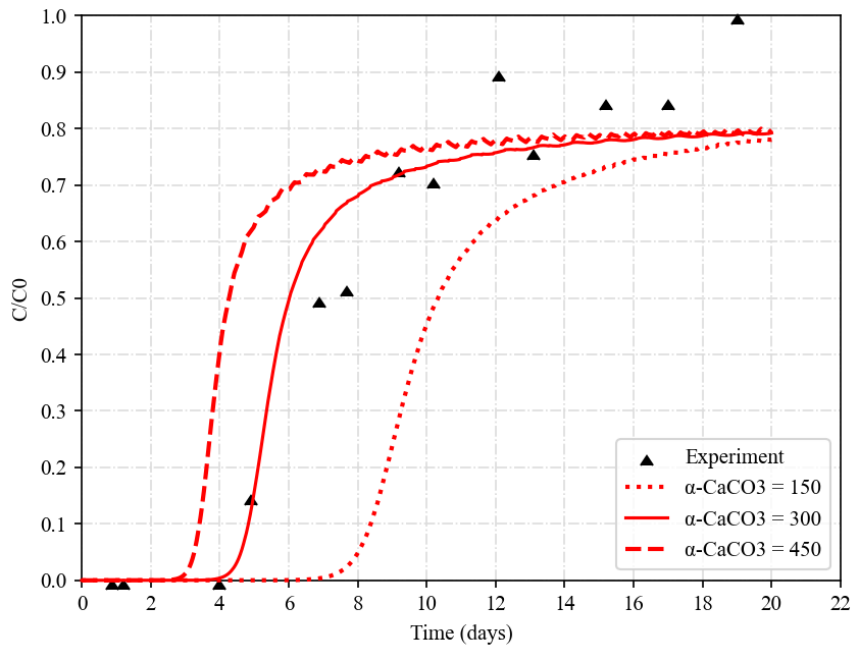


Figure 4.24 Change in  $C/C_0$  vs time graph of 25IR Column  $0.07 \text{ mL/cm}^2 \cdot \text{min}$  flux for Case 3 and Case 4 – 50% increase and decrease in  $\alpha\text{-CaCO}_3$

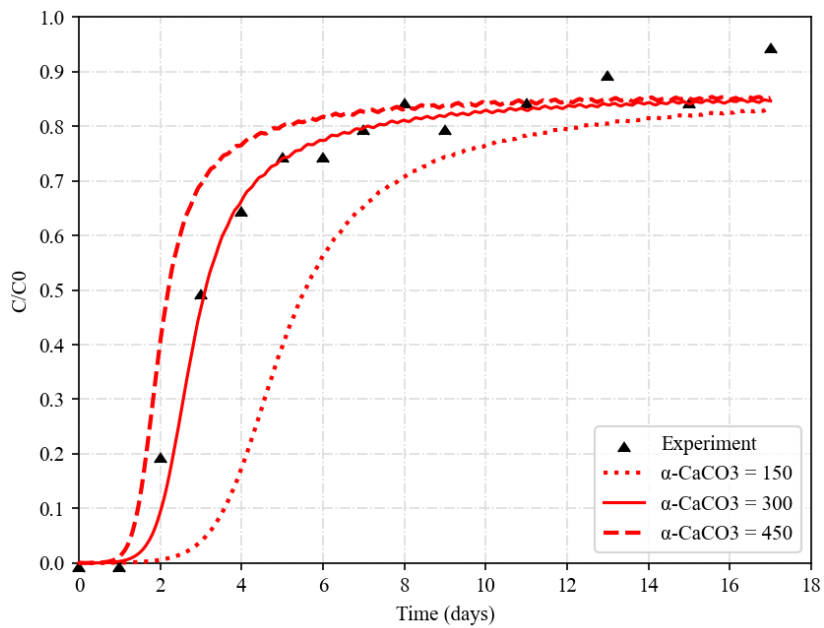


Figure 4.25 Change in  $C/C_0$  vs time graph of 25IR Column  $0.127 \text{ mL/cm}^2 \cdot \text{min}$  flux for Case 3 and Case 4 – 50% increase and decrease in  $\alpha\text{-CaCO}_3$

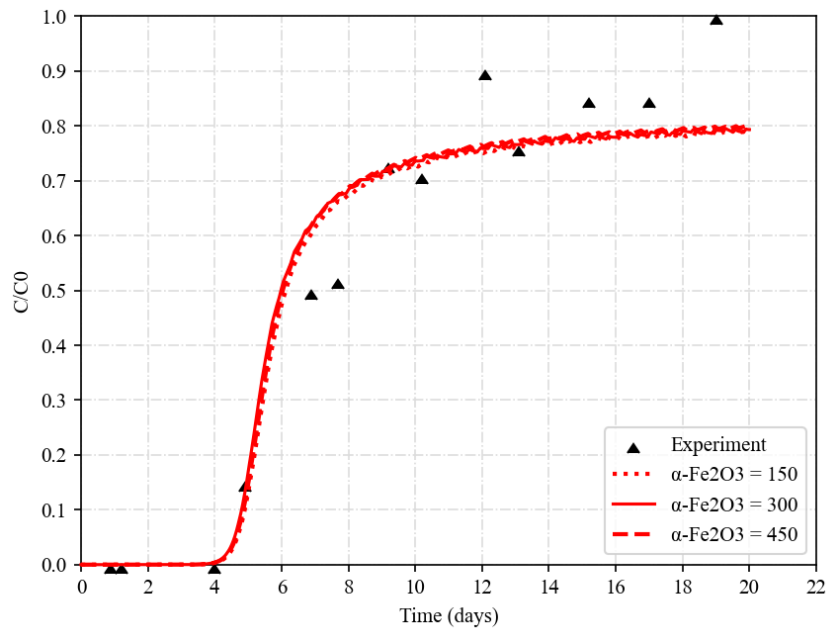


Figure 4.26 Change in  $C/C_0$  vs time graph of 25IR Column  $0.07 \text{ mL/cm}^2 \cdot \text{min}$  flux for Case 5 and Case 6 – 50% increase and decrease in  $\alpha - \text{Fe}_2\text{O}_3$

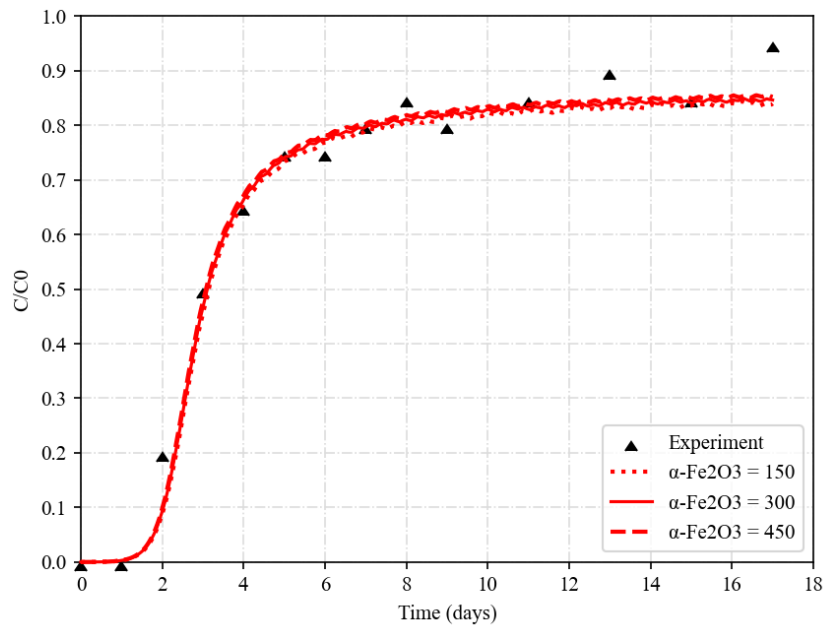


Figure 4.27 Change in  $C/C_0$  vs time graph of 25IR Column  $0.127 \text{ mL/cm}^2 \cdot \text{min}$  flux for Case 5 and Case 6 – 50% increase and decrease in  $\alpha - \text{Fe}_2\text{O}_3$

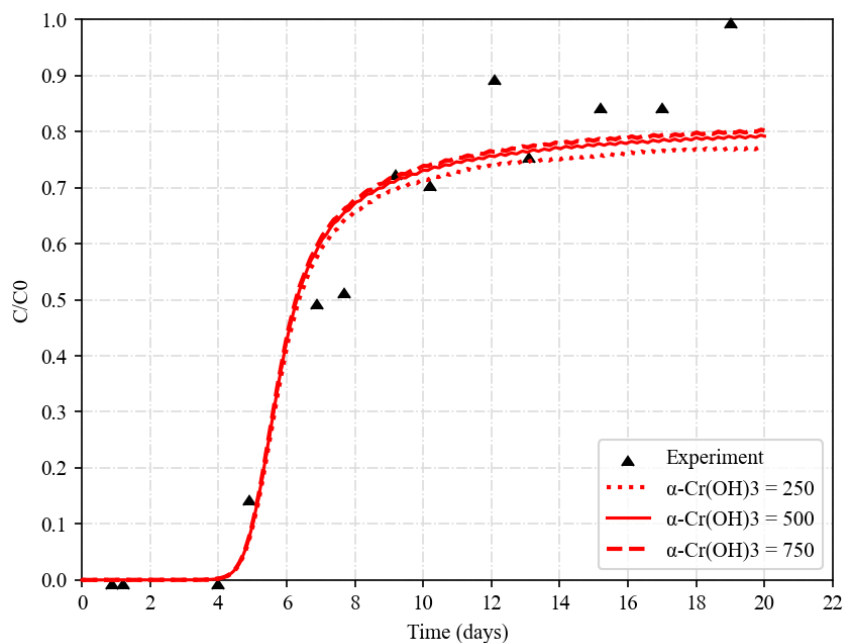


Figure 4.28 Change in  $C/C_0$  vs time graph of 25IR Column  $0.07 \text{ mL/cm}^2 \cdot \text{min}$  flux for Case 7 and Case 8 – 50% increase and decrease in  $\alpha - \text{Cr}(\text{OH})_3$

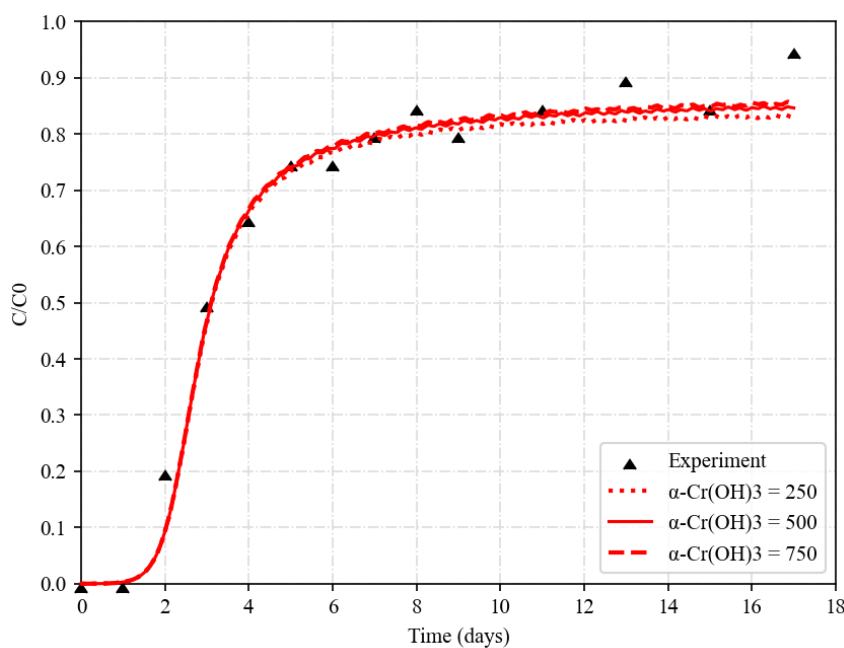


Figure 4.29 Change in  $C/C_0$  vs time graph of 25IR Column  $0.127 \text{ mL/cm}^2 \cdot \text{min}$  flux for Case 7 and Case 8 – 50% increase and decrease in  $\alpha - \text{Cr}(\text{OH})_3$

As Figure 4.22 and Figure 4.23 show when the rate constant,  $k$  is decreased by 50%, Cr(VI) is started to be detected at the effluent earlier and on the contrary when the rate constant is increased by 50%, Cr(VI) is started to be detected at the effluent later than the base case. This behavior also observed in 10IR Columns. This change in profiles is logical since, when the rate constant,  $k$  is decreased, the reduction rate will be decreased and Cr(VI) will be detected earlier at the effluent.

The change in  $C/C_0$  profiles with 50% increase and decrease in proportionality constants,  $\alpha$  for 25IR Column 0.07 and 0.127 mL/cm<sup>2</sup>.min fluxes are given in figures between Figure 4.24 and Figure 4.29. The change in  $C/C_0$  profiles show that the model is more sensitive to  $\alpha - \text{CaCO}_3$  than to other proportionality constants i.e.,  $\alpha - \text{Fe}_2\text{O}_3$ ,  $\alpha - \text{Cr}(\text{OH})_3$ . In fact, when the referred proportionality constants i.e.,  $\alpha - \text{Fe}_2\text{O}_3$ ,  $\alpha - \text{Cr}(\text{OH})_3$ , are increased and decreased by 50%, the  $C/C_0$  values do not change significantly at any time during the simulation.

Normalized parameter sensitivity values ( $S_P$ ) are calculated for rate constant,  $k$  and proportionality constant for minerals i.e.,  $\alpha - \text{CaCO}_3$ ,  $\alpha - \text{Fe}_2\text{O}_3$ ,  $\alpha - \text{Cr}(\text{OH})_3$ . For the rate constant,  $k$ , the calculated  $S_P$  indexes are given by Table 4.13 and Table 4.14. And the  $S_P$  indexes for the  $\alpha - \text{CaCO}_3$ ,  $\alpha - \text{Fe}_2\text{O}_3$ ,  $\alpha - \text{Cr}(\text{OH})_3$  are given between Table 4.15 and Table 4.20.

Table 4.13 Normalized Parameter Sensitivity Index Calculation for 25IR Column-0.07 ml/cm<sup>2</sup>-min flux : Case 1 and 2

Parameter	Base Case Value (P)	Perturbation in Parameter Value (P+ΔP)	P/ΔP	Base Case Model Output - C/C0 C <sub>P</sub>	Time (day)	Model Output (Case 1 and 2) C <sub>P+ΔP</sub>	Normalized Parameter Sensitivity (S <sub>P</sub> )		
Rate Constant, k (L/m <sup>2</sup> .s)	2.11×10 <sup>-4</sup>	3.17×10 <sup>-4</sup> Case 1	2	0.15	at day 5	0.00	-2.00		
				0.50	at day 6	0.10	-1.60		
				0.68	at day 8	0.60	-0.24		
				0.72	at day 10	0.68	-0.11		
				0.75	at day 12	0.72	-0.08		
				0.78	at day 15	0.74	-0.10		
				0.15	at day 5	0.61	6.13		
	1.06×10 <sup>-4</sup> Case 2	2	0.50	at day 6	0.70	0.80			
			0.68	at day 8	0.76	0.24			
			0.72	at day 10	0.79	0.19			
			0.75	at day 12	0.80	0.13			
			0.78	at day 15	0.83	0.13			
			<b>Sum of S<sub>P</sub></b>						<b>3.50</b>

Table 4.14 Normalized Parameter Sensitivity Index Calculation for 25IR Column - 0.127 ml/cm<sup>2</sup>.min flux : Case 1 and 2

Parameter	Base Case Value (P)	Perturbation in Parameter Value (P+ΔP)	P/ΔP	Base Case Model Output - C/C0 C <sub>P</sub>	Time (day)	Model Output (Case 1 and 2) C <sub>P+ΔP</sub>	Normalized Parameter Sensitivity (S <sub>P</sub> )		
Rate Constant, k (L/m <sup>2</sup> .s)	6.30×10 <sup>-5</sup>	9.45×10 <sup>-5</sup> Case 1	2	0.10	at day 2	0.00	-2.00		
				0.68	at day 4	0.60	-0.24		
				0.78	at day 6	0.72	-0.15		
				0.81	at day 8	0.78	-0.07		
				0.83	at day 12	0.81	-0.05		
				0.85	at day 14	0.82	-0.07		
				0.10	at day 2	0.50	8.00		
	3.15×10 <sup>-5</sup> Case 2	2	0.68	at day 4	0.75	0.21			
			0.78	at day 6	0.82	0.10			
			0.81	at day 8	0.83	0.05			
			0.83	at day 12	0.86	0.07			
			0.85	at day 14	0.88	0.07			
			<b>Sum of S<sub>P</sub></b>						<b>5.92</b>

Table 4.15 Normalized Parameter Sensitivity Index Calculation for 25IR Column-0.07 ml/cm<sup>2</sup>.min flux : Case 3 and 4

Parameter	Base Case Value (P)	Perturbation in Parameter Value (P+ΔP)	P/ΔP	Base Case Model Output - C/C0 C <sub>P</sub>	Time (day)	Model Output (Case) C <sub>P+ΔP</sub>	Normalized Parameter Sensitivity (S <sub>P</sub> )			
Proportinality constant, α - CaCO <sub>3</sub>	300	450 Case 3	2	0.15	at day 5	0.62	6.27			
				0.50	at day 6	0.70	0.80			
				0.68	at day 8	0.75	0.21			
				0.72	at day 10	0.76	0.11			
				0.75	at day 12	0.78	0.08			
				0.78	at day 15	0.79	0.03			
	150 Case 4	2	0.15	at day 5	0.00	-2.00				
			0.50	at day 6	0.00	-2.00				
			0.68	at day 8	0.07	-1.79				
			0.72	at day 10	0.47	-0.69				
			0.75	at day 12	0.62	-0.35				
			0.78	at day 15	0.72	-0.15				
			<b>Sum of S<sub>P</sub></b>							<b>0.50</b>

Table 4.16 Normalized Parameter Sensitivity Index Calculation for 25IR Column-0.127 ml/cm<sup>2</sup>.min flux: Case 3 and 4

Parameter	Base Case Value (P)	Perturbation in Parameter Value (P+ΔP)	P/ΔP	Base Case Model Output - C/C0 C <sub>P</sub>	Time (day)	Model Output (Case) C <sub>P+ΔP</sub>	Normalized Parameter Sensitivity (S <sub>P</sub> )			
Proportionality constant, α - CaCO <sub>3</sub>	300	450 Case 3	2	0.10	at day 2	0.40	6.00			
				0.68	at day 4	0.78	0.29			
				0.78	at day 6	0.81	0.08			
				0.81	at day 8	0.82	0.02			
				0.83	at day 12	0.83	0.00			
				0.85	at day 14	0.85	0.00			
				0.10	at day 2	0.00	-2.00			
				0.68	at day 4	0.20	-1.41			
	150 Case 4	2	0.78	at day 6	0.58	-0.51				
			0.81	at day 8	0.70	-0.27				
			0.83	at day 12	0.80	-0.07				
			0.85	at day 14	0.81	-0.09				
			<b>Sum of S<sub>P</sub></b>							<b>2.03</b>

Table 4.17 Normalized Parameter Sensitivity Index Calculation for 25IR Column-0.07 ml/cm<sup>2</sup>.min flux: Case 5 and 6

Parameter	Base Case Value (P)	Perturbation in Parameter Value (P+ΔP)	P/ΔP	Base Case Model Output - C/C <sub>0</sub> C <sub>P</sub>	Time (day)	Model Output (Case) C <sub>P+AP</sub>	Normalized Parameter Sensitivity (S <sub>P</sub> )			
Proportionality constant, α - Fe <sub>2</sub> O <sub>3</sub>	300	450 Case 5	2	0.15	at day 5	0.15	0.00			
				0.50	at day 6	0.50	0.00			
				0.68	at day 8	0.68	0.00			
				0.72	at day 10	0.72	0.00			
				0.75	at day 12	0.75	0.00			
				0.78	at day 15	0.78	0.00			
				0.15	at day 5	0.15	0.00			
	150 Case 6	2	0.50	at day 6	0.50	0.00				
			0.68	at day 8	0.68	0.00				
			0.72	at day 10	0.72	0.00				
			0.75	at day 12	0.75	0.00				
			0.78	at day 15	0.78	0.00				
			<b>Sum of S<sub>P</sub></b>							<b>0.00</b>

Table 4.18 Normalized Parameter Sensitivity Index Calculation for 25IR Column-0.127 ml/cm<sup>2</sup>.min flux:Case 5 and 6

Parameter	Base Case Value (P)	Perturbation in Parameter Value (P+ΔP)	P/ΔP	Base Case Model Output - C/C0 C <sub>P</sub>	Time (day)	Model Output (Case) C <sub>P+ΔP</sub>	Normalized Parameter Sensitivity (S <sub>P</sub> )
Proportionality constant, α - Fe <sub>2</sub> O <sub>3</sub>	300	450 Case 5	2	0.10	at day 2	0.10	0.00
				0.68	at day 4	0.68	0.00
				0.78	at day 6	0.78	0.00
				0.81	at day 8	0.81	0.00
				0.83	at day 12	0.83	0.00
				0.85	at day 14	0.85	0.00
	300	150 Case 6	2	0.10	at day 2	0.10	0.00
				0.68	at day 4	0.68	0.00
				0.78	at day 6	0.78	0.00
				0.81	at day 8	0.81	0.00
				0.83	at day 12	0.83	0.00
				0.85	at day 14	0.85	0.00
<b>Sum of S<sub>P</sub></b>							<b>0.00</b>

Table 4.19 Normalized Parameter Sensitivity Index Calculation for 25JR Column-0.07 ml/cm<sup>2</sup>.min flux: Case 7 and 8

Parameter	Base Case Value (P)	Perturbation in Parameter Value (P+ΔP)	P/ΔP	Base Case Model Output - C/C0 Cp	Time (day)	Model Output (Case) Cp+ΔP	Normalized Parameter Sensitivity (Sp)		
Proportionality constant, α - Cr(OH) <sub>3</sub>	500	750 Case 7	2	0.15	at day 5	0.15	0.00		
				0.50	at day 6	0.50	0.00		
				0.68	at day 8	0.68	0.00		
				0.72	at day 10	0.73	0.03		
				0.75	at day 12	0.76	0.03		
				0.78	at day 15	0.79	0.03		
				0.15	at day 5	0.15	0.00		
	250 Case 8	2	0.50	at day 6	0.50	0.00			
			0.68	at day 8	0.67	-0.03			
			0.72	at day 10	0.70	-0.06			
			0.75	at day 12	0.74	-0.03			
			0.78	at day 15	0.75	-0.08			
			<b>Sum of Sp</b>						<b>-0.11</b>

Table 4.20 Normalized Parameter Sensitivity Index Calculation for 25IR Column-0.07 ml/cm<sup>2</sup>.min flux: Case 7 and 8

Parameter	Base Case Value (P)	Perturbation in Parameter Value (P+ΔP)	P/ΔP	Base Case Model Output - C/C0 C <sub>P</sub>	Time (day)	Model Output (Case) C <sub>P+ΔP</sub>	Normalized Parameter Sensitivity (S <sub>P</sub> )		
Proportionality constant, α - Cr(OH) <sub>3</sub>	500	750 Case 7	2	0.10	at day 2	0.10	0.00		
				0.68	at day 4	0.68	0.00		
				0.78	at day 6	0.78	0.00		
				0.81	at day 8	0.81	0.00		
				0.83	at day 12	0.84	0.02		
				0.85	at day 14	0.86	0.02		
				0.10	at day 2	0.10	0.00		
	250 Case 8	2	0.68	at day 4	0.68	0.00			
			0.78	at day 6	0.78	0.00			
			0.81	at day 8	0.80	-0.02			
			0.83	at day 12	0.82	-0.02			
			0.85	at day 14	0.84	-0.02			
			<b>Sum of S<sub>P</sub></b>						<b>-0.02</b>

Normalized parameter sensitivity values ( $S_P$ ) are calculated for rate constant,  $k$  and proportionality constant for minerals i.e.,  $\alpha - \text{CaCO}_3$ ,  $\alpha - \text{Fe}_2\text{O}_3$ ,  $\alpha - \text{Cr}(\text{OH})_3$ . Table 4.21 summarizes the  $S_P$  indexes for each of the columns.

Table 4.21 Absolute  $S_P$  values of the rate constant,  $k$  and proportionality constant,  $\alpha - \text{CaCO}_3$ ,  $\alpha - \text{Fe}_2\text{O}_3$ ,  $\alpha - \text{Cr}(\text{OH})_3$  for 25IR Columns with 0.07 and 0.127 mL/cm<sup>2</sup>.min fluxes

Parameter	25IR 0.07 mL/cm <sup>2</sup> .min - $S_P$	25IR 0.127 mL/cm <sup>2</sup> .min - $S_P$
Rate Constant, $k$ (L/m <sup>2</sup> .s)	3.50	5.92
Proportionality Constant, $\alpha - \text{CaCO}_3$	0.50	2.03
Proportionality Constant, $\alpha - \text{Fe}_2\text{O}_3$	0.00	0.00
Proportionality Constant, $\alpha - \text{Cr}(\text{OH})_3$	0.11	0.02

As shown in Table 4.21, the  $S_P$  values for the rate constant parameter are higher than that of proportionality constants. In this regard, one can say that for the 25IR Columns the model is more sensitive to rate constant,  $k$  parameter than it is with proportionality constants. And among the proportionality constants, the model is more sensitive to  $\alpha - \text{CaCO}_3$ .

### 4.3.3 Sensitivity Analysis for 50IR Column

Similar approach is followed for sensitivity analysis with 50IR Column. With 50IR Columns, there are 3 proportionality constant,  $\alpha$  values:  $\alpha - \text{CaCO}_3$ ,  $\alpha - \text{Fe}_2\text{O}_3$  and  $\alpha - \text{Cr}(\text{OH})_3$ . In this regard, there are 4 cases other than the base case. The referred cases are given by Table 4.22 below. The change in  $C/C_0$  profiles can be seen between Figure 4.30 and Figure 4.33.

Table 4.22 The values of input parameters for each case of sensitivity analysis with 50IR Column 0.127 mL/cm<sup>2</sup>.min flux

	<b>Input Parameter</b>	<b>50IR 0.127 mL/cm<sup>2</sup>.min Flux</b>
<b>Base Case</b>	Rate Constant, k (L/m <sup>2</sup> .s )	5.38×10 <sup>-5</sup>
	α – CaCO <sub>3</sub>	100
	α – Fe <sub>2</sub> O <sub>3</sub>	100
	α – Cr(OH) <sub>3</sub>	200
<b>Case 1</b>	Rate Constant, k (L/m <sup>2</sup> .s )	8.08×10 <sup>-5</sup>
	α – CaCO <sub>3</sub>	100
	α – Fe <sub>2</sub> O <sub>3</sub>	100
	α – Cr(OH) <sub>3</sub>	200
<b>Case 2</b>	Rate Constant, k (L/m <sup>2</sup> .s)	2.69×10 <sup>-5</sup>
	α – CaCO <sub>3</sub>	100
	α – Fe <sub>2</sub> O <sub>3</sub>	100
	α – Cr(OH) <sub>3</sub>	200
<b>Case 3</b>	Rate Constant, k (L/m <sup>2</sup> .s)	5.38×10 <sup>-5</sup>
	α – CaCO <sub>3</sub>	150
	α – Fe <sub>2</sub> O <sub>3</sub>	100
	α – Cr(OH) <sub>3</sub>	200
<b>Case 4</b>	Rate Constant, k (L/m <sup>2</sup> .s)	5.38×10 <sup>-5</sup>
	α – CaCO <sub>3</sub>	50
	α – Fe <sub>2</sub> O <sub>3</sub>	100
	α – Cr(OH) <sub>3</sub>	200
<b>Case 5</b>	Rate Constant, k (L/m <sup>2</sup> .s)	5.38×10 <sup>-5</sup>
	α – CaCO <sub>3</sub>	100
	α – Fe <sub>2</sub> O <sub>3</sub>	150

**Table 4.22 (Continued)**

	<b>Input Parameter</b>	<b>50IR 0.127 mL/cm<sup>2</sup>.min Flux</b>
<b>Case 5</b>	$\alpha - \text{Cr(OH)}_3$	200
	Rate Constant, k (L/m <sup>2</sup> .s)	$5.38 \times 10^{-5}$
<b>Case 6</b>	$\alpha - \text{CaCO}_3$	100
	$\alpha - \text{Fe}_2\text{O}_3$	50
	$\alpha - \text{Cr(OH)}_3$	200
	Rate Constant, k (L/m <sup>2</sup> .s)	$5.38 \times 10^{-5}$
<b>Case 7</b>	$\alpha - \text{CaCO}_3$	100
	$\alpha - \text{Fe}_2\text{O}_3$	100
	$\alpha - \text{Cr(OH)}_3$	300
	Rate Constant, k (L/m <sup>2</sup> .s)	$5.38 \times 10^{-5}$
<b>Case 8</b>	$\alpha - \text{CaCO}_3$	100
	$\alpha - \text{Fe}_2\text{O}_3$	100
	$\alpha - \text{Cr(OH)}_3$	100

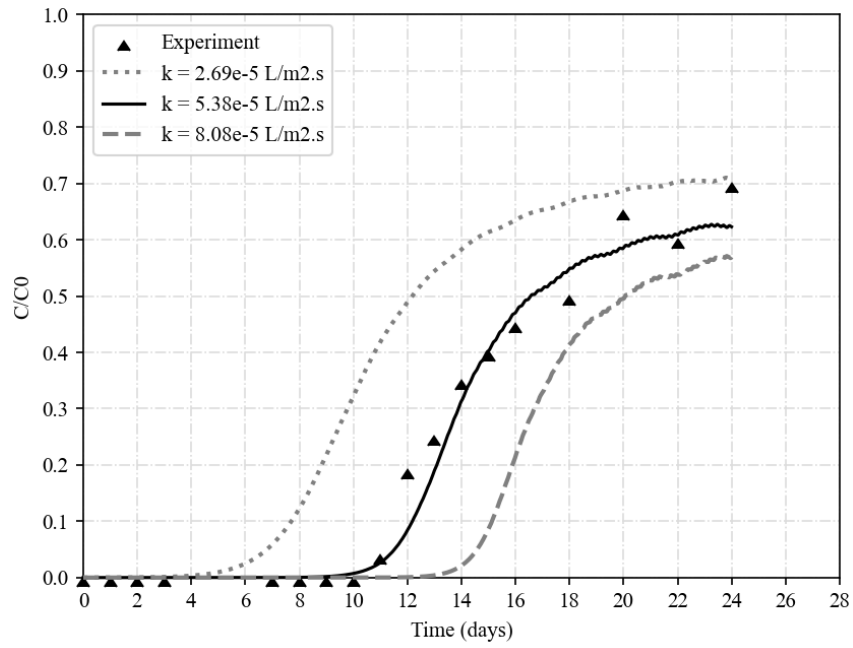


Figure 4.30 Change in  $C/C_0$  vs time graph of 50IR Column  $0.127 \text{ mL/cm}^2.\text{min}$  flux for Case 1 and Case 2 – 50% increase and decrease in rate constant,  $k$

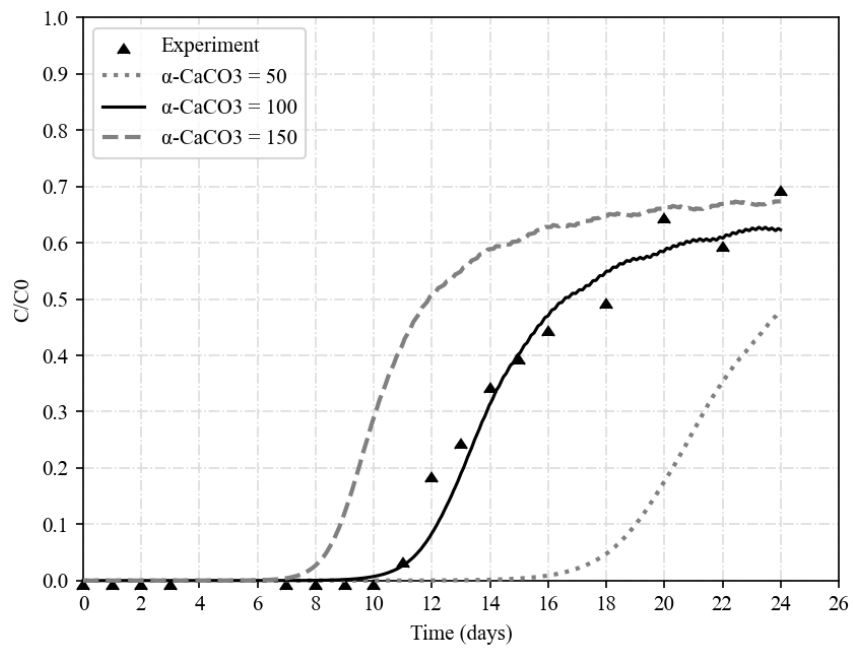


Figure 4.31 Change in  $C/C_0$  vs time graph of 50IR Column  $0.127 \text{ mL/cm}^2.\text{min}$  flux for Case 3 and Case 4 – 50% increase and decrease in  $\alpha - \text{CaCO}_3$

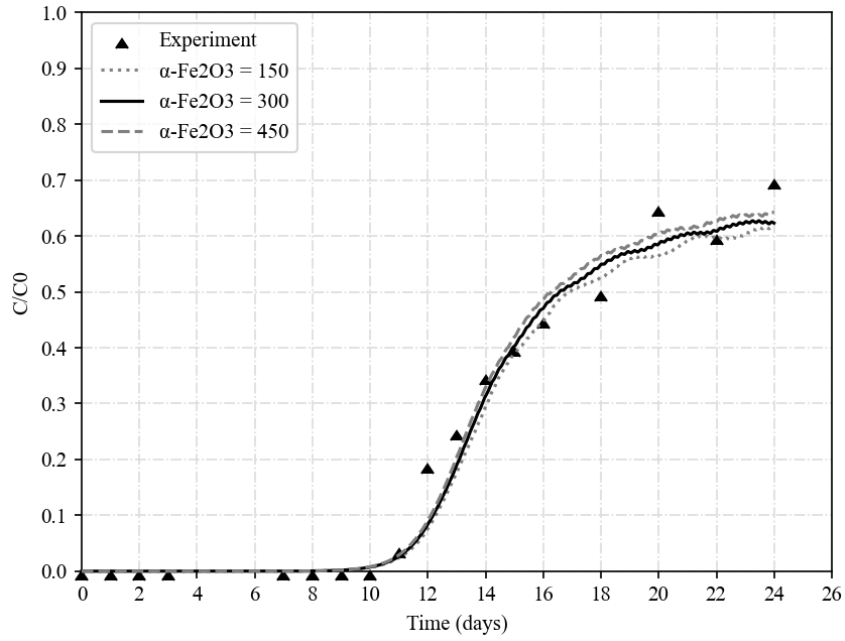


Figure 4.32 Change in  $C/C_0$  vs time graph of 50IR Column  $0.127 \text{ mL/cm}^2 \cdot \text{min}$  flux for Case 5 and Case 6 – 50% increase and decrease in  $\alpha - \text{Fe}_2\text{O}_3$

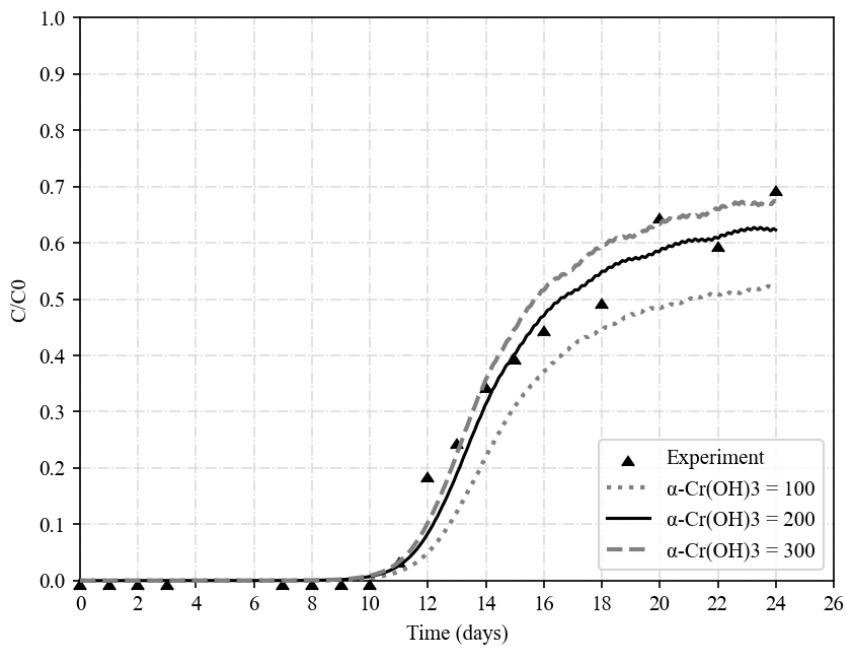


Figure 4.33 Change in  $C/C_0$  vs time graph of 50IR Column  $0.127 \text{ mL/cm}^2 \cdot \text{min}$  flux for Case 7 and Case 8 – 50% increase and decrease in  $\alpha - \text{Cr(OH)}_3$

As shown in Figure 4.30, when the rate constant,  $k$  is decreased by 50%, Cr(VI) is started to be detected at the effluent earlier and on the contrary when the rate constant is increased by 50%, Cr(VI) is started to be detected at the effluent later than the base case. This behavior also observed in other columns. The change in  $C/C_0$  profiles for the proportionality constants show that the model is more sensitive to  $\alpha - \text{CaCO}_3$  than to other proportionality constants. Compared to 25IR Columns, the perturbations in parameter  $\alpha - \text{Cr}(\text{OH})_3$  resulted in more deviations with 50IR Columns.

Normalized parameter sensitivity values ( $S_P$ ) are calculated for rate constant,  $k$  and proportionality constant for minerals i.e.,  $\alpha - \text{CaCO}_3$ ,  $\alpha - \text{Fe}_2\text{O}_3$ ,  $\alpha - \text{Cr}(\text{OH})_3$ . For the rate constant,  $k$ , the calculated  $S_P$  indexes are given by Table 4.23. And the  $S_P$  indexes for the  $\alpha - \text{CaCO}_3$ ,  $\alpha - \text{Fe}_2\text{O}_3$ ,  $\alpha - \text{Cr}(\text{OH})_3$  are given between Table 4.24 and Table 4.26.

Table 4.23 Normalized Parameter Sensitivity Index Calculation for 50IR Column-0.127 ml/cm<sup>2</sup>.min flux: Case 1 and 2

Parameter	Base Case Value (P)	Perturbation in Parameter Value (P+ΔP)	P/ΔP	Base Case Model Output - C/C0 Cp	Time (day)	Model Output (Case 1 and 2) Cp+ΔP	Normalized Parameter Sensitivity (Sp)
Rate Constant, k (L/m <sup>2</sup> .s)	5.38×10 <sup>-5</sup>	8.08×10 <sup>-5</sup> Case 1	2	0.02	at day 10	0.00	-2.00
				0.08	at day 12	0.60	13.00
				0.30	at day 14	0.72	2.80
				0.48	at day 16	0.78	1.25
				0.55	at day 18	0.81	0.95
				0.58	at day 20	0.82	0.83
	5.38×10 <sup>-5</sup>	2.69×10 <sup>-5</sup> Case 2	2	0.02	at day 10	0.50	48.00
				0.08	at day 12	0.75	16.75
				0.30	at day 14	0.82	3.47
				0.48	at day 16	0.83	1.46
				0.55	at day 18	0.86	1.13
				0.58	at day 20	0.88	1.03
<b>Sum of Sp</b>						<b>86.66</b>	

Table 4.24 Normalized Parameter Sensitivity Index Calculation for 50IR Column-0.127 ml/cm<sup>2</sup>.min flux: Case 3 and 4

Parameter	Base Case Value (P)	Perturbation in Parameter Value (P+ΔP)	P/ΔP	Base Case Model Output - C/C0 C <sub>P</sub>	Time (day)	Model Output (Case 3 and 4) C <sub>P+ΔP</sub>	Normalized Parameter Sensitivity (SP)
Proportionality constant, α - CaCO <sub>3</sub>	100	150 Case 3	2	0.02	at day 10	0.00	-2.00
				0.08	at day 12	0.50	10.50
				0.30	at day 14	0.58	1.87
				0.48	at day 16	0.62	0.58
				0.55	at day 18	0.65	0.36
				0.58	at day 20	0.67	0.31
	50 Case 4	2	0.02	at day 10	0.00	-2.00	
			0.08	at day 12	0.00	-2.00	
			0.30	at day 14	0.00	-2.00	
			0.48	at day 16	0.02	-1.92	
			0.55	at day 18	0.06	-1.78	
			0.58	at day 20	0.20	-1.31	
<b>Sum of SP</b>							<b>0.62</b>

Table 4.25 Normalized Parameter Sensitivity Index Calculation for 50IR Column with 0.127 ml/cm<sup>2</sup>.min flux:Case 5 and 6

Parameter	Base Case Value (P)	Perturbation in Parameter Value (P+ΔP)	P/ΔP	Base Case Model Output - C/C0 C <sub>P</sub>	Time (day)	Model Output (Case 5 and 6) C <sub>P+ΔP</sub>	Normalized Parameter Sensitivity (S <sub>P</sub> )
Proportionality constant, α - Fe <sub>2</sub> O <sub>3</sub>	300	450 Case 5	2	0.02	at day 10	0.02	0.00
				0.08	at day 12	0.08	0.00
				0.30	at day 14	0.30	0.00
				0.48	at day 16	0.50	0.08
				0.55	at day 18	0.56	0.04
				0.58	at day 20	0.60	0.07
		150 Case 6	2	0.02	at day 10	0.02	0.00
				0.08	at day 12	0.08	0.00
				0.30	at day 14	0.30	0.00
				0.48	at day 16	0.47	-0.04
				0.55	at day 18	0.53	-0.07
				0.58	at day 20	0.56	-0.07
<b>Sum of S<sub>P</sub></b>							<b>0.01</b>

Table 4.26 Normalized Parameter Sensitivity Index Calculation for 50IR Column-0.127 ml/cm<sup>2</sup>.min flux: Case 7 and 8

Parameter	Base Case Value (P)	Perturbation in Parameter Value (P+ΔP)	P/ΔP	Base Case Model Output - C/C0 Cp	Time (day)	Model Output (Case 7 and 8) Cp+ΔP	Normalized Parameter Sensitivity (Sp)
Proportionality constant, α - Cr(OH) <sub>3</sub>	200	300 Case 7	2	0.02	at day 10	0.02	0.00
				0.08	at day 12	0.10	0.50
				0.30	at day 14	0.33	0.20
				0.48	at day 16	0.52	0.17
				0.55	at day 18	0.60	0.18
	100 Case 8	2	0.58	at day 20	0.63	0.17	
			0.02	at day 10	0.02	0.00	
			0.08	at day 12	0.06	-0.50	
			0.30	at day 14	0.20	-0.67	
			0.48	at day 16	0.38	-0.42	
				0.55	at day 18	0.45	-0.36
				0.58	at day 20	0.48	-0.34
<b>Sum of Sp</b>						<b>-1.07</b>	

Normalized parameter sensitivity values ( $S_P$ ) are calculated for rate constant,  $k$  and proportionality constant for minerals i.e.,  $\alpha - \text{CaCO}_3$ ,  $\alpha - \text{Fe}_2\text{O}_3$ ,  $\alpha - \text{Cr}(\text{OH})_3$ . Table 4.27 summarizes the  $S_P$  indexes for each of the columns.

Table 4.27 Absolute  $S_P$  values of the rate constant,  $k$  and proportionality constant,  $\alpha - \text{CaCO}_3$ ,  $\alpha - \text{Fe}_2\text{O}_3$ ,  $\alpha - \text{Cr}(\text{OH})_3$  for 50IR Column with 0.127 mL/cm<sup>2</sup>.min flux

<b>Parameter</b>	<b>50IR 0.127 mL/cm<sup>2</sup>.min - <math>S_P</math></b>
Rate Constant, $k$ (L/m <sup>2</sup> .s)	86.66
Proportionality Constant, $\alpha - \text{CaCO}_3$	0.62
Proportionality Constant, $\alpha - \text{Fe}_2\text{O}_3$	0.01
Proportionality Constant, $\alpha - \text{Cr}(\text{OH})_3$	1.07

As shown in Table 4.27,  $S_P$  index calculated for the rate constant,  $k$  parameter is higher than that of other parameters. In this regard, one can say that the model is more sensitive to rate constant,  $k$  parameter than it is with other parameters. And among the proportionality constants, the model is more sensitive to  $\alpha - \text{Cr}(\text{OH})_3$  parameter.

Overall, the 10IR, 25IR and 50IR models are assessed in terms of sensitivity to input parameters which are rate constant,  $k$  and the proportionality constants. Normalized parameter sensitivity values ( $S_P$ ) are calculated for each input parameter and compared. In Table 4.28, the  $S_P$  indexes calculated for the referred input parameters are shown.

Table 4.28 Absolute  $S_P$  values of the rate constant,  $k$  and proportionality constant,  $\alpha$  -  $\text{CaCO}_3$ ,  $\alpha$  -  $\text{Fe}_2\text{O}_3$ ,  $\alpha$  -  $\text{Cr}(\text{OH})_3$  for 10IR, 25IR and 50IR Columns

Parameter	Sp Index 10IR 0.07 Flux	Sp Index 10IR 0.127 Flux	Sp Index 25IR 0.07 Flux	Sp Index 25IR 0.127 Flux	Sp Index 50IR 0.127 Flux
Rate Constant, $k$ ( $\text{L}/\text{m}^2.\text{s}$ )	2.30	0.25	3.50	5.92	86.66
Proportionality constant, $\alpha$ - $\text{CaCO}_3$	5.71	0.33	0.5	2.03	0.62
Proportionality constant, $\alpha$ - $\text{Fe}_2\text{O}_3$			0.00	0.00	0.01
Proportionality constant, $\alpha$ - $\text{Cr}(\text{OH})_3$			0.11	0.02	1.07

Higher the value of  $S_P$ , the greater the sensitivity of the model for that parameter. As Table 4.28 shows with 10IR Columns, the model is more sensitive to  $\alpha$  -  $\text{CaCO}_3$  parameter than it is with rate constant,  $k$ . With 25IR Columns, the model is more sensitive to rate constant,  $k$  parameter than it is with proportionality constants. And among the proportionality constants, the 25IR Columns' models are more sensitive to  $\alpha$  -  $\text{CaCO}_3$ . In case of 50IR Column, the model is more sensitive to rate constant,  $k$  parameter than it is with other parameters. And among the proportionality constants, the model is more sensitive to  $\alpha$  -  $\text{Cr}(\text{OH})_3$  parameter. This indicates that, when the reactive media amount is increased, the model will be more depended on the rate constant,  $k$  parameter than it is with proportionality constants.

#### **4.4 Predictions for Removal Performance under Different Inlet Cr(VI) Loadings**

In the experimental study conducted by Uyuşur (2006), the inlet Cr(VI) concentration was 20 mg/L and this was kept constant through different experimental setups. The calibrated models, on the other hand, can also be used for prediction purposes. Therefore the calibrated models of 25IR Column with 0.07 and 0.127 mL/cm<sup>2</sup>.min flux and 50IR Column with 0.127 mL/cm<sup>2</sup>.min flux experiments are also run with different inlet Cr(VI) concentrations i.e., 50 mg/L and 100 mg/L to predict the column performances under increased Cr loadings. The change in removal performance is then illustrated by C/C<sub>0</sub> vs time graphs for three cases: (i) Inlet Cr(VI) Concentration of 20 mg/L; (ii) Inlet Cr(VI) Concentration of 50 mg/L; (iii) Inlet Cr(VI) Concentration of 100 mg/L.

Other than the Cr(VI) removal performance, the change in reactive media amounts and the change in secondary mineral amounts and their effect on reactivity are assessed as a result of increases in the inlet Cr(VI) loadings.

##### **4.4.1 Model Predictions under Different Cr(VI) Loads**

The model prediction results for 25IR Column with 0.07 and 0.127 mL/cm<sup>2</sup>.min fluxes for 20, 50 and 100 mg/L inlet Cr(VI) loadings are given in Figure 4.34 and Figure 4.35.

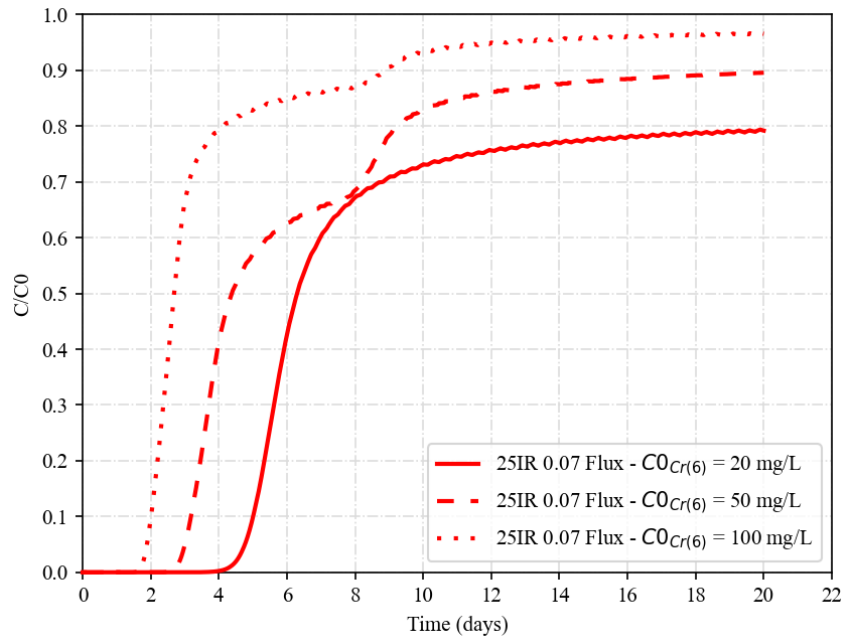


Figure 4.34 C/C0 versus time graphs for 25IR Column with 0.07 mL/cm<sup>2</sup>.min fluxes with inlet Cr(VI) Concentrations of 20, 50 and 100 mg/L

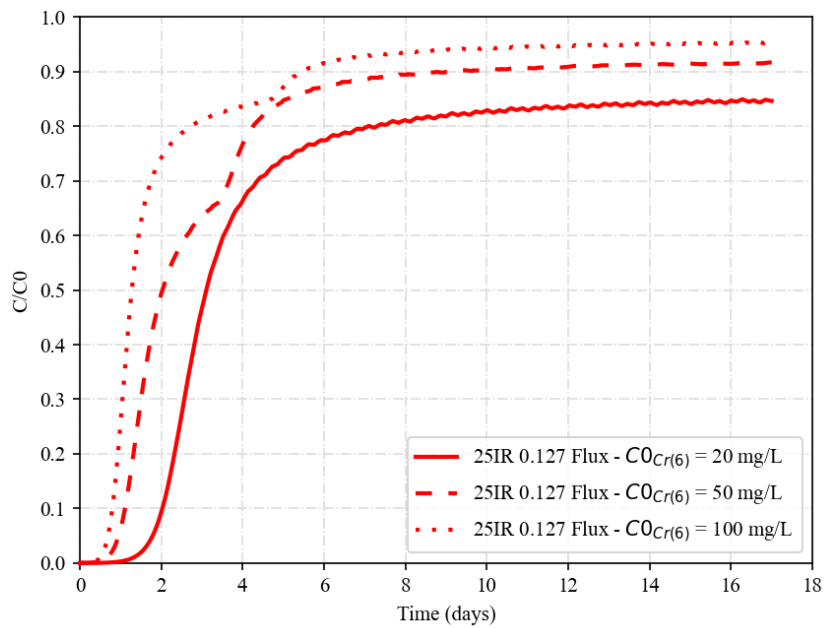


Figure 4.35 C/C0 versus time graphs for 25IR Column with 0.127 mL/cm<sup>2</sup>.min fluxes with inlet Cr(VI) Concentrations of 20, 50 and 100 mg/L

With the increase in inlet Cr(VI) concentrations, the exhaustion of the columns occurs earlier, as expected. With 25IR Column  $0.07 \text{ mL/cm}^2\cdot\text{min}$  flux, within the first 4 days i.e., almost 72 Pore Volumes (PVs) of Cr(VI) is remediated. Afterwards, the columns starts to be exhausted and by the 20<sup>th</sup> day i.e., 358 PVs, of the simulation,  $C/C_0$  value reaches to 0.8. When the Cr(VI) concentration is increased to 50 mg/L, Cr(VI) is remediated almost within 3 days which corresponds to 54 PVs and by the 20<sup>th</sup> day, the  $C/C_0$  value reaches to 0.9 which is a higher value compared to case where inlet Cr(VI) concentration was 20 mg/L. With 100 mg/L Cr(VI) load, the removal performance is more negatively affected. In this case, Cr(VI) remediation lasts for 2 days i.e., 36 PVs and by the 20<sup>th</sup> day of the simulation, the  $C/C_0$  value reaches to 0.97.

In this regard, one can say that 25IR Column –  $0.07 \text{ mL/cm}^2\cdot\text{min}$  flux which embodies 0.124 moles of reactive media i.e., ZVI, can remediate a plume volume with Cr(VI) concentrations of 20, 50 and 100 mg/L for 4, 3 and 2 days (72, 54 and 36 PVs), respectively.

With 25IR Column  $0.127 \text{ mL/cm}^2\cdot\text{min}$  flux, the reactive media amount is again 0.124 moles, however, the operating flowrate is higher. In this case, the exhaustion of the column starts at times even earlier than that of 25IR Column with lower –  $0.07 \text{ mL/cm}^2\cdot\text{min}$  flux. For inlet Cr(VI) concentration of 20 mg/L, Cr(VI) is remediated for almost 2 days i.e., 46 PVs. With 100 mg/L of Cr(VI) concentration, within half a day i.e., 12 PVs, Cr(VI) is remediated and afterwards, the exhaustion starts. Hence, 25IR Column –  $0.127 \text{ mL/cm}^2\cdot\text{min}$  flux which embodies 0.124 moles of reactive media i.e., ZVI, can remediate a plume volume with Cr(VI) concentration of 20, 50 and 100 mg/L for 2, 1 and 0.5 days (46, 23 and 12 PVs), respectively.

The model prediction results for 50IR Column with  $0.127 \text{ mL/cm}^2\cdot\text{min}$  flux for 20, 50 and 100 mg/L inlet Cr concentrations is given in Figure 4.36.

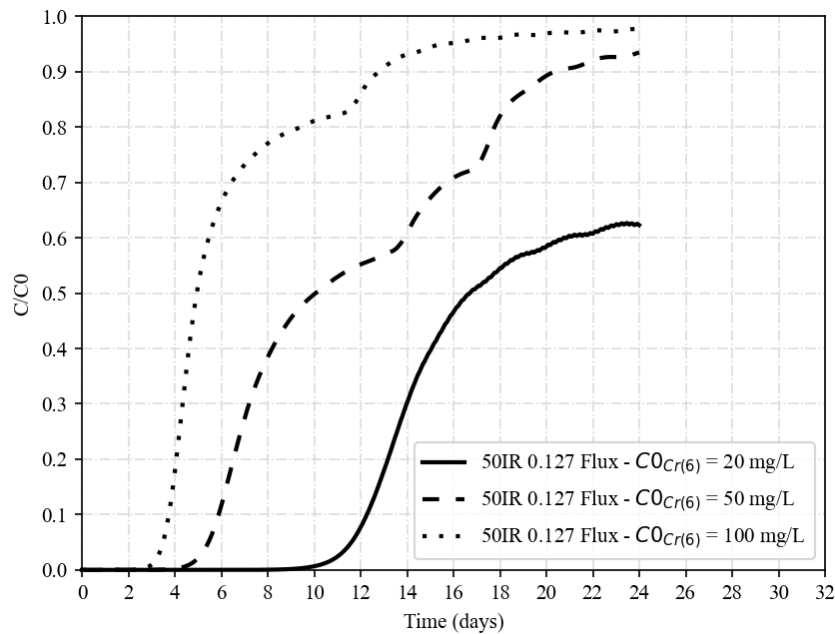


Figure 4.36 C/C0 versus time graphs for 50IR Column with 0.127 mL/cm<sup>2</sup>.min fluxes with inlet Cr(VI) Concentrations of 20, 50 and 100 mg/L

As Figure 4.36 shows, when 50 IR column is used to remove 20 mg/L of inlet Cr(VI) load, the remediation lasts for 10 days i.e., 173 PVs and by the 24<sup>th</sup> day (416 PVs) of the simulation C/C0 reaches to 0.6 i.e., by the 24<sup>th</sup> day only 40% of the inlet Cr(VI) concentration is remediated. When the inlet Cr(VI) load is increased to 50 mg/L, the complete Cr(VI) reduction lasts for almost 4 days i.e., 69 PVs and as expected the final C/C0 value is 0.92 by the 24<sup>th</sup> day of the simulation. With inlet Cr(VI) load of 100 mg/L, the complete Cr(VI) reduction lasts for almost 2.5 days i.e., 43 PVs. Therefore, with 50IR Column - 0.127 mL/cm<sup>2</sup>.min flux which embodies 0.267 moles of reactive media i.e., ZVI, can remediate a plume volume with Cr(VI) concentration of 20, 50 and 100 mg/L for 10, 4 and 2.5 days (173, 69 and 43 PVs), respectively. These model predictions thus depict the difference between the two column operations when treating the same pollution levels with different reactive media amounts.

The model prediction results are summarized in Table 4.29 in terms of remediated PVs. The decrease in remediated PVs show that with the increase in inlet Cr(VI)

concentration from 20 mg/L to 100 mg/L, the remediated PVs decreases exponentially.

Table 4.29 Model Prediction Results for 25IR 0.07 and 0.127 mL/cm<sup>2</sup>.min and 50IR 0.127 mL/cm<sup>2</sup>.min fluxes

Column ID	Scenario	Description of the Scenario	Remediated PVs
25IR 0.07 mL/cm <sup>2</sup> .min	Base Case	Inlet Cr(VI) Conc = 20 mg/L	72
	Case 1	Inlet Cr(VI) Conc = 50 mg/L	54
	Case 2	Inlet Cr(VI) Conc = 100 mg/L	36
25IR 0.127 mL/cm <sup>2</sup> .min	Base Case	Inlet Cr(VI) Conc = 20 mg/L	46
	Case 1	Inlet Cr(VI) Conc = 50 mg/L	23
	Case 2	Inlet Cr(VI) Conc = 100 mg/L	12
50IR 0.127 mL/cm <sup>2</sup> .min	Base Case	Inlet Cr(VI) Conc = 20 mg/L	173
	Case 1	Inlet Cr(VI) Conc = 50 mg/L	69
	Case 2	Inlet Cr(VI) Conc = 100 mg/L	43

#### 4.4.2 Model Predictions for ZVI Amount and Surface Area under Different Cr(VI) Loads

The model predictions for the change in ZVI amount and reactive surface area with 50IR Column – 0.127 mL/cm<sup>2</sup>.min flux are given in Figure 4.37 and Figure 4.38.

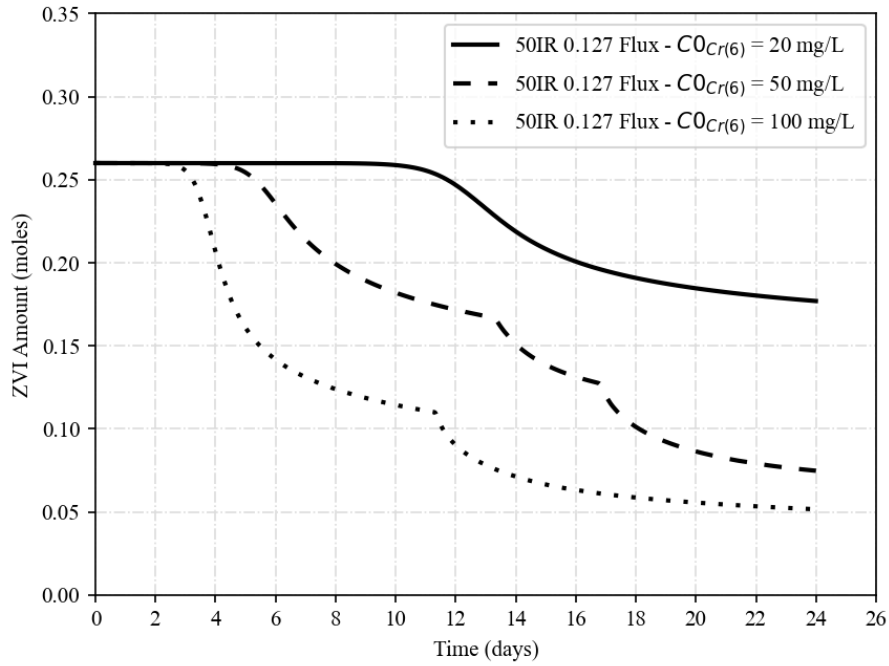


Figure 4.37 ZVI amount versus time for 50IR Column – 0.127 mL/cm<sup>2</sup>.min flux with inlet Cr(VI) concentrations of 20, 50 and 100 mg/L

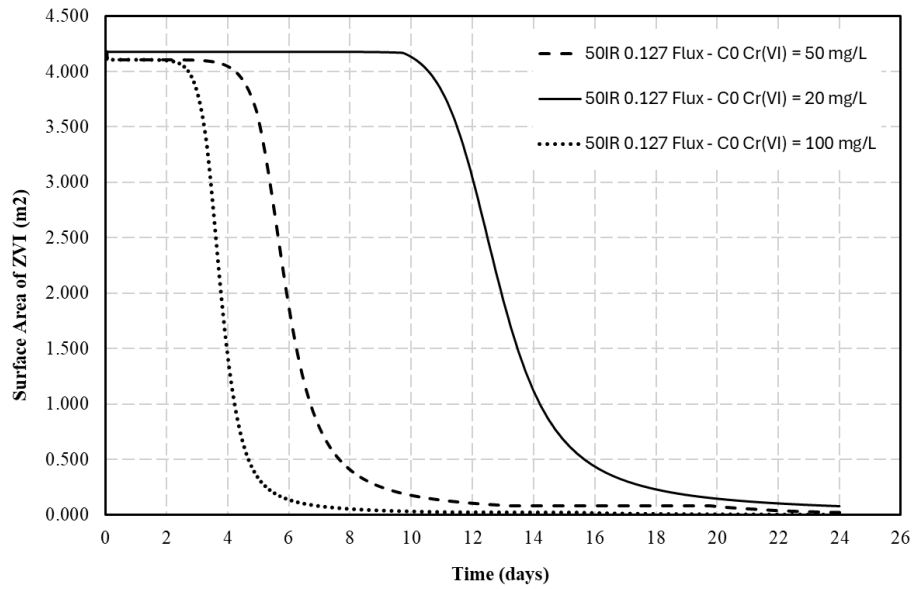


Figure 4.38 ZVI reactive surface area versus time for 50IR Column – 0.127 mL/cm<sup>2</sup>.min flux with inlet Cr(VI) concentrations of 20, 50 and 100 mg/L

The comparative model simulations illustrate that when the pollution level in the influent solution increases, the reactive media amount decreases in larger amounts within the same time period. As can be seen from Figure 4.37, with 20 mg/L of inlet Cr(VI) concentration, the ZVI amount decreases by 33% for 24 days and when the inlet Cr(VI) concentration increases to 100 mg/L, the decrease is by 81% within the same time period.

Figure 4.37 shows that at the end of simulation i.e., day 24, there is still ZVI left in the system. However, as shown in Figure 4.38, the reactive surface area of ZVI is already exhausted by the minerals and becomes almost zero at the end of the simulation. In parallel to  $C/C_0$  vs time graph i.e., Figure 4.36, for 10 days, the surface area of ZVI is constant and afterward it starts to decrease in case where inlet Cr(VI) concentration is 20 mg/L as shown in Figure 4.38. When the inlet Cr(VI) concentration is increased to 50 mg/L, the exhaustion starts on day 4 of the simulation and at day 12, the reactive surface area is decreased by almost 100%. For the case where the inlet Cr(VI) concentration is increased to 100 mg/L, the exhaustion starts on day 2 of the simulation and by day 6, the reactive surface area is decreased by almost 100%. For all cases, at the end of simulation, the reactive surface area is exhausted by almost 100% as shown in Figure 4.38. When the cases are evaluated for the same time period i.e. 10 days, it can be seen that the decrease is larger in case where the inlet Cr(VI) concentration is the highest i.e., 100 mg/L.

#### **4.4.3 Model Predictions for Secondary Mineral Precipitation and Minerals' Effect on Reactivity**

In previous sections, model predictions for  $C/C_0$  versus time, reactive media amount and reactive surface area are represented. As stated under Section 3.3.1, the changing iron reactivity resulting from mineral accumulation can be estimated using an empirically established correlation between reactivity and secondary mineral deposition as expressed in the equation below (Jeen et al., 2007).

$$S(x, t) = S_0 \times \exp\left(-\sum_i \alpha_i \varphi_i(x, t)\right)$$

(Eqn 20)

where,  $S(x,t)$  and  $S_0$  are the current and initial reactive surface area of the ZVI,  $\alpha_i$  is the proportionality constant of the mineral phase  $i$ ,  $\varphi_i(x,t)$  is the amount of the mineral  $i$ ,  $x$  and  $t$  represents location and time, respectively (Jeen et al., 2007).

The exponential term embodied in the equation shows the effect of minerals on the reactive surface area of ZVI. As mentioned earlier, there are three minerals taken into account: (i)  $\text{CaCO}_3$  (ii)  $\text{Fe}_2\text{O}_3$  (iii)  $\text{Cr}(\text{OH})_3$ . The referred exponential functions associated with the three minerals are as follows. As one can see  $\text{Exp term1}$ ,  $\text{Exp term2}$  and  $\text{Exp term3}$  represents the effect of  $\text{Fe}_2\text{O}_3$ ,  $\text{CaCO}_3$  and  $\text{Cr}(\text{OH})_3$ , respectively.

$$\text{Exp term1} = \exp\left(-\sum \alpha_{\text{Fe}_2\text{O}_3} \varphi_{\text{Fe}_2\text{O}_3}(x, t)\right)$$

(Eqn 21)

$$\text{Exp term2} = \exp\left(-\sum \alpha_{\text{CaCO}_3} \varphi_{\text{CaCO}_3}(x, t)\right)$$

(Eqn 22)

$$\text{Exp term3} = \exp\left(-\sum \alpha_{\text{Cr}(\text{OH})_3} \varphi_{\text{Cr}(\text{OH})_3}(x, t)\right)$$

(Eqn 23)

The model predictions for the mineral concentrations and the exponential terms of the referred minerals for 50IR Column – 0.127 mL/cm<sup>2</sup>.min flux with inlet Cr(VI) concentration of 50 mg/L are given Figure 4.39 and Figure 4.40, respectively.

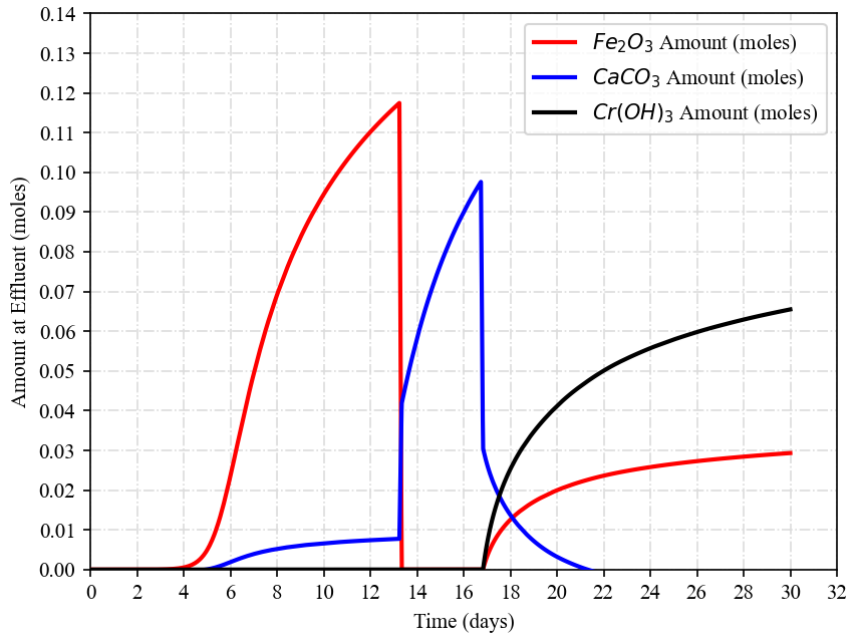


Figure 4.39 Effluent mineral amounts versus time for 50IR – 0.127 mL/cm<sup>2</sup>.min flux with 50 mg/L inlet Cr(VI) concentration

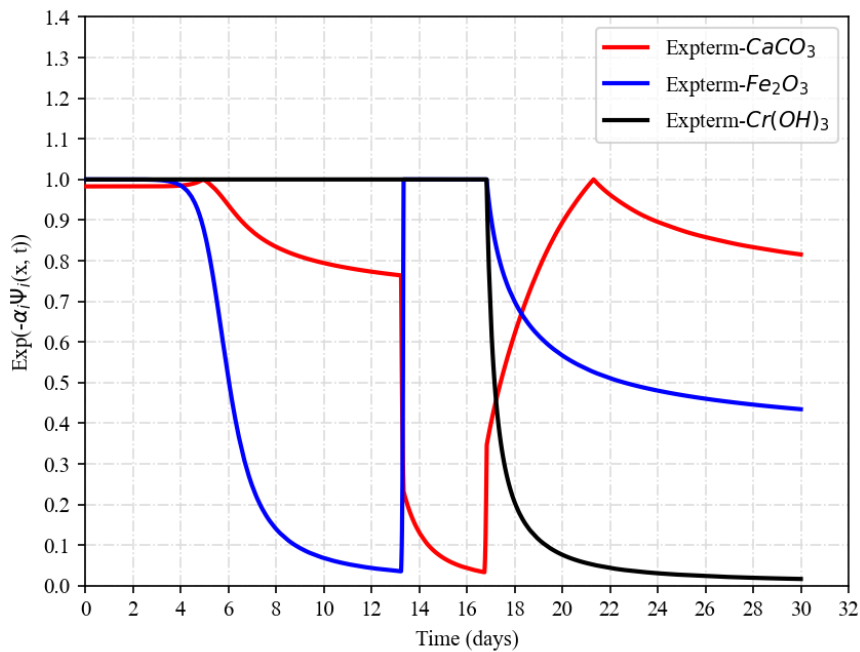


Figure 4.40 Exponential function values versus time for three minerals with for 50IR – 0.127 mL/cm<sup>2</sup>.min flux with 50 mg/L inlet Cr(VI) concentration

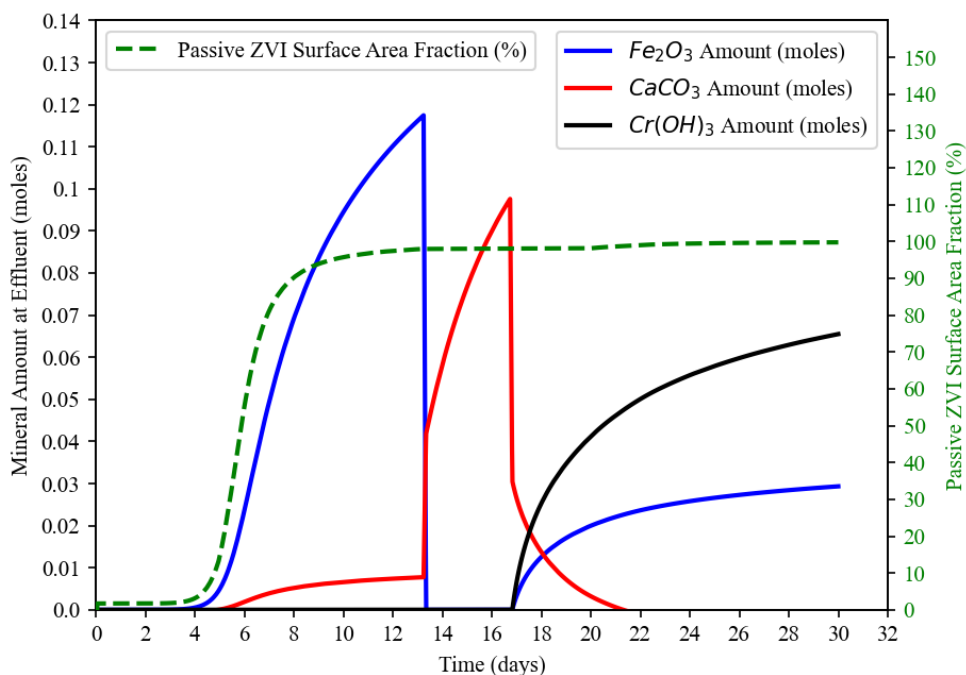


Figure 4.41 Passive ZVI Surface Area Fraction and Mineral Amount at the Effluent with respect to time for 50IR – 0.127 mL/cm<sup>2</sup>.min flux with 50 mg/L inlet Cr(VI) concentration

Figure 4.39 shows that the amounts of Fe<sub>2</sub>O<sub>3</sub> and CaCO<sub>3</sub> at the effluent end of the column start to increase at day 4 of the simulation and for the mineral Cr(OH)<sub>3</sub>, the increase starts after day 17 of the simulation. As shown in Figure 4.40, the impact of the exponential functions associated with the Fe<sub>2</sub>O<sub>3</sub> and CaCO<sub>3</sub> minerals are zero until day 4 of the simulation. As there are no Fe<sub>2</sub>O<sub>3</sub> and CaCO<sub>3</sub> minerals at the effluent end until day 4, thus, exponential functions returns the value of 1. For the Cr(OH)<sub>3</sub> mineral, similarly, the exponential function takes the value of 1 for 17 days and changes accordingly pertaining to its precipitation. As the mineral concentrations increase, the exponential function value i.e., exp (-x), decreases in an amount associated with the proportionality constant and the mineral amount. Thus the decrease in exponential function leads to the decrease in reduction rate of Cr(VI). Figure 4.41 shows the fraction of ZVI that passivated and the amount of three minerals at the effluent for 50IR 0.127 mL/cm<sup>2</sup>.min flux Column with 50 mg/L of

inlet Cr(VI) concentration. It can be inferred from Figure 4.41 that with the increase in mineral amounts the reactive surface is started to be passivated and at the end of simulation, the reactive area is passivated completely. When the mineral amounts are compared in Figure 4.41, one can see that mineral  $\text{Fe}_2\text{O}_3$  has shown the most profound effect between days 4 to 13. Figure 4.40 also shows that the exponential term associated with mineral  $\text{Fe}_2\text{O}_3$  decreases more drastically between days 4 and 13 compared to other minerals' exponential term.

It should be mentioned that the reactions associated with these minerals are in equilibrium. When the product of the concentrations of the ions (Q) in solution is higher than solubility product ( $K_{sp}$ ) of mineral i, the solution becomes super saturated in terms of mineral i and it precipitates. So the abundance of the ions plays an important role in precipitation and dissolution reactions (Flowers et al., 2019).

The pH and alkalinity of the system are two important factors in mineral precipitation behaviors. For example, the process of  $\text{CaCO}_3$  precipitation is influenced by the concentrations of its sub-ions i.e.,  $\text{Ca}^{2+}$  and  $\text{CO}_3^{2-}$ , and these ions are pH-dependent. At low pH conditions, there is an excess  $\text{H}^+$  ions and these  $\text{H}^+$  ions react with  $\text{CO}_3^{2-}$  to form carbonic acid ( $\text{H}_2\text{CO}_3$ ) which dissociates into bicarbonate ions ( $\text{HCO}_3^-$ ) and water. In this regard, under low pH values,  $\text{CaCO}_3$  is less likely to precipitate. On the other hand, under alkaline conditions i.e., high pH, there is an excess  $\text{OH}^-$  ions and the presence of these ions increases the concentration of  $\text{CO}_3^{2-}$  ions and eventually,  $\text{CaCO}_3$  formation is promoted. In this regard,  $\text{CaCO}_3$  is more likely to precipitate under alkaline conditions (Flowers et al., 2019).

In case of  $\text{Fe}_2\text{O}_3$ , the precipitation process is more complex compared to  $\text{CaCO}_3$ . Also the abundance of the Fe in the system affects the overall precipitation behavior. In terms of pH, at low pH values i.e.,  $\text{pH} < 4$ ,  $\text{Fe}^{3+}$  remains soluble and the precipitation of  $\text{Fe}_2\text{O}_3$  is unlikely. At pH values between 4 and 6, iron hydroxides ( $\text{Fe}(\text{OH})_3$ ) starts to precipitate. And above pH value of 7, the formed iron hydroxides can further dehydrate to form  $\text{Fe}_2\text{O}_3$  (Flowers et al., 2019). Similarly the solubility of

$\text{Cr}(\text{OH})_3$  mineral depends on pH. In short, at high pH conditions, the precipitation of the mineral is more likely on the contrary to low pH conditions (Flowers et al., 2019).

One can say that in terms of pH conditions, the minerals i.e.,  $\text{CaCO}_3$ ,  $\text{Fe}_2\text{O}_3$  and  $\text{Cr}(\text{OH})_3$  favor alkaline conditions. Figure 4.39 shows that after day 4,  $\text{Fe}_2\text{O}_3$  concentration increases until almost day 13 and afterward, it sharply decreases. When the ZVI amount is checked it can be seen that after day 10 the ZVI amount decreases. This sharp decrease in  $\text{Fe}_2\text{O}_3$  can be associated to the ZVI availability. While the  $\text{Fe}_2\text{O}_3$  concentration shows a sharp decrease at day 13, the  $\text{CaCO}_3$  mineral concentration increases, where along with the elimination of  $\text{Fe}^{3+}$  ions, the  $\text{OH}^-$  ions present in the solution can favor the formation of  $\text{CaCO}_3$  precipitates.

Overall, with the model prediction runs, the change in removal performance, the change in reactive media amount and its reactive surface area and the amount of minerals and their effect of the reactivity under different inlet Cr(VI) concentrations are discussed in this section. For the removal performance, the model predictions show that with the increase in inlet Cr(VI) concentration, the exhaustion of the columns starts earlier which means that remediation of Cr(VI) lasts for a shorter time period. The difference in reactive media amount is also showed. While with 25IR Column -  $0.127 \text{ mL/cm}^2 \cdot \text{min}$  flux can reduce Cr(VI) for 1 day (46 PVs) in case the inlet load is increased to 50 mg/L, 50IR Column with  $0.127 \text{ mL/cm}^2 \cdot \text{min}$  flux can reduce Cr(VI) for 4 (69 PVs) days when inlet Cr(VI) concentration is increased to 50 mg/L.

The changes in the amounts of reactive media and its reactive surface area are parallel to  $C/C_0$  vs time graphs in a way that at the time when the surface area (or the amount) of the reactive media starts to decrease, Cr(VI) starts to be detected in the effluent. Also it is observed that when the pollution level in the influent solution increases, the reactive media amount decreases in larger amounts within the same time period. With 20 mg/L of inlet Cr(VI) concentration, the ZVI amount decreases by 33% for 24 days and when the inlet Cr(VI) concentration increases to 100 mg/L, the decrease is by 81% within the same time period. Although the ZVI amount versus

time graphs show that at the end of simulation, there is still ZVI in the system, the reactive surface area of ZVI becomes zero at the end of the simulations due to the surface passivation by secondary mineral formations.

The mineral precipitation and the effect of the formed minerals on the ZVI reactivity are also assessed for the case of 50IR Column - 0.127 mL/cm<sup>2</sup>.min flux with 50 mg/L inlet Cr(VI) concentration simulation demonstrations. The mineral formations are evaluated in terms of pH and consequently alkalinity. It is concluded that all these minerals i.e., CaCO<sub>3</sub>, Fe<sub>2</sub>O<sub>3</sub> and Cr(OH)<sub>3</sub> favor alkaline conditions, where Fe<sub>2</sub>O<sub>3</sub> mineral formation is also affected by the presence of ZVI in the system. The change in mineral amounts with respect to time is assessed in terms of pH and ion abundance in the system. The modelling efforts presented in this study provide insights on important geochemical processes affecting Cr removal by ZVI; and is expected to shed light in modeling Cr reduction by ZVI, such as permeable reactive wall applications in the field.

The limitations associated with modeling tool Phreeq-C are listed under Section 3.2. It should be mentioned that these limitations can affect the performance of the model when it is used for field scale applications. In case that the flow conditions in a heterogeneous aquifer would require 2D or 3D spatial resolution, then . Phreeq-C can be integrated with other hydrological and transport models such as MODFLOW and HYDRUS (Parkhurst, 1995). It should also be noted that in field scale environments, the parameters related to geochemical reaction network processes such as kinetic rate constants are often uncertain and might show variations within the system boundaries, where these uncertainties might lead to significant errors in predictions (Parkhurst, 1995). Another limitation is that as the number of species in the solutions i.e., groundwater in case of real world systems, reactions and time step increases, the computation time grows significantly with Phreeq-C. Because, in field scale applications, the model problem may require a more fine grid systems i.e., smaller time steps, and in this regard model can take a long time to run and computational demand of the modeling tool might be significant for field scale applications (Parkhurst, 1995).

It should be mentioned that the influent and background solution compositions in this model work are not as complex as real world systems. And this model work is case specific to the referred lab scale study by Uyusur (2006). Therefore, if the models presented in this study are to be considered to be used for field scale applications, some modifications may need to be done. These modifications might include as the coupling Phreeq-C with other hydrological and transport models, using adaptive time step techniques, focusing on only key geochemical species and/or simplifying the model as much as possible. In this regard, Phreeq-C facilitates the design and optimization of field-scale solutions in the following manners (Parkhurst & Appelo, 2013; Appelo & Postma, 2005).

- The processes involved in heavy metal elimination include precipitation, adsorption/surface complexation, and reduction to a less hazardous state. These processes can be simulated using Phreeq-C. In this context, Phreeq-C serves as a geochemical modeling tool that can forecast the sequence of events resulting in metal removal in PRB systems. This will provide the modeler with insight into the main reaction routes for the elimination of heavy metals (Appelo & Postma, 2005).
- Reactive material selection may be conducted based on major reaction pathways. Additionally, by understanding chemical pathways, the modeler can ascertain the formation of harmful byproducts (Appelo & Postma, 2005)
- Anticipating responses facilitates the formulation of PRBs to sustain optimal pH and redox conditions, for instance, by the incorporation of buffering agents or electron donors/acceptors. Comprehending response sequences guarantees that PRB design accommodates the requisite reaction zones (Appelo & Postma, 2005).
- Reaction predictions guarantee that the barrier design considers material deterioration or depletion, facilitating effective replacement schedules or alternative material selections (Appelo & Postma, 2005).
- Sequential reactions may result in the emergence of secondary pollutants, and forecasting these reactions facilitates the integration of secondary treatment

zones or supplementary reactive materials to mitigate these consequences (Appelo & Postma, 2005).

- Breakthrough curves derived from Phreeq-C can guide PRB design by evaluating the PRB lifespan, finding reactive medium thickness, and projecting maintenance requirements (Parkhurst & Appelo, 2013).

In general, geochemical modeling tools can provide useful information related to the geochemical processes that takes place at the field and the design of the field-scale solutions can be optimized accordingly. The model predictions presented in this section show the effect of different Cr(VI) loadings on the remediated PV amount, which might be helpful to determine . the reactive media thickness and PRB lifespan, for modeling Cr(VI) removal performance by PRB –based implementations.

## CHAPTER 5

### CONCLUSION AND FUTURE WORKS

#### 5.1 Conclusions

In this study, a kinetic reaction network is developed for Cr(VI) reduction to Cr(III) by ZVI, where the impacts of Fe(0) depletion and passivisation of reactive media with secondary mineral precipitation during the removal process are incorporated. Sensitivity analysis of the key kinetic input parameters of the model is also conducted to basically assess the effect of different input parameters on the removal process. And finally, to see the impact of different inlet Cr(VI) concentrations on removal performance, reactive media amount, and mineral formations, model predictions are presented.

The proposed reaction network for the removal process consists of aqueous speciation reactions, mineral dissolution and precipitation reactions, and Cr(VI) reduction reaction. Among these reaction groups only Cr(VI) reduction is controlled kinetically. Other reactions are assumed to be in equilibrium. Reactive transport of Cr(VI) removal by ZVI are simulated for the column experiments carried out by Uyuşur (2006) and Uyuşur and Ünlü (2009); considering varying groundwater fluxes (0.07 and 0.127 mL/cm<sup>2</sup>.min) and ZVI concentrations (10%, 25% and 50% iron powder – corresponding to 10IR, 25IR and 50IR columns, respectively).

The simulation results for each column are presented under Section 4.2. The fit quality between the model and the experimental data is measured with R<sup>2</sup> and MSE statistical analysis. The results of model calibration indicated a very good agreement between measured and predicted concentration values, and hence reasonably well calibration of the numerical reactive transport model was achieved.

The model results showed that the impact of  $\text{CaCO}_3$  and  $\text{Fe}_2\text{O}_3$  mineral precipitates observed to have equal effects on  $\text{Fe}(0)$  surface passivation for 25 and 50IR columns, whereas  $\text{Cr}(\text{OH})_3$  had a higher impact. According to Jeen et al. (2007) and Gui et al. (2009), a higher value of proportionality constant  $\alpha$  means that contribution to reactivity loss is higher. When the calibrated proportionality constants for the three minerals are compared among 10IR, 25IR and 50IR columns, the results show that the impact of ZVI surface passivation is reduced with increasing ZVI concentrations. Due to the higher amount of available  $\text{Fe}(0)$  surface with higher ZVI, the impact of secondary mineral precipitation becomes less pronounced, when the volume of secondary mineral precipitates are compared with the high ZVI volumes. When the decrease in the amounts of ZVI reactivity are compared among the columns, it can be concluded that 50IR Column provides the best remediation activity among the columns and the passivization of the reactive media due to mineral precipitation was not as effective as it was with 10IR and 25IR Columns. The numerical model simulations demonstrated that when the columns operate at higher flux conditions, exhaustion is reached earlier. Therefore, lower rate constant and higher proportionality constant,  $\alpha$ , for same mineral was needed for cases where the flowrates are higher during calibration process of the model.

The mineral distribution graphs of the columns i.e., mineral concentration versus distance along the column, show that mineral accumulation is most prominent near the inlet part of the column, with particularly high concentrations in  $\text{Fe}_2\text{O}_3$  mineral formations. This behavior is mainly due to the oxidation of  $\text{Fe}(0)$  to form  $\text{Fe}(\text{III})$  oxide precipitates; corresponding to the initial decrease in reactivity of ZVI at the influent end of the column. These results are consistent with the solid phase analysis of column experiments by Uyuşur (2006); Uyuşur and Ünlü (2009). The model simulation results show that the  $\text{Cr}(\text{OH})_3$  mineral has the lowest concentration among the three minerals, behaving in a pulse like behavior along the column, where it is mainly observed at the influent end of the columns. Comparative simulations of ZVI concentrations and reactive surface area predictions demonstrated the impact of surface passivation by the precipitation of secondary minerals including  $\text{CaCO}_3$ ,

Fe<sub>2</sub>O<sub>3</sub> and Cr(OH)<sub>3</sub>, despite the presence of ZVI throughout the column for Cr reduction.

The pH profile of the columns show that there is a slight pH increase along the column in 10IR Column. This pH increase can be associated with iron corrosion. In 25IR and 50 IR Columns firstly pH increases due to iron corrosion effect and then it drops corresponding to the formation of Cr(OH)<sub>3</sub> precipitates and along with CaCO<sub>3</sub> precipitation, the pH profile flattens due to the buffering effect. The initial increase in pH and then the carbonate bufferring effect has also been stated in previous works (Wanner et al.,2011; Jeen et al.,2007; Gui et al.,2009).

To identify the key input parameters in the model a sensitivity analysis is conducted. As a sensitivity analysis method one-at-a-time (OAT) technique is used. Analysis mainly performed to show how the model output deviates i.e., C/C<sub>0</sub> versus time profiles, when one specific model input parameter is increased or decreased by a certain amount while the other parameters are kept constant. The sensitivity of the model to a specific parameter is calculated by the Normalized Parameter Sensitivity (S<sub>p</sub>) index . According to S<sub>p</sub> values, with 10IR Columns, the model is more sensitive to  $\alpha$  - CaCO<sub>3</sub> parameter and with 25IR and 50IR Columns, the model is more sensitive to rate constant,k parameter. This shows that with the increase in amount of reactive media, the mineral precipitation effect is started to be diminished and the model is becoming more depended on the rate constant,k parameter.

The impact of different inlet Cr(VI) concentrations on removal performance, reactive media amount, and mineral formations are also discussed. Model predictions show that higher Cr(VI) concentrations shorten remediation time, as the columns become exhausted faster. It is found out that as the inlet Cr(VI) concentration increased from 20 mg/L to 100 mg/L, the remediated PVs decreases exponentially. The reduction in reactive media correlates with the appearance of Cr(VI) in the effluent, and higher pollution levels lead to faster depletion of reactive media. The variations in the amount of reactive media and its reactive surface area correspond to the C/C<sub>0</sub> vs. time graphs, such that when the surface area (or amount) of the reactive media begins

to decline, Cr(VI) starts appearing in the effluent. Additionally, it is observed that as the pollution level in the influent solution rises, the amount of reactive media decreases more rapidly within the same time frame.

The modelling efforts presented in this study provide insights on important geochemical processes affecting Cr removal by ZVI; and is expected to shed light in modeling Cr reduction by ZVI such as iron-based permeable reactive barrier applications in the field.

## **5.2 Future Works**

In this study, Cr(VI) removal process with ZVI is modeled. The calibrated input parameters i.e., rate constant,  $k$  and proportionality constants,  $\alpha$  for the minerals, are presented. Also a sensitivity analysis is conducted to show the key input parameters of the model. Model prediction runs are presented to see the impact of inlet Cr(VI) concentrations on removal performance, reactive media amount, and mineral formations.

The calibrated models can further be extended to be validated with a different set of data to see if the model is capable of simulating future behavior. In a further study, the model can be used to see the effect of variations in background and influent solution compositions. The groundwater bodies can include various species other than carbonate ions. In a further study more complex influent and background solution compositions can be run with calibrated models.

The modeling tool provide us the required amount of reactive media or it shows when the column starts to be exhausted for Cr removal applications. In this regard, the geochemical models can become a part of design process of PRBs, where the predictions can be conducted for various treatability scenarios and design in general.

It should be mentioned that the reactive media ZVI can also be used to treat other hazardous compounds. The kinetic modeling approach can provide an insight for modeling the removal for other heavy metal compounds residing in groundwater

bodies, where first the reaction network would need to be updated accordingly and calibration of the input parameters would need to be conducted.



## REFERENCES

- Alowitz, M. J., & Scherer, M. M. (2002, January 4). Kinetics of Nitrate, Nitrite, and Cr(VI) Reduction by Iron Metal. *Environmental Science & Technology*, 36(3), 299–306. <https://doi.org/10.1021/es011000h>
- Appelo, C., & Postma, D. (2005). *Geochemistry, Groundwater and Pollution, Second Edition*. CRC Press.
- Arora, B., Şengör, S. S., Spycher, N. F., & Steefel, C. I. (2014). A reactive transport benchmark on heavy metal cycling in lake sediments. *Computational Geosciences*, 19(3), 613–633. <https://doi.org/10.1007/s10596-014-9445-8>
- Battelle Memorial Institute. (2012). *Permeable reactive barrier cost and performance report*. <https://www.frtr.gov/matrix/documents/Permeable-Reactive-Barriers/2012-Permeable-Reactive-Barrier-Cost-and-Performance-Report.pdf>
- Becker, D. S., Long, E. R., Proctor, D. M., & Ginn, T. C. (2006). Evaluation of potential toxicity and bioavailability of chromium in sediments associated with chromite ore processing residue. *Environmental Toxicology and Chemistry*, 25(10), 2576–2583. <https://doi.org/10.1897/05-494r.1>
- Bilardi, S., Calabrò, P. S., & Moraci, N. (2023). A Review of the Hydraulic Performance of Permeable Reactive Barriers Based on Granular Zero Valent Iron. *Water*, 15(1), 200. <https://doi.org/10.3390/w15010200>
- Blowes, D. W., Ptacek, C. J., & Jambor, J. L. (1997, November 26). In-Situ Remediation of Cr(VI)-Contaminated Groundwater Using Permeable Reactive Walls: Laboratory Studies. *Environmental Science & Technology*, 31(12), 3348–3357. <https://doi.org/10.1021/es960844b>
- Chiha, M., Samar, M. H., & Hamdaoui, O. (2006, June). Extraction of chromium (VI) from sulphuric acid aqueous solutions by a liquid surfactant membrane (LSM). *Desalination*, 194(1–3), 69–80. <https://doi.org/10.1016/j.desal.2005.10.025>
- Chrysochoou, M., Theologou, E., Bompoti, N., Dermatas, D., & Panagiotakis, I. (2016, October 22). Occurrence, Origin and Transformation Processes of Geogenic Chromium in Soils and Sediments. *Current Pollution Reports*, 2(4), 224–235. <https://doi.org/10.1007/s40726-016-0044-2>
- EFSA. (2014). Scientific Opinion on the risks to public health related to the presence of chromium in food and drinking water. *EFSA Journal*, 12(3). <https://doi.org/10.2903/j.efsa.2014.3595>

- EU Parliament and the Council . (2020, December 23). Directive (EU) 2020/2184 of the European Parliament and of the Council of 16 December 2020 on the quality of water intended for human consumption. In *EUR-Lex*. Official Journal of the European Union. <http://data.europa.eu/eli/dir/2020/2184/oj>
- Fiúza, A., Silva, A., Carvalho, G., de la Fuente, A. V., & Delerue-Matos, C. (2010, March). Heterogeneous kinetics of the reduction of chromium (VI) by elemental iron. *Journal of Hazardous Materials*, *175*(1–3), 1042–1047. <https://doi.org/10.1016/j.jhazmat.2009.10.116>
- Flowers, P., Langely, R., Robinson, W. R., & Theopold, K. H. (2019). *Chemistry 2e*. OpenStax. [https://chem.libretexts.org/Bookshelves/General\\_Chemistry](https://chem.libretexts.org/Bookshelves/General_Chemistry)
- Gallios, G. P., & Vaclavikova, M. (2007, November 21). Removal of chromium (VI) from water streams: a thermodynamic study. *Environmental Chemistry Letters*, *6*(4), 235–240. <https://doi.org/10.1007/s10311-007-0128-8>
- Gheju, M. (2011, April 19). Hexavalent Chromium Reduction with Zero-Valent Iron (ZVI) in Aquatic Systems. *Water, Air, & Soil Pollution*, *222*(1–4), 103–148. <https://doi.org/10.1007/s11270-011-0812-y>
- Gould, J. (1982). The kinetics of hexavalent chromium reduction by metallic iron. *Water Research*, *16*(6), 871–877. [https://doi.org/10.1016/0043-1354\(82\)90016-1](https://doi.org/10.1016/0043-1354(82)90016-1)
- Gui, L., Yang, Y., Jeon, S. W., Gillham, R. W., & Blowes, D. W. (2009, April). Reduction of chromate by granular iron in the presence of dissolved CaCO<sub>3</sub>. *Applied Geochemistry*, *24*(4), 677–686. <https://doi.org/10.1016/j.apgeochem.2008.12.019>
- Hamby, D. M. (1994). A review of techniques for parameter sensitivity analysis of environmental models. *Environmental Monitoring and Assessment*, *32*(2), 135–154. <https://doi.org/10.1007/bf00547132>
- Holch. (2008, June). *Thermodynamic and kinetic degradation reactions of organic substances in groundwater modelled with phreeqc*. [https://www.hydrology.uni-freiburg.de/abschluss/Holch\\_J\\_2008\\_DA.pdf](https://www.hydrology.uni-freiburg.de/abschluss/Holch_J_2008_DA.pdf)
- Hyman, M., & Dupont, R. R. (2001, January 1). *Groundwater and Soil Remediation*. Amer Society of Civil Engineers. [http://books.google.ie/books?id=XzrkwAEACAAJ&dq=Groundwater+and+Soil+Remediation:+Process+Design+and+Cost+Estimating+of+Proven+Technologies&hl=&cd=1&source=gbs\\_api](http://books.google.ie/books?id=XzrkwAEACAAJ&dq=Groundwater+and+Soil+Remediation:+Process+Design+and+Cost+Estimating+of+Proven+Technologies&hl=&cd=1&source=gbs_api)

- Jeen, S., Mayer, K. U., Gillham, R. W., & Blowes, D. W. (2007). Reactive Transport Modeling of Trichloroethene Treatment with Declining Reactivity of Iron. *Environmental Science & Technology*, 41(4), 1432–1438. <https://doi.org/10.1021/es062490m>
- Kaplan, D. I., & Gilmore, T. J. (2004, June). Zero-Valent Iron Removal Rates of Aqueous Cr(VI) Measured Under Flow Conditions. *Water, Air, & Soil Pollution*, 155(1–4), 21–33. <https://doi.org/10.1023/b:wate.0000026518.23591.ac>
- Karegar, S., Bhargavi, M., & Divekar, S. V. (2015). Treatment of wastewater from chrome plating industry by ion exchange method. *International Journal of Research in Engineering and Technology*, 04(07), 393–401. <https://doi.org/10.15623/ijret.2015.0407063>
- Karvonen, A. (2004, August). Cation Effects on Chromium Removal in Permeable Reactive Walls. *Journal of Environmental Engineering*, 130(8), 863–866. [https://doi.org/10.1061/\(asce\)0733-9372\(2004\)130:8\(863\)](https://doi.org/10.1061/(asce)0733-9372(2004)130:8(863))
- Mayer, K.U., Blowes, D.W., Frind, E.O. (2001). Reactive transport modeling of an in situ reactive barrier for the treatment of hexavalent chromium and trichloroethylene in groundwater. *Water Resources Research*. 37(12), 3091-3103.
- Melitas, N., Chuffe-Moscoso, O., & Farrell, J. (2001). Kinetics of Soluble Chromium Removal from Contaminated Water by Zerovalent Iron Media: Corrosion Inhibition and Passive Oxide Effects. *Environmental Science & Technology*, 35(19), 3948–3953. <https://doi.org/10.1021/es001923x>
- Member Agencies of the Federal Remediation Technologies Roundtable. (2002). *Evaluation of Permeable Reactive Barrier Performance*. [https://www.clu-in.org/download/rtdf/2-prbperformance\\_web.pdf](https://www.clu-in.org/download/rtdf/2-prbperformance_web.pdf)
- Mersin Valiliği Çevre Şehircilik ve İklim Değişikliği İl Müdürlüğü. (2022). *Mersin İli 2021 Yılı Çevre Durum Raporu*. [https://webdosya.csb.gov.tr/db/ced/icerikler/mers-n\\_-cdr2021-20221227141341.pdf](https://webdosya.csb.gov.tr/db/ced/icerikler/mers-n_-cdr2021-20221227141341.pdf)
- MTA. (2022). Dünyada ve Türkiye’de Krom. *Maden Tetkik Ve Arama*. Retrieved February 18, 2024, from [https://www.mta.gov.tr/v3.0/sayfalar/bilgi-merkezi/maden-serisi/krom\\_1.pdf](https://www.mta.gov.tr/v3.0/sayfalar/bilgi-merkezi/maden-serisi/krom_1.pdf)
- Naidu, & Birke (Eds.). (2015). *Permeable Reactive Barrier Sustainable Groundwater Remediation*. CRC Press.

- Nordstrom, D. K. (Ed.). (2005). *Groundwater Geochemistry*.  
<https://doi.org/10.1007/b138774>
- Noubactep, C. (2010, November 16). Review: The fundamental mechanism of aqueous contaminant removal by metallic iron. *Water SA*, 36(5).  
<https://doi.org/10.4314/wsa.v36i5.62000>
- Noubactep, C., & Schöner, A. (2009, June 15). Fe<sub>0</sub>-based alloys for environmental remediation: Thinking outside the box. *Journal of Hazardous Materials*, 165(1–3), 1210–1214. <https://doi.org/10.1016/j.jhazmat.2008.09.084>
- Noubactep, C., & Schöner, A. (2010, March). Metallic iron for environmental remediation: Learning from electrocoagulation. *Journal of Hazardous Materials*, 175(1–3), 1075–1080.  
<https://doi.org/10.1016/j.jhazmat.2009.09.152>
- Obiri-Nyarko, F., Grajales-Mesa, S. J., & Malina, G. (2014, September). An overview of permeable reactive barriers for in situ sustainable groundwater remediation. *Chemosphere*, 111, 243–259.  
<https://doi.org/10.1016/j.chemosphere.2014.03.112>
- Palmer, C. D., & Wittbrodt, P. R. (1991, May). Processes affecting the remediation of chromium-contaminated sites. *Environmental Health Perspectives*, 92, 25–40. <https://doi.org/10.1289/ehp.919225>
- Parkhurst, D. L., & Appelo, C. a. J. (2013). *Description of Input and Examples for PHREEQC Version 3—A Computer Program for Speciation, Batch-Reaction, One-Dimensional Transport, and Inverse Geochemical Calculations*. <https://pubs.usgs.gov/tm/06/a43/>
- Parkhurst, D. L. (1995). *User's Guide to PHREEQC - A Computer Program for Speciation, Reaction-Path, Advective-Transport, and Inverse Geochemical Calculations*. U.S. Geological Survey.  
<https://pubs.usgs.gov/wri/1995/4227/report.pdf>
- Powell, Blowes, Gillham, Schultz, Sivavec, Puls, Vogan, Powell, & Landis. (1998). *Permeable Reactive Barrier Technologies for Contaminant Remediation*.  
[https://cfpub.epa.gov/si/si\\_public\\_record\\_Report.cfm?Lab=NRMRL&dirEntryId=90404](https://cfpub.epa.gov/si/si_public_record_Report.cfm?Lab=NRMRL&dirEntryId=90404)
- Prasad, S., Yadav, K. K., Kumar, S., Gupta, N., Cabral-Pinto, M. M., Rezanian, S., Radwan, N., & Alam, J. (2021). Chromium contamination and effect on environmental health and its remediation: A sustainable approaches. *Journal of Environmental Management*, 285, 112174.  
<https://doi.org/10.1016/j.jenvman.2021.112174>

- Pratt, A. R., Blowes, D. W., & Ptacek, C. J. (1997). Products of Chromate Reduction on Proposed Subsurface Remediation Material. *Environmental Science & Technology*, 31(9), 2492–2498. <https://doi.org/10.1021/es9607897>
- Profillidis, V., & Botzoris, G. (2019b). Statistical Methods for Transport Demand Modeling. In *Elsevier eBooks* (pp. 163–224). <https://doi.org/10.1016/b978-0-12-811513-8.00005-4>
- Scherer, M. M., Richter, S., Valentine, R. L., & Alvarez, P. J. J. (2000, January). Chemistry and Microbiology of Permeable Reactive Barriers for In Situ Groundwater Clean up. *Critical Reviews in Microbiology*, 26(4), 221–264. <https://doi.org/10.1080/10408410091154237>
- Socolofsky, S. A., & Jirka, G. H. (2001). *Environmental Fluid Mechanics Part I: Mass Transfer and Diffusion* (2nd ed.). Universitat Karlsruhe. <https://publikationen.bibliothek.kit.edu/1542004/1362>
- Song, J., Huang, G., Han, D., Hou, Q., Gan, L., & Zhang, M. (2021, October). A review of reactive media within permeable reactive barriers for the removal of heavy metal(loid)s in groundwater: Current status and future prospects. *Journal of Cleaner Production*, 319, 128644. <https://doi.org/10.1016/j.jclepro.2021.128644>
- Sorwat, J., Mellage, A., Maisch, M., Kappler, A., Cirpka, O. A., & Byrne, J. M. (2021b). Chromium (VI) removal kinetics by magnetite-coated sand: Small-scale flow-through column experiments. *Journal of Hazardous Materials*, 415, 125648. <https://doi.org/10.1016/j.jhazmat.2021.125648>
- Steeffel, C. I., Appelo, C. a. J., Arora, B., Jacques, D., Kalbacher, T., Kolditz, O., Lagneau, V., Lichtner, P. C., Mayer, K. U., Meeussen, J. C. L., Molins, S., Moulton, D., Shao, H., Šimůnek, J., Spycher, N., Yabusaki, S. B., & Yeh, G. T. (2014). Reactive transport codes for subsurface environmental simulation. *Computational Geosciences*, 19(3), 445–478. <https://doi.org/10.1007/s10596-014-9443-x>
- T.C. Resmi Gazete. *İçme Suyu Temin Edilen Suların Kalitesi Ve Arıtılması Hakkında Yönetmelik*. 06.07.2019. Sayı: 30823. Tarım ve Orman Bakanlığı
- Tarr, M. A. (2003, August 8). *Chemical Degradation Methods for Wastes and Pollutants*. CRC Press. [http://books.google.ie/books?id=mNHWiYTXmxEC&printsec=frontcover&dq=Chemical+Degradation+Methods+for+Wastes+and+Pollutants&hl=&cd=1&source=gbs\\_api](http://books.google.ie/books?id=mNHWiYTXmxEC&printsec=frontcover&dq=Chemical+Degradation+Methods+for+Wastes+and+Pollutants&hl=&cd=1&source=gbs_api)

- Thacher, R., Ravindran, V., & Pirbazari, M. (2016, May 5). Modeling and performance prediction of chromate reduction by iron oxide coated sand in adsorber reactors. *AIChE Journal*, *62*(10), 3717–3729. <https://doi.org/10.1002/aic.15257>
- Tumolo, M., Ancona, V., De Paola, D., Losacco, D., Campanale, C., Massarelli, C., & Uricchio, V. F. (2020, July 28). Chromium Pollution in European Water, Sources, Health Risk, and Remediation Strategies: An Overview. *International Journal of Environmental Research and Public Health*, *17*(15), 5438. <https://doi.org/10.3390/ijerph17155438>
- U.S. Environmental Protection Agency. (1998). MINTEQA2/PRODEFA2, A Geochemical Assessment Model for Environmental Systems: User Manual Supplement for Version 4.0. <https://www.epa.gov/sites/default/files/documents/SUPPLE1.PDF>
- U.S. Environmental Protection Agency. (2000, October). *In Situ Treatment of Soil Groundwater Contaminated with Chromium*.
- U.S. Environmental Protection Agency. (2009, May). *National Primary Drinking Water Regulations*. <https://www.epa.gov/ground-water-and-drinking-water/national-primary-drinking-water-regulations>
- USGS. (2022). *Mineral Commodity Summaries*. <https://pubs.usgs.gov/periodicals/mcs2022/mcs2022-chromium.pdf>
- Uyuşur, B. (2006). *Laboratory Investigation of the Treatment of Chromium Contaminated Groundwater with Iron-Based Permeable Reactive Barriers* [MA Thesis]. Middle East Technical University.
- Uyuşur, B., & Ünlü, K. (2009). A Laboratory Column Investigation for the Treatment of Cr(VI) with Zero-Valent Iron. *Environmental Engineering Science*, *26*(2), 385–396. <https://doi.org/10.1089/ees.2007.0089>
- Vaux, H. (2010). Groundwater under stress: the importance of management. *Environmental Earth Sciences*, *62*(1), 19–23. <https://doi.org/10.1007/s12665-010-0490-x>
- Yalçın, S. (2003). *Modeling Chromium Leaching from Chromite Ore Processing Waste* [MA Thesis]. Middle East Technical University.
- Zazo, J. A., Paull, J. S., & Jaffe, P. R. (2008). Influence of plants on the reduction of hexavalent chromium in wetland sediments. *Environmental Pollution*, *156*(1), 29–35. <https://doi.org/10.1016/j.envpol.2008.01.006>

- Walpole, R. E., & Myers, R. H. (1989, January 1). *Probability and Statistics for Engineers and Scientists*. Macmillan College.  
[http://books.google.ie/books?id=5oqiM8L9yYoC&q=Probability+and+Statistics+for+Engineers+and+Scientists&dq=Probability+and+Statistics+for+Engineers+and+Scientists&hl=&cd=2&source=gbs\\_api](http://books.google.ie/books?id=5oqiM8L9yYoC&q=Probability+and+Statistics+for+Engineers+and+Scientists&dq=Probability+and+Statistics+for+Engineers+and+Scientists&hl=&cd=2&source=gbs_api)
- Wanner, C., Eggenberger, U., & Mäder, U. (2011, August). Reactive transport modelling of Cr(VI) treatment by cast iron under fast flow conditions. *Applied Geochemistry*, 26(8), 1513–1523.  
<https://doi.org/10.1016/j.apgeochem.2011.06.015>
- WHO Team. (2022, March 21). *Guidelines for drinking-water quality: fourth edition incorporating the first and second addenda*.  
<https://www.who.int/publications/i/item/9789240045064>
- Wilkin, R. T., Su, C., Ford, R. G., & Paul, C. J. (2005, April 30). Chromium-Removal Processes during Groundwater Remediation by a Zerovalent Iron Permeable Reactive Barrier. *Environmental Science & Technology*, 39(12), 4599–4605. <https://doi.org/10.1021/es050157x>
- Wu, Y., Guan, C. Y., Griswold, N., Hou, L. Y., Fang, X., Hu, A., Hu, Z. Q., & Yu, C. P. (2020, December). Zero-valent iron-based technologies for removal of heavy metal(loid)s and organic pollutants from the aquatic environment: Recent advances and perspectives. *Journal of Cleaner Production*, 277, 123478. <https://doi.org/10.1016/j.jclepro.2020.123478>